A study of copper infiltration for conventional ferrous powder metallurgy

by

Arno Paul Scholtz

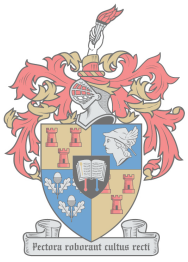

Thesis presented in partial fulfilment of the requirements for the degree of Master of Engineering (Mechanical) in the Faculty of Engineering at Stellenbosch University

Supervisor: Prof DC Blaine

December 2018

The financial assistance of the Department of Science and Technology (DST) towards this research is hereby acknowledged. Opinions expressed and conclusions arrived at, are those of the author and are not necessarily to be attributed to the DST.

Declaration

By submitting this thesis electronically, I declare that the entirety of the work contained therein is my own, original work, that I am the sole author thereof (save to the extent explicitly otherwise stated), that reproduction and publication thereof by Stellenbosch University will not infringe any third party rights and that I have not previously in its entirety or in part submitted it for obtaining any qualification.

Initials and surname: AP Scholtz
Date: December 2018

Plagiarism Declaration

1. Plagiarism is the use of ideas, material and other intellectual property of another's work and to present it as my own.
2. I agree that plagiarism is a punishable offence because it constitutes theft.
3. I also understand that direct translations are plagiarism.
4. Accordingly all quotations and contributions from any source whatsoever (including the internet) have been cited fully. I understand that the reproduction of text without quotation marks (even when the source is cited) is plagiarism.
5. I declare that the work contained in this assignment, except where otherwise stated, is my original work and that I have not previously (in its entirety or in part) submitted it for grading in this module/assignment or another module/assignment.

AP Scholtz Initials and surname	December, 2018 Date

Abstract

A study of copper infiltration for conventional ferrous powder metallurgy

AP Scholtz

Department of Mechanical and Mechatronic Engineering,
University of Stellenbosch,
Private Bag X1, Matieland 7602, South Africa.

Thesis: MEng (Mech)

2018

Powder metallurgy (PM) describes a group of manufacturing technologies whereby fine metallic powders are consolidated to create engineering components. The most widely used PM technology is the press-and-sinter process, used to manufacture ferrous alloys. Ferrous PM is frequently sinter-infiltrated with copper (Cu) in order to improve the materials machinability. During sinter-infiltration, molten copper infiltrates the inherently porous PM structure, filling the pores and creating a more dense, less porous material. Residual Cu, from incomplete infiltration, is a common defect in copper infiltrated PM parts. This project investigates the parameters of sinter-infiltration that are critical to successful infiltration and the production of high-quality Cu infiltrated ferrous PM alloys.

Common reasons for poor infiltration include incomplete delubrication prior to sintering, and inadequate furnace atmosphere and temperature control. Both of these aspects can introduce impurities into the material during the sintering process, which inhibits efficient infiltration and sintering. This study focuses specifically on the influence of delubrication and furnace control on the sinter-infiltrated material quality.

A proprietary copper-infiltrated ferrous PM alloy, with specified processing parameters, is used for this study. A systematic evaluation of both the

delubrication and copper-infiltration processes is presented. In order to perform this evaluation, it was necessary to implement control of the furnace temperature and atmosphere. As such, an extensive overhaul of the furnace at Stellenbosch University, with particular attention given to both the electrical and process gas flow systems, was performed and the details are presented in this study.

The results of the study indicate that in order to successfully perform good quality sinter-infiltration of the proprietary alloy with copper, different process gas atmospheres are required in the furnace for the delubrication and sintering steps, respectively. During delubrication, a reducing atmosphere of 80:20 vol% N2:H2 with a dewpoint of 8 °C must be maintained. During sintering an atmosphere composition of 80:20 vol% N2:H2 must be maintained with a low dewpoint of -35 °C. For the cooling of the samples an atmosphere composition of 95:5 vol% N2:H2 was used.

Furthermore, a detailed metallographic analysis of the consecutive stages of copper infiltration, over the temperature range of 1070 to 1130 °C was conducted. The results of which show how the interaction between Cu and Mn in the alloy significantly influences the melting and infiltration behaviour.

This research provides valuable insight into the high sensitivity of the copper infiltration process to furnace atmosphere control, as well as the advantage of understanding the detailed interaction between different alloying elements in the PM material during copper infiltration. Insight leads to the ability to control the process and to design for good quality copper infiltration during sintering.

Uittreksel

Studie van koper infiltrasie vir konvensionele ysterhoudende poeier metallurgie

("A study of copper infiltration for conventional ferrous powder metallurgy")

AP Scholtz

Departement Meganiese en Megatroniese Ingenieurswese,
Universiteit van Stellenbosch,
Privaatsak X1, Matieland 7602, Suid Afrika.

Tesis: MIng (Meg)

2018

Poeiermetallurgie (PM) beskryf 'n groep vervaardigingstegnieke waardeur fyn metaalpoeiers gekonsolideer word om ingenieurskomponente te skep. Die mees gebruikte PM tegnologie is die pers-en-sinter proses, wat gebruik word om ysterhoudende allooie te vervaardig. Ferro PM is dikwels sinter-geïnfiltreer met koper (Cu) om die materiaal se bewerkbaarheid te verbeter. Tydens sinter-infiltrasie infiltreer gesmelte koper die inherente poreuse PM struktuur, vul die porieë en skep 'n digter, minder poreuse materiaal. Residuele Cu, van onvolledige infiltrasie, is 'n algemene probleem in koper geïnfiltreerde PM dele. Hierdie projek ondersoek die parameters van sinter-infiltrasie wat krities is vir suksesvolle infiltrasie en die produksie van hoëgehalte Cu-geïnfiltreerde ferro-PM-legerings.

Gewone redes vir swak infiltrasie sluit onvolledige delubrikasie voor sintering, en onvoldoende oond atmosfeer en temperatuur beheer. Albei hierdie aspekte kan onreinhede in die materiaal tydens die sinterproses skep, wat effektiewe infiltrasie en sintering inhibeer. Hierdie studie fokus spesifiek op die invloed van delubrikasie en oond beheer op die sinter-geïnfiltreerde materiaal kwaliteit.

'n Besitlike koper-geïnfiltreerde Ferro PM-legering, met gespesifiseerde verwerkingsparameters, word vir hierdie studie gebruik. 'n Sistematiese

evaluering van beide die delubrikasie- en koperinfiltrasieprosesse word aangebied. Ten einde hierdie evaluering te kan uitvoer, was dit nodig om beheer oor die oondtemperatuur en atmosfeer te implementeer. 'n Omvattende opknapping van die oond aan die Universiteit Stellenbosch, met besondere aandag aan beide die elektriese en prosesgasvloeistelsels, was uitgevoer en die besonderhede word in hierdie studie aangebied.

Die resultate van die studie dui daarop dat ten einde suksesvolle sintere-infiltrasie van die besitlike allooi met koper te kan uitvoer, word verskillende prosesgas-atmosfere in die oond vir die delubrikasie en sinteringstappe onderskeidelik benodig. Tydens delubrikasie moet 'n reduserende atmosfeer van 80:20 vol % N_2:H_2 met 'n doupunt van 8 °C behoue bly. Tydens sintering moet 'n atmosfeer samestelling van 80:20 vol% N2:H2 behou word met 'n lae doupunt van minstens -35 °C. Vir die afkoeling van die monsters is 'n atmosfeer samestelling van 95:5 vol% N2:H2 gebruik.

Verder is 'n gedetailleerde metallografiese analise van die opeenvolgende stadiums van koperinfiltrasie, oor die temperatuurreeks van 1070 tot 1130 (°)C uitgevoer. Die resultate toon hoe die interaksie tussen Cu en Mn in die allooi die smelt- en infiltrasiegedrag aansienlik beïnvloed.

Hierdie navorsing bied waardevolle insig in die hoë sensitiwiteit van die koperinfiltreringsproses om oond-atmosfeerbeheer te gebruik, sowel as die voordeel om die gedetailleerde interaksie tussen verskillende legeringselemente in die PM-materiaal tydens koperinfiltrering te verstaan. Insig lei tot die vermoë om die proses te beheer en te ontwerp vir goeie gehalte koperinfiltrasie tydens sintering.

Acknowledgements

I would like to express my sincere gratitude to the following people and organisations;

Dr DC Blaine for her role as study supervisor throughout the course of this project.

Mr P Pieterse and Mr A van den Berg for their assistance with the repair of the pusher furnace.

Mr K Neaves for his assistance with electrical components.

Dr E Harmzen-Pretorius for her assistance with scanning electron microscopy.

Contents

List of Figures

List of Tables

List of Equations

List of Reactions

Chapter 1

Introduction

Powder metallurgy (PM) describes a group of manufacturing technologies whereby fine metallic powders are consolidated to create engineering components. The most widely used PM process is the press–and–sinter process, where the metal powders are compacted together in a die. The compacted shape is subsequently sintered in order to bond the powder particles together; this results in a coherent and reasonably strong part. Unique parts, in terms of part design or alloy and material formulation, can be produced through PM techniques, resulting in tailored material properties and components. The press–and–sinter PM technique, hereafter referred to as conventional PM, is well suited for high volume manufacturing, making it an attractive manufacturing process for mass-producers such as the automotive industry [1:2, 2:135, 3:375, 4:28, 5].

The most widely used PM alloys are the ferrous or carbon steel alloys, that are mainly used due to their relatively high tensile strength and low cost. The press–and–sinter process results in a material with around 10 – 15 vol% residual porosity. This influences the machinability of the press–and–sinter part. In order to mitigate machinability concerns, the green powder compacts are sinter-infiltrated with copper (Cu) in order to improve the material's machinability. Additionally, infiltration improves material properties: strength, corrosion resistance and thermal conductivity [1, 6, 7].

In sinter-infiltration, the porous compact and the infiltrant material, whilst in direct contact, are heated to a temperature above the melting point of the infiltrant but below the melting point of the compact. The infiltration and sintering of the part occur simultaneously. The molten infiltrant material fills the open porosity of the press–and–sinter part resulting in an increased density. This increase in density is the primary driver behind the improved material properties. Infiltration is capable of producing fully dense parts [1:255,3:389, 8].

Currently, in the general manufacturing industry, of which PM is a subset, there is a need to optimise production processes in terms of material and

energy usage. PM, including sinter-infiltration, is one means of achieving such improvements [9]. The infiltration process must be carefully controlled in order to avoid defects in parts. Due to the high production rates of sinter-infiltrated PM used in the industry, there is the potential to incur large losses (in time and monetary value) if product quality is not maintained.

Bleistahl–Produktions GmbH & Co. KG, a German company with a global presence, is a leading manufacturer of valve seat inserts and valve guides for the automotive industry. They wish to further develop of their sinter-infiltration process in terms of the infiltration defects that they experience during series production of parts. It is therefore evident that there is also the need in the industry to reduce or prevent the occurrence of defects resulting from the sinter-infiltration process. Accordingly, a partnership has been established between Stellenbosch University (SU) and Bleistahl–Produktions GmbH & Co. KG, from which a collaborative research project was conceived.

This project investigates parameters of sinter-infiltration that are critical to the production of high-quality ferrous PM alloys. This thesis document will present the theory of sinter-infiltration, and thereafter specific studies of the influence of delubrication and furnace parameter control on the sinter-infiltrated material quality. The results of these studies are evaluated and discussed, leading to the identification of cause and effect scenarios for process-specific defects. Finally, good practice guidelines for sinter-infiltration processes are compiled.

1.1 Research Question and Objectives

Research question:

What are the critical sintering process parameters for high-quality Cu sinter-infiltration of conventional ferrous PM alloys?

Research objectives:

1. Commission a functional set of equipment, required for the study of conventional ferrous PM sinter-infiltration, at SU.
2. Establish good sinter-infiltration practice with regards to delubrication of ethylene bisstearamide[1] (EBS).
3. Perform successful sinter-infiltration at SU.
4. Establish possible cause-effect scenarios regarding the formation of black residue on the proprietary Cu infiltrated alloy of Bleistahl–Produktions GmbH & Co. KG.

[1]EBS, also known by the trade names of Acrawax® and Licowax®)

1.2 Background

A commitment to long-term sustainable development was made by the Cabinet of South African with the approval of the South African Nation Framework for Sustainable Development (NFSD) [10] in 2008 and the National Strategy for Sustainable Development and Action Plan (NSSD) [11] in 2011. Since then South Africa has been working towards achieving sustainable development.

South Africa is a member of the United Nations (UN). In 2012, the United Nations Conference on Sustainable Development, Rio+20 identified two important themes that will support the move towards sustainable development of all its members not only for South Africa: "the green economy (sustainable development and poverty eradication) and an institutional framework for sustainable development" [12].

In 2011 the European Commission (EC), an institution of the European Union (EU), said in their Europe 2020 Strategy that "sustainable growth, which promotes a more resource efficient, greener and more competitive economy" is a priority for them [13]. It is therefore clear that sustainable development is a global concern, not only for developing countries but also for developed countries.

As part of the DST AMTS program[2] active research is being conducted at the SU on the project Resource Efficient Process Chains. The Resource Efficient Process Chains project investigates hybrid manufacturing processes in order to find the most resource efficient production methods according to variables such as material usage and energy consumption. This investigation, concerned with the green technology of PM [14], forms part of the overall programme.

1.3 Motivation

PM allows for the fabrication of near net shaped components, therefore the process incurs very little material wastage. Additionally, the process of infiltration provides energy efficiency gains by improving the machinability of the press–and–sinter PM parts [1:339, 5, 7]. Furthermore, infiltration results in improved material properties. As a result of these improvements resulting from the infiltration process, the Fe-Cu infiltration system is commonly used in industry and therefore well documented [8, 15, 16, 17, 18]. The aim of this study was to better understand the Cu infiltration process whilst attempting

[2]South African Department of Science and Technology (DST), Advanced Manufacturing Technologies Strategy (AMTS), , Stellenbosch University is currently collaborating in a consortium-based project "Resource Efficient Process Chains", managed through the Titanium Centre of Competence (TiCoC) and the Council for Scientific and Industrial Research (CSIR).

to improve the infiltration process used in industry, by Bleistahl–Produktions GmbH & Co. KG.

1.4 Scope and Limitations

This project was limited to:

- A literature review of conventional ferrous PM and copper infiltration.
- Investigation of Cu infiltration of the proprietary Fe-alloy of Bleistahl–Produktions GmbH & Co. KG.
- Infiltration, and related, studies were conducted using the existing laboratory facilities at SU.
- Green compacted materials are limited to those supplied by Bleistahl–Produktions GmbH & Co. KG.
- Sample shape and size are limited to typical dimensions for process development studies.

Chapter 2

Literature Review

This chapter provides a basis for the understanding of the theory and processes involved with sinter-infiltration of ferrous press–and–sinter PM alloys. Firstly, the conventional press–and–sinter PM manufacturing process is outlined, thereafter the importance of correct delubrication is highlighted and finally the infiltration process employed for Cu infiltration of ferrous press–and–sinter PM parts is explained.

2.1 Overview of Conventional Ferrous Powder Metallurgy

PM describes a group of manufacturing processes whereby metallic parts are produced from metal powders. Conventional press–and–sinter PM, hereafter referred to as conventional PM, involves a sequence of three basic operations, 1) powder blending and mixing, 2) compaction of powders into a green compact of the desired shape, and 3) subsequent sintering of the green compact [2:135, 3:375, 5:759, 6].

Conventional PM holds several advantages, 1) the production of near net shaped parts (with tolerances of $\pm 0.13\,\text{mm}$) thus eliminating extensive machining actions and reducing material waste, 2) flexibility in design and product shape complexity, 3) uniform microstructure and alloying element distribution, 4) the possibility of producing parts with a specific level of porosity, 5) fabrication of materials that are otherwise challenging or impossible to produce, 6) process automation and efficient high volume production of parts [2, 3:376, 5:24]. Nevertheless there are some challenges to overcome, 1) the high cost of tooling, equipment and powders, 2) powder storage considerations (e.g. flammability, oxidation), 3) part shape is limited to shapes that can be uniaxially compacted, 4) density variations, 5) limited size of parts, 6) poor machinability due to inherent porosity of PM materials [3:376, 5:24, 19].

The capital, running, and maintenance costs for compaction and sintering

of PM parts are expensive, therefore PM is mostly used for medium (100 – 10 000 units) to high (>10 000 units) production rates [3:6]. In order to facilitate a continuous production cycle, as is typically required for efficient PM manufacturing, continuous sintering furnaces are used. Green compacts are continuously fed into the one side of the continuous sintering furnace and sintered parts are removed from the other. Routine production rates of sintered components with continuous sintering furnaces are around 100 kg/hr [1:275].

2.1.1 Powder Production

The dominant powder production process for powders that are suitable for conventional PM, is water atomization. This process is flexible and easily scalable [5]. A substantial portion (~30 %) of commercial iron powder is, however, produced by the sponge iron process [20].

Water atomization occurs by impengeing water jets onto a stream of molten metal, causing the molten steam to break up into countless small droplets (i.e. atomize). These droplets solidify into individual powder particles [3:382, 6]. This process allows large quantities of powder to be produced with relative ease. A wide range of particle sizes can be produced, depending on the adjustment of several parameters, such as nozzle size and atomization fluid velocity. The particle shape is influenced by the atomizing fluid, with higher heat capacity fluids, such as water, producing more irregularly shaped particles [6].

Sponge iron powder is produced by the reduction of iron ore into sponge iron and subsequent crushing. This produces iron powder with highly irregular particle shapes [20]. The process gets its name from the soft and easily compressed sponge-like particles, which give rise to compacts with high green strength [6]. Water atomized powders are typically used where a part density of $< 6.4\,\mathrm{g/cm^3}$ is desired [5:1870]. Sponge iron powder is typically used where a part density of $> 6.7\,\mathrm{g/cm^3}$ is desired [5:1870].

Electrolytic copper powder is typically used to compact discs for infiltration during sintering [6]. Here a dilute aqueous solution of copper sulphate and sulphuric acid is used to deposit copper particles at a copper electrode in an electrolytic cell [3, 21]. The particles are cleaned, annealed and crushed to form copper powder.

2.1.2 Powder Characteristics

There are several attributes of powders that aid in understanding the performance of powders. These attributes are listed in Table 2.1 [1], along with their standard test methods, and subsequently discussed in this section:

Table 2.1: Powder characteristics and corresponding test methods [1]

Powder Characteristic	**Test Method**
Particle size	Microscopy with image analysis software and statistical techniques. An older method still in use is sieve analysis (ASTM B214).
Particle shape	Aspect ratio measurements using microscope image analysis.
Surface area	Gas absorption (ASTM B922) and gas permeability (ASTM E2980) tests. Estimates are possible with microscopy.
Packing Density and interparticle friction	Apparent density measurements with Hall (ASTM B212), Scott (ASTM B329) and Arnold (ASTM B703) meters. And packing density measurements through the gas pressure-volume technique. Powder flow rate can be measured using a Hall Flowmeter
Compressibility	Measurement of the pressure required to attain a target green density or vice versa (ASTM B331), where the density is measured using the Archimedes principle (ASTM B962).
Particle Internal Structure	The powder is mounted in resin, subsequently polished and etched to reveal the internal structure of particles.
Chemical characterization	Overall composition and impurity tests use emission or fluorescence spectroscopy. Combustion tests for impurity (oxygen, nitrogen, carbon) concentrations. Other tests include: loss on reduction, ceramic inclusion, X-ray techniques, and electron or ion beam measurements.

Powder particles can be produced in a wide range of sizes, 10 – 1000 μm, however for conventional press–and–sinter PM, particle sizes of 25 – 200 μm are typically used [2:112, 3:379, 5:83]. The desired particle size distribution is often obtained through sieving the powder through a series of sieves. These sieves are rated with a certain mesh count, the number of openings found in a linear inch of a sieve, thus higher number rated sieves will produce smaller particle sizes [3:378]. Particle sizes are typically characterised by a single dimension. Analysis of powder particle size distribution is conducted according to ASTM E2651 standard.

Powder particle shape is conveniently expressed as an aspect ratio, of the maximum to the minimum dimension of the particle [3:379]. For spherical powder particles, this value is 1 and tends towards zero for increasingly

irregularly shaped powder particles. Irregularly shaped particles result in mechanical interlocking which leads to high green strength compacts, suitable for press–and–sinter applications [22:84]. Higher green strengths prevent cracking during compact ejection and damage during handling or transportation [22:98]. Conversely, powders with irregular particle shapes do not flow as well as spherically shaped powders and are therefore not suitable for other PM technologies, such as additive manufacturing or powder injection moulding [22:96].

Powder particle shape influences the specific surface area[1] of a powder, which in turn affects the sintering process. To a great extent powder particle size also influences the specific surface area [22:97]. The specific surface area, 'S' [m^2/kg] is inversely related to the particle diameter, 'D', and powder particle density, 'ρ', as follows in Equation 2.1.

$$S = \frac{6}{D \cdot \rho} \tag{2.1}$$

Increasing surface area increases the amount of friction in a powder which results in less efficient flow and powder packing. The Hall flow rate test is the ASTM B213 standard test method for the flow rate of metallic powders. The apparent density can be measured with a Hall flow meter, according to ASTM B212 standard. The apparent density is the mass per unit volume of loose powder. Apparent density gives an indication of how well the powder particles pack into a given volume [1:45].

Compressibility is a measure of the densification of a powder subjected to an applied load. Compressibility is determined through measurement of the pressure required to achieve a target green density or vice versa. The density of a compacted specimen is determined through the ASTM B962 standard using the Archimedes principle. Typical PM ferroalloys start with an apparent density around 2.4 – 2.7 g/cc (~78 % porosity) and compact to around 6.6 – 6.9 g/cc (~14 % porosity).

[1]Specific surface area is defined as the total surface area of a material per unit mass [1:41].

2.1.3 Alloying Elements

Four different approaches are used in PM to create alloy materials: (1) admixed alloys, (2) partial alloys (diffusion alloys), (3) pre-alloys and (4) hybrid alloys [5:1870]. Admixing is generally the least expensive and most widely used alloying method. Admixed powders are created by mixing alloying elements in the elemental or ferroalloy[2] powder form to the base iron powder. This allows the powder mixture's compressibility to be, in most cases, similar to that of the base iron powder [5:1870]. Alloying of the admixed powder occurs through diffusion during sintering and is dependant on the diffusivity of the alloying elements in iron at the sintering temperature. Alloying occurs by the formation of solid solutions and/or intermediate solutions. Typical alloy additions include carbon, added in the form of graphite powder, copper, manganese, sulphide, and alloy steel powders [3].

2.1.4 Lubricants

Several types of waxes, listed in Table 2.2 are typically added, in powder form, to PM mixtures as lubricants [1:134, 5:755, 6, 23–27]. These lubricants reduce inter-particle and die-wall friction during compaction, reducing friction between the powder and tooling surfaces, and aid in the ejection of the compact from the tooling [1:134, 3, 5, 22:77,]. The reduction in friction allows for the use of smaller compacting forces to achieve larger green densities and strength, with reduced density gradients [1:134, 5, 22:98]. Additionally, the die tooling is protected from excessive wear [28:8].

Table 2.2: Common Lubricants [1:134, 5:755, 6, 23–27]

Lubricant	**Chemical formula**	**Melting point**	**Density**
Zinc Stearate	$Zn(C_{18}H_{35}O_2)_2$	130 °C	1.1 g/cc
Lithium Stearate	$LiC_{18}H_{35}O_2$	221 °C	1.025 g/cc
Paraffin	$C_{22}H_{46}$ to $C_{27}H_{56}$	40 – 60 °C	0.812 g/cc
Acrawax®*	$C_{38}H_{76}N_2O_2$	140 – 145 °C	0.97 g/cc

*Acrawax® is the trade name of a compound with the generic name of ethylene bisstearamide (EBS).

Generally 0.5 – 1.5 wt% of lubricant is added to the bulk metal powder [1:134, 5:571, 29]. Table 2.2 [1:134, 6, 5:755, 23–27] presents the density of common lubricants as ~1 g/cc, much lower than the density of iron at 7.9 g/cc given in Table C.1 [30–34]. Therefore the mass of lubricant results in a substantial amount of lubricant volume that is added to the metallic powder,

[2]The term ferroalloy refers to various iron alloys with a high alloy proportion.

thus adversely affecting the maximum attainable green density [1:197, 5:571]. For these quantities, it can be assumed that the higher the lubricant content, the lower the powder flow rate [1:134, 5:692]. A low flow rate negatively affects the compaction process production rate [22:98].

Lubricants are typically hydrocarbon polymers. In order to facilitate successful sintering, these hydrocarbons must be decomposed and burnt off before the compact enters the high heat zone [35:179]. This process is called delubrication and is further explained in Section 2.3. Failure to fully burn off the polymers results in carbon contamination of the final sintered material. This affects the mechanical properties as well as the ability to form strong sintered bonds between particles.

2.1.5 Mixing and Blending

The first step of the PM process is powder blending and mixing; powders can be blended or mixed with alloy powders or constituents in order to control properties of the final product or facilitate the subsequent PM processes: compaction and sintering. The final product's material properties are controlled through the density, powder and processing parameters of the PM process. To a large degree, mixing and blending of powders allow for control over density and the production of custom alloys [1:140, 5:24)].

In order to tailor the PM process and product, powder mixtures contain various powders to produce the desired alloy material, waxes that serve as lubricants, and sometimes binders that impart green strength to the compact and deflocculants that improve the loose powder's flow rate [3:304, 22:85].

2.1.6 Powder Compaction

The next step in conventional PM is die compaction, where the powder mixture or blend is compacted in order to form the desired part shape. Compaction (or compression) involves the application of uni-axial loads to the loose powder, in a die, ranging from 650 MPa – 1000 MPa resulting in a green compact [1:184, 4:109, 3:306, 2:135]. Green compacts are held together by interlocking particles and particle-to-particle cold-welds [1:193, 2:135, 28:8]. It is for this reason that irregularly shaped powders, such as water atomized or sponge iron powders, are preferred for die compaction [22]. The compaction process provides adequate green strength and the desired green density for handling and sintering of the compact [1:197]. As a result, the degree of densification that occurs during sintering is minimal in order to control dimensional accuracies.

Sufficient green strength allows the compact to be handled after the compaction process [28:8, 36].

Figure 2.1 is a cross-sectional view of a uni-axial die set. The numbering balloons indicate the following components: (1) punch base plates, (2) upper punch, (3) inner die, (4) outer die[3] and (5) the lower punch. The arrows indicate the uni-axial force (F) applied to the punches.

The die set is orientated such that compression occurs in the vertical direction. The loose powder is poured into the die cavity with a certain fill height in order to produce a compact with desired dimensions and density. The full compaction force is now applied to by moving both the upper and lower punches towards each other. The die is free to move during compaction, creating a floating die setup. This results in dual-action compaction which ensures a more uniform density gradient in the compact [5:732]. Compacting without a floating die setup, the load is applied by the actuating punch and is called single action compaction.

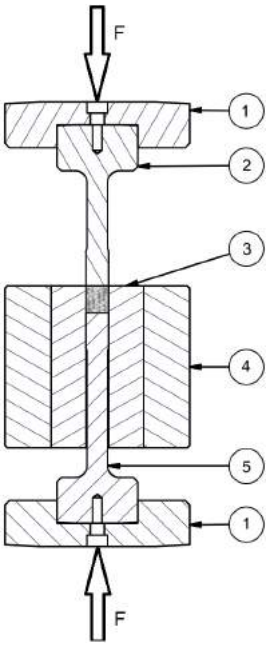

Figure 2.1: Die tooling cross-section

2.1.7 Sintering

Following compaction, the green compacts are sintered. Sintering is a process whereby solid bonds form due to solid state diffusion between powder particles at elevated temperatures [1:219, 5:1095]. Normally a sintering temperature of 0.6 – 0.9 of the powder's principal constituent's melting point is chosen [2:135, 3:387, 4:47]. Ferrous PM components are typically sintering in the range of 1120 – 1150 °C [4:47]. This temperature range is used due to the phase transformation temperatures of the Fe-C system, further detailed in Section 2.5. Additionally, the heating rate used to reach the sintering temperature is important for the prevention of defects. [1:277] reports that a typical heating rate of 10 °C/min is used for a Fe-2Cu-0.8C system.

During sintering compacts are consolidated, resulting in a number of benefits, through particle bonding; 1) increased density, 2) the ability to sinter active elements in alloy steels, 3) improved mechanical properties (hardness, toughness, strength, etc.), 4) improved physical properties (ductility, thermal conductivity, etc.) [1:219, 3:306]. In PM a strong emphasis is placed on the density of PM parts because an approximate linearly increasing relationship is seen between sintered density and the tensile and fatigue strength. While

[3]The outer die is added for increased safety. Stresses induced in the die set components during compression (such as axial loading and radial expansion) can result in the failure of the punches and/or die. The outer die provides the required radial strength, additionally providing a barrier to crack propagation.

an exponential increase is found for elongation and impact strength with sintered density [4:46].

Sintering is divided into three stages: 1) the initial stage where neck formation occurs, but there is no change in density, 2) the intermediate stage where neck growth, pore rounding and densification occurs, 3) the final stage where pores become isolated as grain growth occurs with limited densification [6].

There are two types of mass transport mechanisms active during sintering [1:221, 37:657, 38]: (1) surface transport, which results in the bonding of particles and (2) bulk diffusion, which results in densification [38]. The driving force for sintering is the reduction of surface energy by reducing the surface area of the powder compact. Elevated temperatures promote increased diffusion rates thus increasing the sintering densification rate of the compact [1:221, 5:1130]. Densification of the compact is required in order to increase the part strength. Densification results in increased load bearing structure, within a cross sectional area, thereby increasing part strength.

Sintering starts at the contact interface between two particles, as seen in Figure 2.2. Particle bonding occurs between the particles, creating a neck [1:221, 37:656]. The formation of a neck is accompanied by the formation of a grain boundary, indicated by the dotted line in Figure 2.2. As the necking region grows, due to surface transport, the potential for bulk diffusion increases [38]. Necking will progress while sintering until the two particles are indistinguishable from one another.

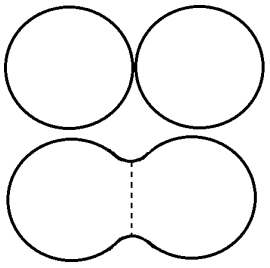

Figure 2.2: Necking formation between two powder particles

Figure 2.3, adapted from [5:1033], is a magnified cross-sectional view of a necking region between two powder particles. The figure presents the different material transport modes found during sintering, with arrows indicating the direction of transport of atoms from one location to another. The arrows are labelled with letters [1:221, 5:1033, 37:657, 38]:

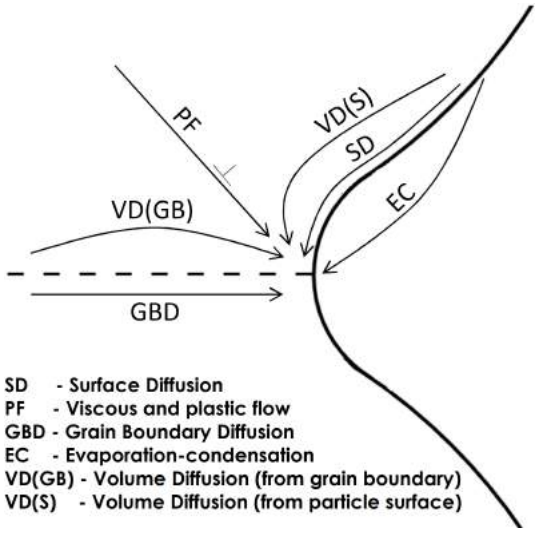

Figure 2.3: A magnified cross-sectional schematic of the mass transport mechanisms active during conventional PM sintering [5:1033]

Although most of the powder's surface energy can be eliminated during sintering, a portion of the surface energy is also transformed into grain boundary energy [1:221, 37:657]. Grain boundaries are dissimilar materials and/or misaligned crystal structures sharing a border. Nearly all previous particle contact surfaces are transformed into grain boundaries due to the misalignment of their crystal lattices [1:221, 37:657].

Grain boundary diffusion is generally considered the dominant mechanism for sintertering densification [1:230]. Defects in the grain boundary allow for mass flow to occur between grains [39:92]. Vacancies are annihilated at the grain boundary through slip and rotation. Mass flows along the grain boundary and is deposited at the particle bond, resulting in grain growth. During the later stages of sintering, grain boundary diffusion is less effective as a vacancy sink and densification has progressed such that the solid structure resists further densification. These conditions result in pore coarsening, due to transport along the grain boundaries [39:92].

Pore rounding promotes the formation of interconnected pores at the expense of smaller voids. These interconnected pores allow fluids, such as molten metal (as in sinter-infiltration) or process gases, to move through the compact. As sintering continues, pores decrease in size as the surface energy is further reduced. As the pore size is reduced, densification takes place, and shrinkage of the compact occurs [3:307]. Furthermore, porosity is reduced through bulk diffusion to the grain boundaries, which result in the increase in density [5:2071]. With the continued reduction in surface energy, the sintered part approaches full-density, but is limited by the entrapment of gases inside pores [1:229]. However, interconnected pores are essential for infiltration to

occur. Pores are interconnected up to ~92 % of full density, after this point the interconnected pores close off and tend to become more spherical [39].

Under closely controlled process parameters, shrinkage due to densification is predictable. An important parameter in this regard is the green density of the compact, which in turn depends on the compaction pressure used. In order to account for shrinkage, the compaction tooling is oversized [37]. The largest dimensional change occurs in the radial direction, perpendicular to the direction of compaction [5:1021]. Iron-based compacts with conventional commercial particle size distribution, a green density of 6.6 – 7.1 g/cc, sintered at 1100 – 1200 °C, for 0.5 – 1 hr, typically present minimal shrinkage of <1 %.

2.2 Role of Sintering Furnace

The sintering furnace is integral to the PM production line. After the metal powder has been compacted into the green shape, the compact is sintered in order to bond the metal particles together, as explained in Section 2.1.7. It is important to ensure that impurities are not present in the final sintered microstructure in order to produce high quality sintered materials.

The literature presented in this section has been limited to the use of a N_2:H_2 mixed atmosphere, as this is the most common sintering atmosphere used for ferrous PM. The interested reader is referred to [35] for information on alternative atmospheres. All of these atmospheres prevent oxidation and promote the reduction of oxides at elevated temperatures. Further than these two main objectives of the sintering atmosphere the choice of atmosphere also serves the purpose of; 1) protecting the furnace and sintered parts from oxidation, 2) removing surface oxides through reduction, 3) recarburizing (material composition), 4) lubricant and binder removal (delubrication), 5) control over the heat transfer rate [3:308, 35, 40].

The sintering atmosphere is particularly important when sintering PM parts. PM compacts are porous which exposes a large surface area of material to the sintering atmosphere. This allows for large areas where reactions can take place between the compact and the atmosphere – the effects of which are aggravated by the high temperatures employed [5:1057].

Continuous sintering furnaces are most frequently used for conventional PM. They have multiple, sequential, chambers or zones which each serve a specific function. (1) The preheat zone is where lubricants and binders are burnt off. (2) The hot zone is where sintering takes place; and (3) the cooling zone is where the sintered parts are cooled for handling and removal from the protective atmosphere [3:308, 5:1058]. These zones can be seen in Figure 2.4, adapted from [3:308], where a schematic of a continuous sintering furnace is presented.

Green compacts are placed on a conveyor belt which moves the parts into the furnace at the preheat zone through baffles. A baffle is a partition between two areas used to restrain the flow of gases between them. Baffles are typically made of fibrous material, such as fibreglass, which create curtains that sweep over the PM parts [41]. The baffles, located before the preheat zone and after the cooling zone (and sometimes between furnace zones), impede the loss of heat and process gas from the furnace (or between furnace zones). Additionally, impeding also the movement of atmospheric air into the furnace. The PM compacts move, sequentially, through the three furnace zones at a constant velocity (belt speed). The belt speed is set so that the compacts experience the required heating rate and the required amount of time at temperatures within the different zones. Prior to exiting the furnace, in the cooling zone, samples are cooled under a protective atmosphere in order to prevent oxidation.

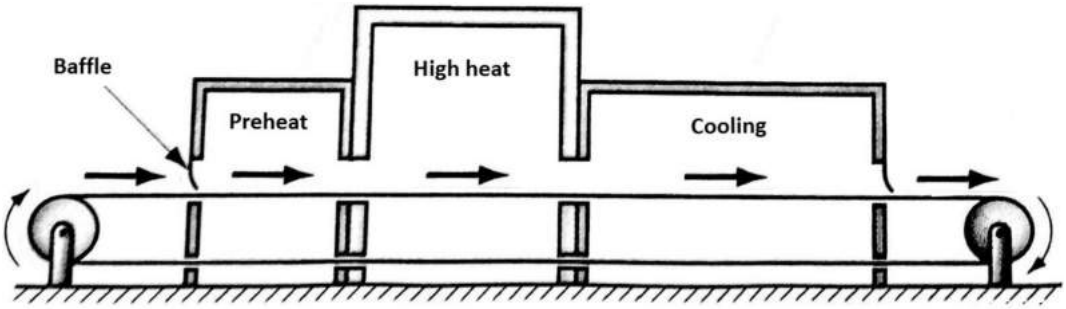

Figure 2.4: Pusher furnace schematic adapted from [3:308]

Each furnace zone (the preheat, hot and cooling) has a specific requirement for the composition of the atmosphere, or process gas, in that region. In order to control the furnace atmosphere, adjustment of the H_2 gas flow rate and/or the oxidizing agent (H_2O) is employed [41]. Typical monitoring of the furnace atmosphere incorporates oxygen probe measurements and a PLC-based controller that regulates N_2, H_2, and oxidising agent (H_2O) flow rates into the different sections of the furnace. Alternatively, monitoring of the furnace atmosphere can be done using dewpoint measurement with a hydrogen analyser, or a hydrogen analyser and oxygen probe to determine the dewpoint [41].

For ferrous PM (carbon steels), the (typical) atmosphere throughout the furnace is plotted in Figure 2.5. The temperature curve depicted in this figure shows approximately isothermal conditions at the delubrication and high heat zones which are preceded by relatively constant heating rates (5 °C/min [1:277]). These isothermal temperature zones provide the constant hold temperatures, across a distance inside the furnace, such that conveyor is not required to stop in order to initiate an isothermal hold of the components it carries. The delubrication zone's isothermal temperature is typically 600 –

800 °C [1:268]), while the high heat zone's isothermal temperature is (~1120 °C [1:277]).

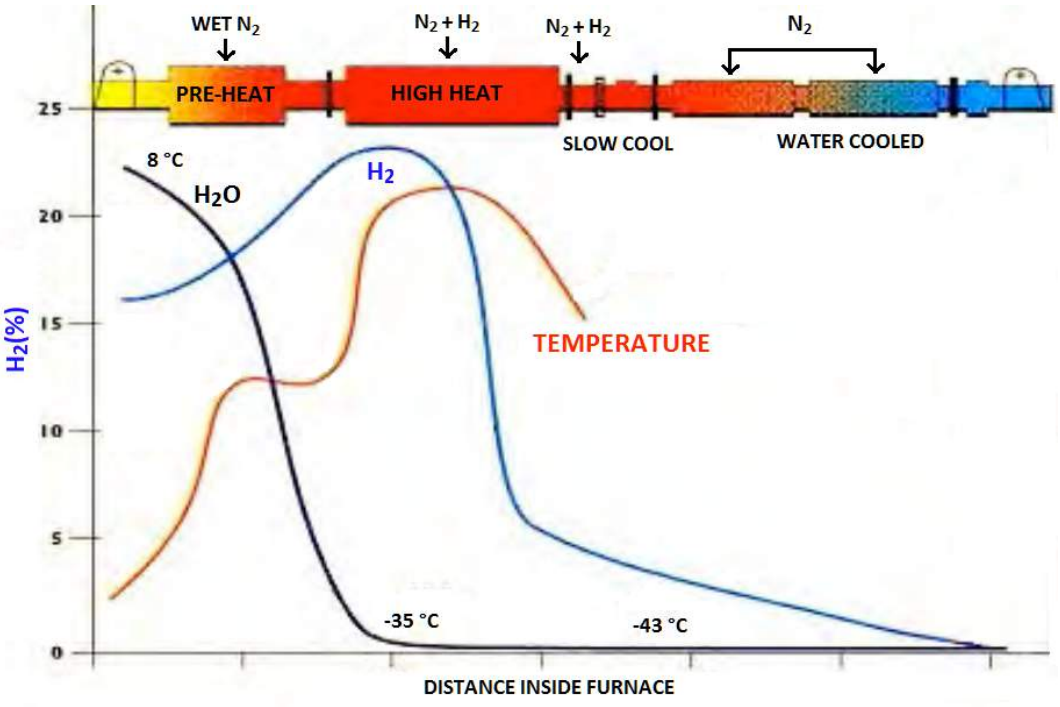

Figure 2.5: Typical continuous sintering furnace atmosphere for carbon steel, adapted from [40]

The goals of the preheat zone are to remove any residual lubricant from the compact by thermal decomposition (termed delubrication) and to control the heating rate while heating to the required sintering temperature. It is important that all hydrocarbons, such as lubricants, are removed in the preheat zone. If any hydrocarbons reach the high-heat zone soot formation occurs, manifesting as carbon (C) deposits, on the part surfaces. Soot formation is unwanted because it impedes sintering and infiltration [8], but also negatively affects the aesthetics of the sintered component.

Figure 2.5 shows that the preheat zone atmosphere must have a high dewpoint (~8 °C) which results in a slightly oxidising atmosphere [5, 40]. The high dewpoint provides the necessary oxygen, in the form of water vapour ($H_2O_{(v)}$), for the delubrication process [40]. During delubrication, the sintering atmosphere prevents carbon residue formation (or sooting) on sintered parts by chemically reacting with carbon, from the decomposing hydrocarbons. The products of lubricant decomposition and delubrication must be removed from the furnace through the flow of the furnace atmosphere. It is, therefore, also important that the process gas has a high enough flow rate, from the rear of the furnace to the front, in order to facilitate the removal of these products [40]. Typically, at least 80 % of the

furnace atmosphere should flow against the direction of travel of the PM parts, maximizing interaction between the atmosphere and the samples [41]. An atmosphere turnover rate of at least 10 times per hour is required to aid in the removal of the polymer burnout products [1:268]. Consequently, the preheat zone typically has a composition of 85:15 - 80:20 vol% (N_2:H_2) with a dewpoint of ~8 °C [5:1069, 40, 42:74]. The large vol% of nitrogen provides the required, protective, atmosphere turnover rate [1:268].

The purpose of the hot zone is to facilitate sintering. In the hot zone, the oxides on the surface of the powder particles must be reduced in order to promote sinter bonding. This is accomplished by enveloping the parts in an atmosphere that decomposes the oxides by a redox reaction. Consequently, a strongly reducing atmosphere with a low dewpoint is required for the removal of surface oxides and oxidation prevention. A sintering atmospheres' reducing capability is typically characterised by the dewpoint. The dewpoint of an atmosphere is the temperature, at a specific barometric pressure, below which condensation occurs. The closer the dewpoint is to the atmosphere's temperature, the closer the atmosphere is to saturation in terms of water vapour content. A relative humidity of 100 % indicates a saturated atmosphere, which occurs when the dewpoint equals the current atmosphere temperature [43]. It is therefore important to have a low moisture (water vapour) content or dewpoint (~-40 °C) [1:277] in this zone with a higher concentration of H_2 (~23 vol%) [40]. H_2 is a strong reducing gas at high temperatures and is therefore used for this purpose. The typical hot zone atmosphere composition is N_2:H_2, 80:20 - 75:25 vol% [40]. Hydrogen reduces iron oxides according to the following reactions [41, 44].

$$Fe_3O_4\ (s) + H_2\ (g) \longleftrightarrow H_2O\ (g) + 3\,FeO\ (s) \quad \{1\}$$

$$Fe_2O_3\ (s) + 3\,H_2\ (g) \longleftrightarrow 2\,Fe\ (s) + 3\,H_2O\ (g) \quad \{2\}$$

$$FeO\ (s) + H_2\ (g) \longleftrightarrow Fe\ (s) + H_2O\ (g) \quad \{3\}$$

As can be seen, these reactions are reversible, thus if there were to be a shortage of hydrogen available iron oxide would form in the presence of water vapour. The direction of these reactions is controlled by the ratio of the partial pressure of H_2 to H_2O (g) [41]. Additionally, H_2O and H_2 are in equilibrium as per Reaction 4.

$$2\,H_2O\ (g) \longleftrightarrow O_2 + 2\,H_2 \quad \{4\}$$

Once the parts have completed their sintering cycle, they enter the cooling zone. The goal of the cooling zone is to cool the sintered parts to below their oxidation temperature, in air, for removal from the protective furnace atmosphere. A slightly reducing atmosphere in the cooling zone is desirable

because the sintered components entering the cooling zone are still at a very high temperature and are susceptible to rapid oxidation [5:1062]. The cooling zone atmosphere consists primarily of N_2 (> 90 vol%) with decreasing amounts of H_2 (< 10 vol%) and a low dewpoint ($<$ -40 °C) [40].

Not included in Figure 2.4 are the flame curtains, typically produced through combustion of natural gas, that are located at the furnace entrance and exit. Additionally, most sintering furnaces are equipped with an exhaust hood and vent piping system. The function of this exhaust system is to safely vent the escaping furnace atmosphere [41]. Flame curtains are used to limit the ingress of air into the furnace [41]. Furthermore, the flame curtain burns-off lubricant vapours as they exit the furnace and preheat samples aiding in the delubrication process.

The flame front can also provide the furnace operator with information on the furnace atmosphere. A flame curtain receding into the furnace indicates an insufficient atmosphere flow rate, which can lead to PM part defects. A fluctuating flame curtain indicates an unstable furnace atmosphere which can lead to variable properties in the PM parts. The desired positive pressure inside the furnace is indicated by a flame curtain that is slightly blown out by the flow of the furnace atmosphere exiting the furnace [41]. The heat generated from the burn off of delubrication products and H_2 at the flame curtain results in a draft, or negative pressure inside the furnace, which tends to pull the furnace atmosphere upward and out of the furnace. This draft can result in a large ingress of air at the furnace exit, which in some cases are mitigated through adjustable nitrogen injection nozzles [41].

2.3 Polymer Burn-off and Delubrication

The most important and most frequent problems found during sintering result from incorrect or incomplete polymer delubrication [40]. Lubricants must be entirely removed before the compact reaches the sintering temperature in order to promote effective sintering [8, 35:179]. Delubrication (delubing) of PM parts is sensitive to temperature and atmosphere conditions. The delubing section of a continuous furnace heats PM compacts to above the melting temperature of the lubricant, where the hydrocarbon compounds are decomposed and burnt-off or vaporized. This section contains an overview of the chemistry involved with polymer burn-off and delubrication, whereafter good practice procedures for delubrication are given.

2.3.1 Delubrication Reactions

Delubrication is a thermally activated process, whereby the hydrocarbon lubricants melt, decompose/pyrolysis, and then eventually evaporate as

gases, leaving the compact clean of any lubricant decomposition products. The lubricants listed in Table 2.2 typically start to melt around 150 °C. At this point, the larger hydrocarbons in the lubricant start to decompose into smaller, more volatile, hydrocarbons [1:226]. This thermal decomposition process is known as pyrolysis or thermolysis. Evaporation of the pyrolysis products occur at 300 – 500 °C [1:226] or 425 – 650 °C [5]. The pyrolysis products are typically CH_4 (methane), C_2H_6 (ethane), C_4H_{10} (butane), C_3H_8 (propane), CO (carbon monoxide), CO_2 (carbon dioxide) and $H_2O_{(g)}$ (water vapour) [1, 5].

The gases interact with the each other principally through a few important reactions. Sooting occurs through the continued decomposition of the hydrocarbon products resulting from the decomposition of the lubricant as follows [5:1068].

$$CH_4(g) \longrightarrow 2H_2(g) + C(s) \quad \{5\}$$

Gas products from pyrolysis react with H_2 and H_2O as follows:

$$CO_2(g) + H_2(g) \longleftrightarrow CO(g) + H_2O(g) \quad \{6\}$$

$$C_xH_y(g) + H_2O(g) \longleftrightarrow CO(g) + CO_2(g) + H_2(g) \quad \{7\}$$

In Reactions 6 and 7; CO, CO_2 and H_2O are on opposite sides of the reactions, allowing for control of the atmosphere through control of the gas ratios. The reactions can be monitored using the dewpoint, which gives an indication of the H_2O content of the atmosphere [1:267]. Control of the ratios of CO_2:CO and H_2O:H_2 allows control of the atmosphere [1:267]. In addition to these reactions, there are numerous other possibilities (similar to the reactions presented here) however, analyses of these reactions sufficient in order to understand the fundamentals of furnace atmosphere control.

A study was conducted by [29] on Acrawax® (EBS) where the chemical mechanisms of its decomposition were described. The results indicated that EBS, with a chemical composition of $C_{38}H_{76}N_2O_2$, decomposes by a series of competing reactions, including EBS hydrolysis to stearic acid, followed by further pyrolysis and decarboxylation[4]. It was shown that EBS ultimately decomposes, in anhydrous conditions between 200 – 600 °C, into mainly CO_2, CH_3, and CH_2. Minor decomposition products, approximately an order of magnitude lower than the CO_2 concentrations, include CO, CH_4, CH, C_2H_4, and NH_3. The characteristic temperature, where the lubricant has lost half of its mass, was established as 450 °C [29].

[4]Decarboxylation is a chemical reaction wherein a carboxyl group (COOH) is removed from the hydrocarbon and carbon dioxide (CO_2) is released.

The carbon-containing decomposition product gases must be quickly removed from the delubrication section in order to prevent further breakdown, on or inside the sintered compacts, which will result in sooting. Some of the decomposition product gases, if not removed, are burnt off using oxygen, contained in the species; O_2, CO_2 and H_2O [1:268, 45:154]. The products resulting from the burn-off reactions (CO and CO_2) are then safely swept away by the flow of the furnace atmosphere process gas [45:154].

2.3.2 Temperature and Heating Rate

It can be seen that for the lubricants used in conventional PM given in Table 2.2, their melting points (and thus the onset of pyrolysis) are relatively low, $<$ ~220 °C [1:134, 5:755, 6, 23–27]. However, removal of the lubricants is influenced by the density and cross-sectional area of a PM part, therefore higher temperatures are often used for delubrication [5:1060]. The higher temperatures allow for chemical reactions to occur at an increased rate, the viscosity of lubricants to further decrease, and their product gases to become more volatile – promoting their removal from the compact. Additionally, carbon oxidation occurs at temperatures as low as 400 °C, but carbon deposits are usually removed at temperatures of 600 – 800 °C (up to ~1010 °C) due to the physical restrictions imposed by the porous metal matrix [1:268, 19].

Within a continuous furnace, there is limited time for complete and effective delubrication to occur. Delubrication, under the correct processing parameters, follows a sigmoidal function, where the lubricant starts at an initial mass which reduces as the temperature is increased, as shown in Figure 2.6. The maximum rate of lubricant mass loss occurs at the steepest gradient of the sigmoid. In order to prevent damaging the compact, a slow heating rate during periods of high mass loss must be used [1:226]. A typical heating rate of 20 °C/min for ferrous compacts, with a green density of 7.05 g/cc, containing Acrawax® [46]. This heating rate conflicts with the typical heating rate, of 10 °C/min given by [1:277]. The sintering process is often a trial and error process and when considering heating rates, the more conservative approach is to use a lower heating rate, rather than a higher heating rate with a larger probability of resulting in defects.

An empirical model for the delubrication of PM parts is given in Equation 2.2 [46]. α is the weight fraction at any temperature, W_t is the lubricant weight at any temperature, W_o is the initial lubricant weight, 'T' is the temperature of interest (in K), T_c is the inflection point of the sigmoidal curve (where the decomposition rate is a maximum and 50 % of the lubricant has been removed, in K), 'b' is a constant which depends on the lubricant and the heating rate, and $\dot{T}$ is the heating rate in °C/min. For EBS it has been found that the constant, 'b', can be expressed, empirically, as Equation 2.3 [46].

$$\alpha = \frac{W_t}{W_o} = \frac{1}{1 + \frac{T}{T_c}^b} \tag{2.2}$$

$$b = 0.5225\dot{T} + 17.607 \tag{2.3}$$

For a heating rate of 10 °C/min the value of 'b', when using Acrawax®, is 22.832. [46] states that values of 'b' in excess of 15 results in less than 10 °C variation in T_c. A T_c value of ~710 K (436.85 °C) is reported for Acrawax® at a heating rate of 10 °C/min in a 100 % N_2 atmosphere for samples with a green density of 7.05 g/cc. For practical purposes, complete delubrication can be assumed when 97 wt% ($\alpha = 0.03$) of the lubricant has been removed [46]. For an Fe-0008 ferrous alloy (0.8 wt% C + Fe) and 1 wt% Acrawax® lubricant a green density of 7.05 g/cc, delubrication is complete when a temperature of 826.76 K (553.61 °C) is reached as shown in Figure 2.6. Green density and T_c have a positive correlation, where T_c increases with increasing green density. The resulting sigmoid for various heating rates can be seen in Figure 2.6.

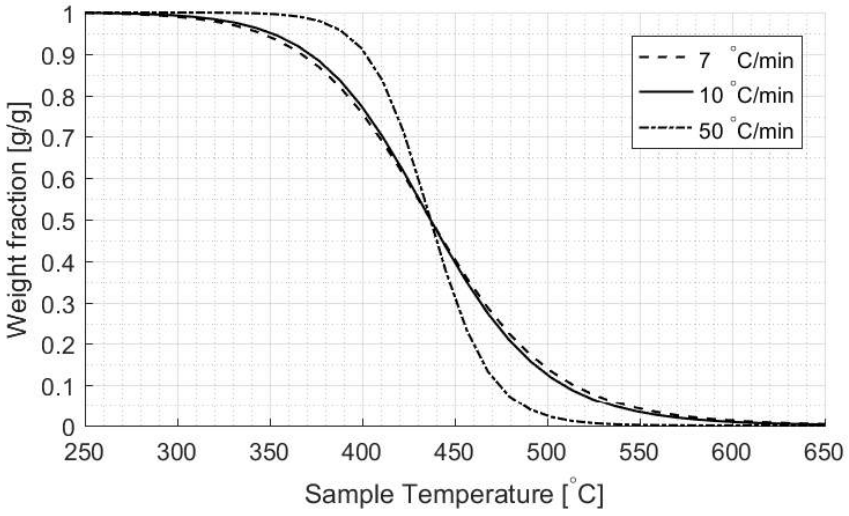

Figure 2.6: Delubrication of 1 wt% Acrawax® PM compact with 7.06 g/cc green density

Considering a worst case scenario for delubrication, it is assumed that the delubing furnace zone should have a maximum temperature of 600 °C. The window available for the lubricant to escape from the compact occurs between the characteristic temperature (T_c = 436.85 °C) and the maximum delubing temperature (600 °C) [46].

2.4 Infiltration

This section explains what sinter-infiltration is and how it is performed on PM parts and the mechanisms at work during infiltration. Finally, defects that may result from the infiltration process are discussed.

2.4.1 Advantages of Infiltration

As mentioned in Section 2.1.7, density plays an important (and beneficial) role in the properties of sintered parts. Copper infiltration is a relatively well-known process wherein a porous PM part, with an interconnected network of pores, is filled with a molten metal in order to achieve a fully dense composite [1:255, 3:390, 6, 7, 15, 16]. The porous part is produced using conventional PM techniques and is infiltrated either after sintering or during sintering (referred to as sinter-infiltration). The presence of the liquid phase during sintering significantly increases sintering rates by bonding grains together with a fast diffusion rate [1:248]. The liquid phase aids in densification through solution-reprecipitation wherein smaller grains are dissolved in the liquid phase and subsequently precipitate onto larger grains [1:249]. Resultingly, infiltration holds several advantages over conventional PM parts, such as; improved mechanical properties, increased machinability, increased thermal and electrical conductivity, decreased shrinkage, and improved corrosion resistance [1, 3:309, 7, 36].

Infiltration results in a relatively non-porous and more uniform density part as compared to conventional PM. Mechanical properties, such as toughness, strength and machinability, are influenced by the porosity and pore structure. Infiltration reduces the number of pores in a part and supplies more load bearing material, thus increasing the mechanical properties of the composite [1:375].

Similarly, the elimination of pores results in further advantages of infiltration. The machinability of PM parts is increased due to the filling of voids which decrease cutting forces and tool wear. The cutting forces and tool wear are further decreased when the relative ductility of the infiltrate, as compared to the matrix material, is lower. As a result, infiltration improves the surface finish of PM parts which are machined. Thermal- and electrical conductivity is greatly decreased by the presence of pores, therefore increased density results in increased thermal- and electrical conductivity [1:391]. The porosity of conventional PM parts provides a large surface area where corrosion can take place, therefore, a denser infiltrated part results in improved corrosion resistance [1:387].

In uninfiltrated PM parts, the cutting tool moves across the work surface removing material until it reaches a cavity, created by a pore. The machining

bit slips into the cavity and moves through it, subsequently coming into contact with the opposite pore wall. This sudden, small surface area, contact creates an impulse force in the part and the tooling. The stresses and heat of machining are locally intensified at the contact area causing material removal due to seizure and subsequent fracture or melting of the area. Fragmentation of the tooling and/or work surface can occur. Increased wear and a rougher surface finish result [7]. As the bit moves further through the part material the contact area increases and the pressure reduces, changing the active wear mechanisms to plasticity and mild oxidation/diffusion wear.

Infiltration improves machinability of PM parts due to the higher ductility of the infiltrant as compared to the matrix material and the filling of voids, as seen in Figure 2.7 [7], decreases cutting forces and tool wear whilst improving the surface finish [47]. The most common types of chips found when machining porous materials are serrated and discontinuous chips [48:13]. The infiltrant material filling prevents the occurrence of the impulse forces between the machining bit and the part being machined. Instead, the infiltrant filling creates a shaving which leads to a smoother surface finish [47].

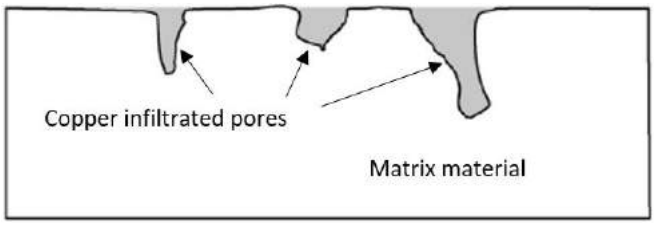

Figure 2.7: Voids filled with Cu adapted from [7]

2.4.2 Infiltration Technique

A technique called slug infiltration is commonly employed in ferrous PM. The slug method allows for high volume production, made possible by its ease of use and minimal post infiltration operations (e.g infiltrate material removal) [1:255]. The method consists of a single slug or disc, placed (usually) on top of and in contact with the porous part during sintering. Slugs have lower melting temperatures than that of the porous body and are once they melt, the liquid metal is drawn into the pores by gravity and capillary forces [49]. Therefore, the wetting ability of the infiltrant liquid is an important characteristic for infiltration [1:248].

2.4.3 Infiltration Mechanisms

The principal driving force of infiltration is that of capillary action[5] [3:309]. Capillary forces are determined by the contact angle between the solid and liquid phases. The contact angle is defined as the solid-liquid-vapour equilibrium angle. Contact angles are a means of measuring the wettability of a material, which refers to the ability of a liquid to spread out or form boundary surfaces when in direct contact with a solid.

The traditional definition of a contact angle, 'θ', is the angle created at a solid and liquid interface, as shown in Figure 2.8. Note that the contact angle between a solid and a liquid is measured from the inside of the liquid volume. A smaller contact angle results from a smaller surface energy and implies a larger wetting tendency. Liquids with contact angles smaller than 90° are considered wetting liquids and those with contact angles larger than 90° are considered non-wetting liquids [51].

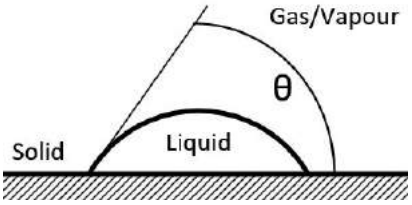

Figure 2.8: Young's contact angle

The contact angle is primarily influenced by the surface energy (or surface tension) of the liquid. The surface energy is defined as the energy required to increase the surface area of a substance by a unit amount [50:375].

The relationship between the surface energy and the contact angle is defined by Equation 2.4, the Young Equation, and Equation 2.5, the Young-Duprè Equation [51, 52]. In these equations; θ_{Y} is Young's contact angle, σ_{SV} is the solid-vapour surface energy, σ_{SL} is the solid-liquid surface energy, σ_{LV} is the liquid-vapour surface energy and $\mathrm{W_a}$ is the adhesion energy. From Equation 2.4 it can be noted that wetting angles occur when solid-vapour surface energies are larger than solid-liquid surface energies. Likewise, from Equation 2.5 it can be noted that wetting angles occur when adhesive forces are stronger than cohesive forces, as mentioned previously. Contact angles of 60° have been shown to ensure spontaneous infiltration, but contact angles of a few tens of degrees are considered to be good wetting interactions [52].

$$Cos(\theta_{\mathrm{Y}}) = \frac{\sigma_{\mathrm{SV}} - \sigma_{\mathrm{SL}}}{\sigma_{\mathrm{LV}}} \tag{2.4}$$

$$Cos(\theta_{\mathrm{Y}}) = \frac{\mathrm{W_a}}{\sigma_{\mathrm{LV}}} - 1 \tag{2.5}$$

[5]Capillary action (or capillarity) is when a liquid column rises, against gravitational forces, inside a narrow space [50:376]

The adhesion energy is defined as the energy required to (reversibly) separate a solid and liquid; it can be obtained by combining equations 2.4 and 2.5 [52] into:

$$W_a = \sigma_{SV} + \sigma_{LV} - \sigma_{SL} \tag{2.6}$$

When the liquid and solid, in contact with each other, chemically react (or are mutually soluble) dissolution of the solid into the liquid occurs. The contact angle becomes characteristic of the reacted surface, decreasing as a result of the dissolution, which removes/reduces the wetting barrier. Additionally, surface roughness can also influence the contact angle. This new contact angle is called the observed contact angle (θ) [1:256, 52]. The defect angle with the surface mean is defined as α, which when added to the Young's contact angle results in θ. This relationship is called the Wenzel Equation and is given in Equation 2.7 [52]. Figure 2.9 shows the difference between the observed contact angle and the Young's contact angle.

$$\theta = \theta_Y + \alpha \tag{2.7}$$

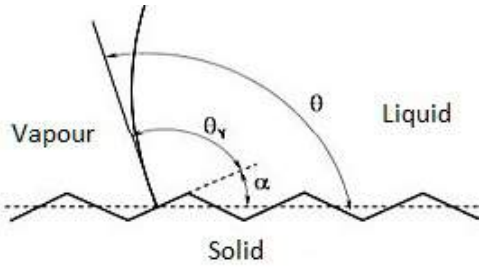

Figure 2.9: Observed contact angle schematic adapted from [52]

A non-traditional definition of a contact angle is that of the angle created between solid and liquid when a liquid enters a capillary (a very narrow pore channel) [51]. This definition is more easily applied to the infiltration process as compared to the traditional definition of contact angles because of the presence of capillaries in the metal matrix. The net result of the interaction between the cohesive and adhesive forces of a wetting liquid is that the liquid travels within the narrow passage.

Figure 2.10 shows the forces acting on a meniscus. The capillary rise is 'h', the capillary radius is 'R', the contact angle is θ, P_w is the pressure on the wetting side of the meniscus, P_{nw} is the pressure on the non-wetting side of meniscus and σ_w is the surface tension [50:376, 53, 54:33]. Performing a vertical force balance on the forces shown in Figure 2.10 results in Equation 2.8:

$$\mathrm{P_{nw}} \cdot (\pi R^2) = \sigma_{\mathrm{w}} \cos\theta \cdot (2\pi \mathrm{R}) + \mathrm{P}_w \cdot (\pi \mathrm{R}^2) \tag{2.8}$$

The capillary pressure, $\mathrm{P_c}$, is the primary driving force behind infiltration and can be expressed in terms of surface tension, σ_{w} by combining Equations 2.8 and 2.9, resulting in Equation 2.10 [53:60, 55].

$$\mathrm{P_c} = \mathrm{P_{nw}} - \mathrm{P_w} \tag{2.9}$$

$$\mathrm{P_c} = \frac{2\sigma_{\mathrm{w}} \cos\theta}{\mathrm{R}} \tag{2.10}$$

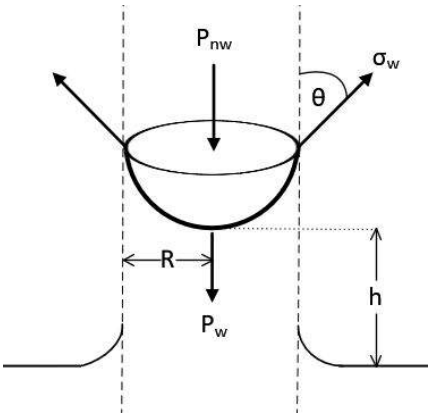

Figure 2.10: Force balance of forces acting on a meniscus

Capillary pressure can also be given in terms of the fluid column height, as in Equation 2.11 [55]. Where ρ_{l} and ρ_{g} are the densities of the liquid and gas respectively and gravitational acceleration is 'g'.

$$\mathrm{P_c} = (\rho_{\mathrm{l}} - \rho_{\mathrm{g}})\mathrm{hg} \tag{2.11}$$

Ignoring the effects of gas density, Equation 2.12 for the fill height, 'h', can be written by combining Equations 2.10 and 2.11 [53:59]:

$$h = \frac{2\sigma_{\mathrm{w}}}{\rho_{\mathrm{l}}\mathrm{gR}} \cdot \cos\theta \tag{2.12}$$

It is evident from Equation 2.10 and 2.11 that smaller pore radii result in larger capillary pressures, that result in an increased capillary fill height. Larger capillary pressures are therefore more desirable as they will result in more complete infiltration. To this end, several parameters in Equations 2.9 – 2.12 may be adjusted. Increasing the wetting surface energy will increase the capillary pressure. Likewise, decreasing pore radii, contact angles, gas densities or liquid densities will also increase the capillary pressure. Additionally, it is important to note that gravitational forces also contribute to the capillary pressure. Depending on the direction of infiltration gravity can increase or decrease capillary pressure. Gravity increases capillary pressure for infiltration occurring downwards.

Once the fill height is known, the filling time, '$\mathrm{t_f}$', is given by Equation 2.13 for an elliptical pore and can be reduced to Equation 2.14 for cylindrical pores [56]. Where μ is the viscosity, σ is the surface tension, θ is the contact angle, 'a' is

the pore width and 'b' is the pore length. The interested reader is referred to Appendix C.2 where viscosity values, decreasing with increasing temperature, for molten Cu can be found. In terms of infiltration, it is important to note that Equations 2.13 and 2.14 are only valid for pores that do not contain entrapped gas.

$$t_f = \frac{(2h^2\mu)}{\sigma Cos(\theta)} \frac{(a^2 + b^2)}{(a + b)ab} \tag{2.13}$$

$$t_f = \frac{2h^2\mu}{R\sigma Cos(\theta)} \tag{2.14}$$

From Equations 2.13 and 2.14 it can be seen that infiltration time increases with increased viscosity, fill height and decreased pore radii. This conclusion is quite intuitive as increased viscosity and smaller pores provide increased resistance to infiltrant flow. While it has been determined that smaller pores result in larger fill heights, smaller pores will also result in longer capillary fill times. On the other hand, sufficiently large radius pores result in insufficient capillary pressure preventing complete infiltration. It follows that there exists an optimum ratio of pore height to diameter (h/2R) which will result in maximum infiltration [7], i.e. through a balance between fill height and infiltration time optimum infiltration can be achieved.

2.4.4 Infiltration Defects

Sinter-infiltration can result in a range of defects. The cause and effect of these defects are studied in this section. Information for the identification, cause and remedy is given to assist in the troubleshooting of furnace operation. In the context of this project, high-quality samples are considered to be fully sinter-infiltrated, soot (from incomplete delubrication) and oxidation free. Figure 2.11 presents an example image of what is considered to be a high-quality sinter-infiltrated component.

Figure 2.11: High-quality sinter-infiltrated valve seat insert

Copper pooling: Copper pooling is identified by copper deposits on the surface of the PM part and the surrounding soot formation. Typically, copper pooling is caused by insufficient delubrication, which in turn is related to the dewpoint of the furnace atmosphere. If the lubricant does not burn-off completely the residual soot on the part adheres to the molten copper and prevents its diffusion into the steel matrix (due to the lack of wetting between the molten metal and carbon deposit), leading to the formation of copper pools on the part surface [8]. An example of copper pooling is given in Figure 2.12a.

Copper rundown: Copper rundown is the formation of copper droplets which when large enough run over the defect compact's surface, typically on a vertical surface. An example of copper rundown can be seen in Figure 2.12b. The surface in this area is clearly lightened by an increase in copper concentration. Likely causes for copper rundown are as follows [8, 19]. (1) Too high an infiltrate fluidity. (2) Excessive copper pooling as a result of soot formation can result in copper rundown. (3) Infiltration inhibition as a result of incorrect pore formation.

Copper balling: Copper balling occurs as an extreme case of copper pooling. Excessive soot build-up causes the liquid copper to form a ball resulting from the large contact angle between the soot and liquid copper. An example of copper balling can be seen in Figure 2.12c.

Erosion: Erosion is visible in Figure 2.12d. Erosion is identifiable by a rough surface texture with flowing type cracks and grooves near the edge of the infiltrant slug with subsequent darkening of the eroded area. Likely causes for Erosion are as follows [8]: 1) Too high an infiltration temperature and too long

an infiltration time can cause an increased amount of iron to dissolve in copper. 2) Using too small an infiltration slug. 3) Too low a slug density may result in a large residue skeleton and reduced the infiltration efficiency. 4) Vibrations can cause infiltrate powder segregation, which may result in erosion. 5) Using an erosion-prone infiltrate (resulting from its formulation). 6) Too low an infiltrate carbon content causing surface decarburization as the solubility of copper in iron increases as carbon content decreases.

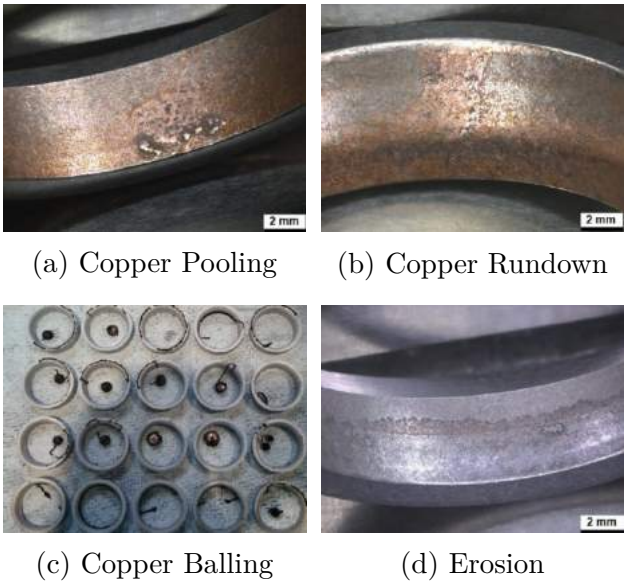

(a) Copper Pooling (b) Copper Rundown

(c) Copper Balling (d) Erosion

Figure 2.12: Typical Cu infiltration defects

Solid lubricant sweeping: Solid lubricants, such as MnS, are often added to the ferrous PM alloys to improve their machinability [1:340]. In Figure 2.13a a decrease in solid lubricant concentration is seen near the copper infiltration surface. This is a common occurrence during infiltration, where the solid lubricant particles are swept along with the liquid infiltrate towards lower areas in the part.

Staining and residue: In Figure 2.13b staining is visible, identified by a discolouration of the infiltrated part surface found near infiltrate residue on any surface of the sintered part [8, 40]. Staining results from incomplete delubrication due to the soot/residue formation (causing the darkening of the area) which prohibits the infiltrate's infiltration into the PM part. Sooting, can be caused by too low an infiltration temperature or low slug density. At lower temperatures, there is slower diffusion of the infiltrate causing incomplete infiltration which in turn can result in residue adherence. Sinter-infiltration time may also play a role and should be 20 – 35 min. An extreme case of sooting, called blistering, is caused by too high a heating rate in the reheat section [40].

Figure 2.13c is an example picture of black residue formation, on the top surface of the infiltrated proprietary alloy. The source and composition of this black residue are unknown, as the author was not been able to find literature that can effectively and completely explain the formation thereof, crumbly, residue. The source and causation of this residue are investigated in the subsequent section of this document. Figure 2.13d is a more severe occurrence of the residue formation in Figure 2.13c.

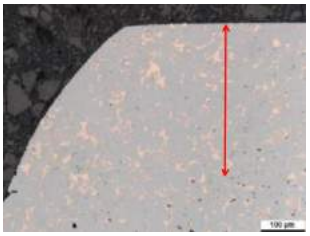

(a) Solid Lubricant MnS Sweeping

(b) Staining

(c) Residue (Image 1) [8]

(d) Residue (Image 2)

Figure 2.13: Typical Cu infiltration defects (continued)

Conclusion: Review of the possible causes of defects mentioned in this section indicates that the furnace atmosphere characteristics is responsible for most defects. Close control of the furnace dewpoint (especially in the preheat zone) and heating rates are required.

2.5 Alloying Element Effects

In valve seat applications, alloys with high heat and wear resistance are required. To this end, primary alloying elements used in ferrous valve seats are C, Cr, Mo and Mn. Additional to these alloying elements: Ni, W, Si, P, S, N, Co, Cu and Pb are also used [57–60]. These alloying additions can result in the presence of a range of different phases occurring in the bulk material. The phases can be plotted, on a phase diagram, to show how the material transforms on a microstructural level with changing temperature and composition. There are three types of transformations that can take place, 1) simple diffusion-dependant transformations where the number and

composition of phases do not change, 2) diffusion-dependant transformation where phase composition and/or the number of phases change, 3) diffusion-less transformation where a metastable[6] phase is produced [61].

With this basic background, each of the relevant phase diagrams for the Fe-Cu-C system is covered in more depth. More complex interactions, between the various additions of alloying elements, are likely to occur in the ferroalloy used in this project. Due to the proprietary nature of the alloy, the alloying additions are not known to the author and their interaction cannot be studied or researched. However, the behaviour of a pure binary (Fe-C and Fe-Cu) or ternary (Fe-Cu-C) system supplies valuable insight to predict the behaviour of a Fe-Cu-C system with various alloy additions. The ASTM standards B783 gives the limits of metallurgically combined carbon for several high Cu content steels, namely: FX-1000, FX-1005, FX-1008, FX-2000, FX-2005, and FX-2008. Additionally, Table X1.6 in ASTM B783 gives the standardized copper-infiltrated iron and steel properties for these alloys.

2.5.1 Fe-C Phase Diagram

Widely considered the most important alloy system is that of Fe-C, where graphite powder is added to the iron powder mixture to yield the solid solution strengthening effect of C in Fe. A portion of the metastable[7] iron-iron carbide (Fe-Fe_3C) phase diagram is presented in Figure 2.14 (adapted from [2:198, 37:198, 61:319, 62, 63]). There is a tendency in steels to form cementite (Fe_3C), rather than graphite, and therefore the Fe-Fe_3C phase diagram is used for steels [61].

[6] Metastable phases are non-equilibrium states which may persist for a very long time, and for all practical purposes can be considered constant.

[7] Metastable materials experience a microstructural change when at room temperature that is so slow it can be considered to remain the same compound indefinitely. For the Fe-C system, cementite is metastable at room temperature and will transform into α-Fe gradually through exposure to elevated temperatures (650 – 700 °C) for several years.

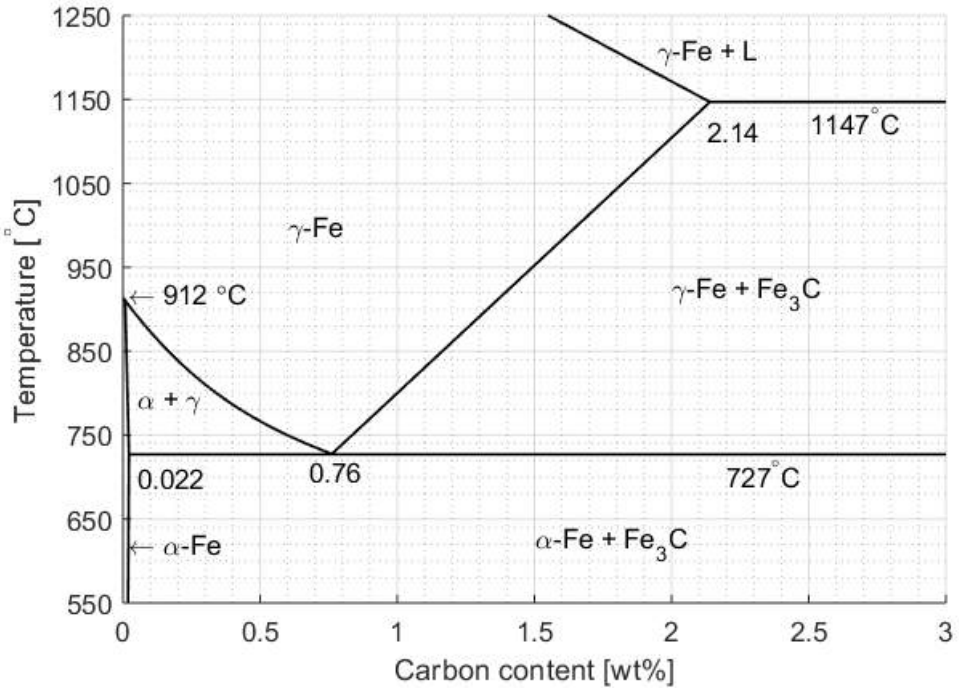

Figure 2.14: Fe-Fe_3C phase diagram adapted from [2:198, 37:198, 61:319, 62, 63]

Pure Fe at room temperature is in the stable form of ferrite (α-Fe). The α-Fe phase is a low solubility phase with a Body Centric Cubic (BCC) crystal structure [1:247, 61:319]. At room temperature carbon has a solubility of 0.008 wt% [37:198] in α-Fe. And at 727 °C carbon has a maximum solubility of 0.022 wt% for steels in α-Fe [61:320, 63].

At 912 °C α-Fe experiences a polymorphictransformation to austenite (γ-Fe), with a Face Centric Cubic (FCC) crystal structure. Carbon has a maximum solubility in γ-Fe of 2.11 wt% at 1148 °C. It can be noted that carbon's solubility in the γ-Fe phase is ~100 times more than in α-Fe [61:321]. The higher solubility in γ-Fe as compared to α-Fe is due to the different crystal lattice structures. FCC structures have larger interstitial areas than BCC structures. The larger FCC structure can accommodate more carbon atoms and impose smaller strains on the surrounding iron atoms [61:321].

Cementite (Fe_3C) is a metastable iron carbide that forms in steels.An eutectoid point exists at 0.76 wt% C and 727 °C whereupon cooling of the γ-Fe phase, a dual phase material containing α-Fe and Fe_3C is formed. The presence of cementite, which is very hard and brittle, in some steels can greatly enhance the strength of the material. The eutectoid transformation can be seen in Equation 2.15.

$$\gamma\text{Fe}(0.76\text{ wt\% C}) \longleftrightarrow \alpha\text{Fe}(0.022\text{ wt\% C}) + \text{Fe}_3\text{C}(6.7\text{ wt\% C}) \tag{2.15}$$

2.5.2 Fe-Cu Phase Diagram

The Fe-Cu phase diagram is presented in Figure 2.15 adapted from [64]. Pure Cu, which has a FCC crystal structure [64], has a melting temperature of 1084.87 °C. Cu has a maximum solubility in α-Fe of 2.2 wt% at 850 °C. In γ-Fe Cu has a maximum solubility of 8.2 wt% at 1096 °C, but at the sinter-infiltration temperature of 1130 °C the liquid phase Cu has ~9 wt% solubility in γ-Fe. Fe is mutually soluble in Cu, where up to 1.1 wt% α-Fe is soluble in Cu at 850 °C. A maximum of 4.1 wt% γ-Fe is soluble in Cu at 1096 °C. At the sintering temperature of 1130 °C γ-Fe has a solubility in liquid Cu of ~3.3 wt%. An eutectoid point exists at 3.1 wt% Cu and 850 °C whereupon cooling of the γ-Fe phase, α-Fe and Cu is formed. The eutectoid transformation is given in Equation 2.16.

$$\gamma\text{Fe}(3.1\text{ wt\% C}) \longleftrightarrow \alpha\text{Fe}(2.2\text{ wt\% Cu}) + \text{Cu}(1.1\text{ wt\% Fe}) \tag{2.16}$$

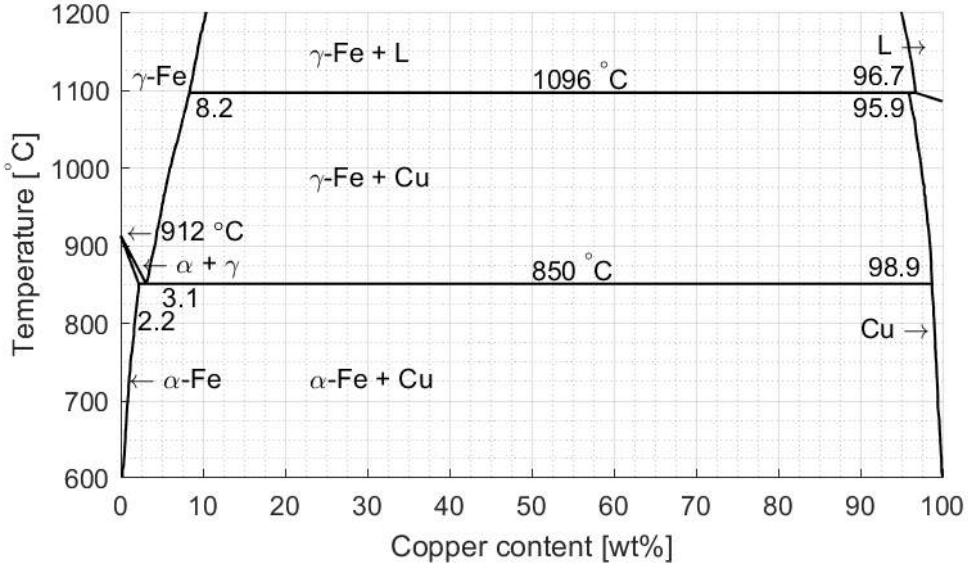

Figure 2.15: Fe-Cu phase diagram adapted from [64]

2.5.3 Fe-Cu-C Phase Diagram

It is known that the Fe-Cu-C system does not have any stable intermetallic phases [65]. It can be seen in Figure 2.16 that C solubility in γ-Fe decreases slightly with increasing wt% Cu. Similarly, Cu solubility also decreases slightly with increasing wt% C.

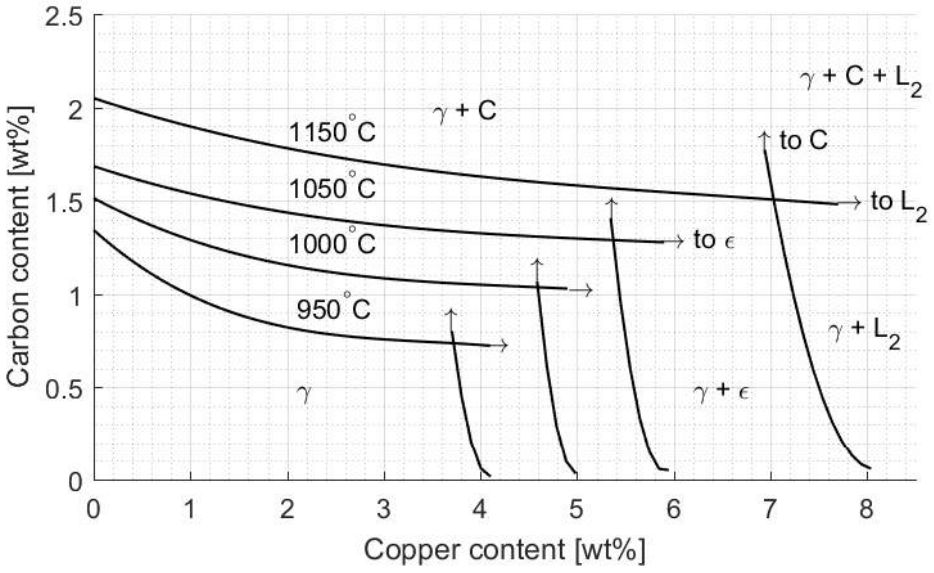

Figure 2.16: Fe-Cu-C Phase Diagram [66]

It is clear that a substantial portion of Cu will dissolve into the γ-Fe phase. Therefore it is important to determine the Cu solubility limit in the presence of carbon in order to ensure a fully dense part. The carbon steel alloy, which will be used in this study contains 0.5 – 1 wt% C. From the Fe-Cu phase diagram, Figure 2.15, at the sintering temperature of 1130 °C, a Cu solubility in γ-Fe of ~9 wt% Cu is noted. However, according to Figure 2.16 [66], at zero wt% C only ~7.4 wt% Cu is soluble in Fe. In the presence of carbon, the Cu solubility reduces even further. Taking into account the carbon content of the proprietary alloy mentioned previously, only ~6.6 – 7.2 wt% Cu will be soluble in the Fe-Cu-C system at the sintering temperature.

Chapter 3

Methodology

In this chapter, the research methodology for this study of copper infiltration of conventional ferrous PM is presented. In order to investigate the copper infiltration process of conventional PM parts, it was necessary to conduct the following investigations:

1. Investigate the effect of temperature and time on the delubrication process of conventional ferrous PM.
2. Investigate the role of the sintering furnace atmosphere on the delubrication process of conventional ferrous PM.
3. Determine the optimum delubrication temperature to be used in the pusher furnace at SU.
4. Investigate furnace control and parameters which result in successful, consistent and repeatable sinter-infiltration of conventional ferrous PM with Cu in the pusher furnace at SU.
5. Investigate composition and source of black deposits found on sintered ferroalloy samples.

All these investigations were designed based on an established industrial conventional PM process that uses copper infiltration. The iron alloy used in this project is a proprietary alloy of Bleistahl–Produktions GmbH & Co. KG. The alloy is a copper infiltrated, sintered high speed steel alloy, interspersed with intermetallic phases, used to manufacture valve seat inserts for use in internal combustion engines. An overview of the process, with the main quality control parameters for each step is given in Table 3.1.

Table 3.1: Ferroalloy production process specifications

Process step	**Equipment**	**Parameters**	**Control parameter**
Mixing	Mixer	Various proprietary Fe, alloy and 0.2 wt% lubricant powders	N/A
Die compaction	Uni-axial press	Fe alloy: ~750 MPa Cu slug: ~175 MPa	ρ_g(Fe) = 6.6 g/cc ρ_g(Cu) = 8.1 g/cc 22 wt% Cu
Sinter-infiltration	Continuous sintering furnace HeBoCoat® 10WF graphite plates	Isothermal hold: 1130 °C (30 min)	ρ_s = 7.5 g/cc 480 HV3 RCS[a] = 1000 MPa

[a]Radial crushing strength (RCS)

Bleistahl–Produktions GmbH & Co. KG have supplied this project with 60 research sized Fe-alloy and Cu samples. The ferroalloy samples have a diameter of ~20 mm, a thickness of ~9.4 mm and a mass of ~20 g. The copper discs have a diameter of ~20 mm, thickness of ~1.7 mm and a mass of ~4.4 g. Additionally, the alloy is also known to contain, an unknown quantity of, the solid lubricant[1] manganese sulfide (MnS). In order to replicate the sinter-infiltration process step in the laboratory, the pusher furnace and supporting equipment, housed in the M&M materials engineering laboratory is used.

Prior to evaluating the copper infiltration process, it was necessary to conduct maintenance and implement necessary improvements to the furnace. This included evaluating temperature and process gas control. The presentation of this study and the associated investigations is divided into three sections: 1) Chapter 4 presents the furnace maintenance and improvements that were required, 2) Chapter 5 presents the study of the delubrication process, critical for clean sinter-infiltration, and 3) Chapter 6 presents the copper sinter-infiltration study. Chapter 6 details the results of experiments conducted using different operating procedures for the pusher furnace. Finally, conclusions and recommendations are made through interpretation of the results presented in the above mentioned chapters. Details of equipment and experimental methods are included in each chapter, as relevant.

+

[1]Solid lubricants do not serve the same purpose as polymer lubricants, instead solid lubricants reduce wear and friction in relative motion applications [5].

Chapter 4

Sinter-infiltration Furnace

This chapter provides an overview of the pusher furnace system and the modifications thereof that were required in order to facilitate this project. Firstly, an overview of the pusher furnace system structure is given. The electrical and mechanical problems, pertaining to the pusher furnace, which was uncovered during the course of this project are outlined. The solutions implemented to remedy the problems are then detailed. Finally, the correct functioning of the pusher furnace system is validated through instrument calibration and profiling.

4.1 Pusher Furnace Overview

The sintering furnace used for the duration of this project is an R.M Catterson Smith[1] furnace. The furnace was owned by the Council for Scientific and Industrial Research (CSIR) of South Africa (SA), but was purchased by Powdermet (Pty) Ltd and is on loan to the M&M engineering department of SU. The overall dimensions of the furnace are w: 800 mm, h: 1600 mm, l: 2600 mm, with a furnace tube length of 1800 mm and a maximum operating temperature of the 1650 °C (provided that B-type thermocouples are used). Currently, K-type thermocouples are installed and thus the furnace has a maximum operating temperature of 1300 °C.

4.1.1 Physical Furnace Structure

Electrical Heating Elements

The furnace generates heat through Joule heating, or resistive heating, with three molybdenum disilicide ($MoSi_2$, also known as MOSI) elements which are wound onto the high heat furnace tube. Safe operation of the furnace requires the furnace operator to have knowledge of the heating elements' behaviour at elevated temperatures. For MOSI the onset of oxidation occurs at 400 °C, where SiO_2 is formed on its surface. Between 500 °C and 600 °C the oxidation

[1] R.M Catterson Smith has been out of business since 2009.

rate increases rapidly and as a result, MOSI elements must be kept in an inert atmosphere when above 500 °C. At 1723 °C the protective oxide layer of SiO_2 melts and $MoSi_2$ finally melts at 2230 °C [67, 68]. Accordingly, the safe maximum service temperature of these elements is chosen as 1650 °C.

Apart from the heating element oxidation behaviour, the electrical behaviour of the elements is also important for consideration by the furnace operator. It is known that the resistivity of materials change with temperature. The practical implication of changing resistivity is that the maximum power output of the heating system changes with resistivity. According to Ohm's law, Equation 4.1, if resistance increases and voltage remains constant the current will decrease. And according to Equation 4.2, the power output (and associated heating potential) of the furnace will be reduced as the current decreases.

$$R = \frac{V}{I} \tag{4.1}$$

$$P = I^2 R \tag{4.2}$$

On one wall of the furnace, there are four bolted conductor connections (junctions 1, 2, 3, and 4 which can be seen on the circuit diagram presented in Appendix A.1.1), connecting the transformer output phases to the heating elements. Junction 4 connects the third heating element, with a cable, to the first phase connection at junction 1, completing a three-phase delta connection of the elements. In order to determine the resistance of the heating elements at room temperature, a simple experiment was required[2]. The bridged connection between junction 1 and 4 was removed and a Gwinstek GPS-3303 power supply was connected to two junctions (1–2, 2–3, 3–4, 1–4) at a time, allowing current (3 A) to run through a single element only for each test. Voltage measurements were taken, with a BRYMEN TBM805 digital multimeter, over each of the two junctions to which the current was applied. It was seen that the voltage measured over junctions 1–4 was the sum of the voltages measured over junctions 1–2, 2–3, and 3–4, confirming that the furnace elements are connected in a delta configuration, with the addition of the external bridge between junctions 1 and 4. The heating element resistances, at room temperature, can be calculated from the measured voltages and known current using Equation 4.1. The heating element farthest towards the front of the furnace, was found to have a resistance of 210 mΩ while the central and rear elements have a resistance of 195 and 185 mΩ, respectively, at room temperature.

[2]Note that these resistances are too small to be accurately measured using a multimeter.

Using the resistivity of $MoSi_2$ it is possible to calculate the resistance of the heating elements at any temperature. Knowing what the resistances of the elements are at any one given temperature, in this case, room temperature (24 °C), a dimensional constant[3], 'z', of the heating element wires can be determined according to Equation 4.3. Using this constant for each of the elements the expected resistances, at any temperature where the resistivity is known, can be calculated, using Equation 4.4. The resistivity for $MoSi_2$ elements capable of heating to 1800 °C, given in [69], is plotted on the right-hand side y-axis of Figure A.1. The expected resistance of the heating elements are plotted on the left-hand side y-axis of Figure A.1. It can be seen that the element resistance increase ~10 times from room temperature to around 1200 °C.

$$z = \frac{R_{24}}{\rho_{24}} \tag{4.3}$$

$$R = z\rho \tag{4.4}$$

Furnace Tube

The furnace tube consists of three parts: the preheat zone tube, the high heat zone tube, and the cooling zone tube. The high heat zone tube is located inside a thermally insulated muffle, whereto the preheat and cooling zone tubes are connected through bolted flanges. The three heating elements are wound separately around the central, high heat zone, tube. The preheat and cooling zone tubes are heated through conduction, convection and radiation heat transfer from the heat generated at the high heat zone, approximately located in the centre of the furnace. The true material composition of these three sections is unknown. However, it is thought by the author of this document that the preheat zone and cooling zone are steel sections while the high heat zone tube is a refractory metal alloy. Accordingly, it can be assumed that the maximum service temperature of the central, high heat zone, tube is above that of the heating elements. Additionally, it can be shown that the preheat and cooling zone sections are within the safe service temperature range ($<$ ~450 °C) for carbon steel components [70:79].

Cooling Jacket

Surrounding a large portion of the cooling zone tube is a water cooling jacket. The cooling jacket has a water inlet on the lowest point of its circumference and an outlet at the highest point of its circumference, allowing the cooling section

[3]The resistivity dimensional constant is a constant characteristic of the cross-sectional area and length of the $MoSi_2$ wire.

tube to be encased by a water jacket. In previous years, the furnace had been decommissioned due to improper use of the cooling jacket, where water was supplied to it after the furnace had reached its set temperature. This resulted in the cooling section of the furnace tube cracking due to the thermal shock. The cracks allowed water to leak into the furnace tube which caused excessive oxidation of parts at high temperatures. The cooling section of the furnace tube was repaired, but not tested, before the onset of this project.

4.1.2 Heating Control System

The pusher furnace control system consists of two K-type thermocouples, a closed loop temperature controller, a temperature measurement (over-temperature) instrument, a thyristor unit, and a transformer.

Thermocouples

The pusher furnace thermocouples were procured from Temperature Controls (Pty) Ltd and calibrated on 22/05/2016 by Cape Metrology Field Services. An offset of 5 $\pm 1\,^{\circ}\mathrm{C}$ between the temperature controller and the over-temperature controller was determined, where the over-temperature controller presents the higher temperature. This offset has been taken into account for the duration of this project. The K-type thermocouples have a practical measuring range between -270 and 1260 °C. The K-type thermocouples have a standard error of +/- 2.2 °C or +/- 0.75 %, whichever is greatest. This means that above a temperature of 293 °C the percentage error must be taken. The temperature error therefore at the sintering temperature of 1130 °C is +/- 8.5 °C. Furthermore, the thermocouples both have a length of 1800 mm and a diameter of 6 mm.

Temperature Controllers

The two controllers of the furnace control system are RKC SA200 and a RKC Rex-D100 temperature controller units. One K-type thermocouple is installed on each of these controllers. The RKC Rex-D100 is a proportional integral differential (PID) controller, with the purpose of controlling the furnace temperature. The unit has an accuracy of $\pm 0.3\,\%$ of the temperature span +1 digit This gives an accuracy of $\pm 4.4\,^{\circ}\mathrm{C}$ at the sinter-infiltration temperature of 1130 °C. The unit outputs a voltage signal of 0 – 5 V, received by the thyristor unit which then scales the power output accordingly. The RKC SA200 unit is a temperature measurement unit, with alarm capabilities for over-temperature protection. This unit was used during the course of the project for the purposes of measuring sample temperatures at locations throughout the furnace.

Thyristor

The thyristor unit is located in the electrical circuit of the heating control system between the PID temperature controller and the transformer. The electrical circuit can be seen in Figure A.2. The presence of the transformer in the circuit requires that the thyristor be capable of supplying power to an inductive load[4]. The heating elements have a certain resistance, and drawing a certain current at a given supply voltage, thus resulting in a required power supply capacity. The current per phase is measured by an induction ammeter, seen in the circuit diagram, which connected to the incoming phases and located between the wall socket and the thyristor unit. Therefore the ammeter will display the current before it is stepped up by the transformer and not the current seen by the elements. The thyristor has a rated output current of 25 A.

The thyristor unit consists of three thyristors (solid-state semiconductors), one on each phase. The thyristors work together, combining the phases in such a way that the desired output voltage, and as a result, desired power is obtained. The thyristors combine the three-phase inputs by conducting a single-phase current over 120° of its sinusoid. The power output is controlled by shifting the conducted part of the sinusoid. This shift is realised by a shift (of 0 – 180°) in the trigger or firing angle, where the thyristor starts conducting. From Ohm's law, Equation 4.1, it can be seen that for a constant load resistance a larger voltage will result in a larger current. The larger current in turn results in a larger power output, according to Equation 4.2.

Thus, for maximum power output, the conducted sinusoid must include the peak of the full wave voltage. When the voltage peaks of all three phases are combined, the maximum power output of the thyristor unit is delivered, resulting in the waveform presented in Figure A.4.

Transformer

The transformer, a Transformer and Electrical Co. Ltd. 14 KVA NO. JC 418, is required between the thyristor and the heating elements to step up the current because the elements are low resistance and require a high current in order to produce a high power output. The primary side voltage of the transformer is 415 V which is stepped down to 75 V. That is a 5.53 step down ratio for voltage. Thus, a 5.53 step-up ratio for current. The thyristor unit can output a maximum current of 25 A, thus at this limit, the current seen by the elements would be 133.25 A. Additionally, the transformer primary and secondary are connected in delta.

[4] A inductive load is a load which resists changes in current which is manifested by the current lagging the voltage.

4.1.3 Process Gas System

A diagram of the gas flow system in question was created and is presented in Figure B.1. The furnace tube has three (A, B, C) points of atmosphere inlet. One inlet is located 170 mm from the furnace tube inlet (A). The second inlet is located, between the high heat and cooling zone, at (B) 450 mm from the furnace tube outlet. The third inlet is located 115 mm from the furnace tube outlet. The muffle[5] has one atmosphere inlet (D) and exhaust (E), located above the high heat zone. The gas system contains three permanent variable area flow (VAF) meters, one measuring N_2 flow and two measuring H_2 flow. The N_2 flow meter is an Aalborg VAF meter, 034-39-CA, with a Carboloy float. The H_2 flow meters are both Aalborg VAF meters, 102-05-SA, with sapphire floats.

4.2 Operational Problems

This section outlines the problems, with the pusher furnace, encountered through the course of the project.

4.2.1 Required Sintering Temperature Unattainable

Initial inspection of the pusher furnace revealed that a maximum temperature of only 1000 °C was attainable (without the use of the cooling jacket) after 32 hours of heating. Sinter-infiltration of the ferroalloy requires a high heat temperature of 1130 °C. Several system components were investigated during the solution of the above-mentioned problem. These components are listed below and further detailed in Section 4.3. The validation of the modifications is detailed in Section 4.4.1, with temperature profiling in Section 4.4.2.

4.2.2 Process Gas Flow Inaccurate

During initial furnace operation testing, a discrepancy between the expected volume flow rate from the N_2 cylinder and the volume flow rate indicated by the rotameter was noticed. A test, detailed in section 4.3.4, based on the ideal gas law was conducted to determine if the discrepancy truly existed. Following the confirmation of the process gas flow inaccuracy, modifications were made to the process gas system, also detailed in Section 4.3.4. Calibration of the process gas system was done, and is detailed in Section 4.4.3.

4.2.3 Sooting of Samples

Incorrect or incomplete delubrication results in blackened sample surfaces. In order to supply the required oxygen-containing species for delubrication to

[5]The muffle is the isolating and insulating material of the furnace chamber.

occur a bubble column reactor is often employed to add moisture to the process gas entering the preheat zone of the furnace. A bubble column reactor was designed, build and installed in the process gas system. The calculations for this process are detailed in Appendix B.1.2. A different method to continuous furnace control and operation, in conjunction with the moisture bubbler, was explored. This alternative method was named transient furnace atmosphere control and is detailed and validated in Section 6.2.

4.2.4 General Problems

Equipment practicality issues were addressed and system safety upgrades were conducted. The upgrades are detailed in Section 4.3.6.

4.3 Furnace Modification

The modifications to the pusher furnace system that were required for resolution of the problems presented in Section 4.2 are detailed in this section.

4.3.1 PID Controller Output

Circuit Rewiring and Documenting: To ensure that all the electrical connections were in good condition, rewiring of the furnace components was performed and a circuit diagram was drawn up for the furnace, which can be viewed in Figure A.2.

PID Controller Reprogrammed: The PID controller's operator manual was consulted and the parameters for its output to the thyristor unit was reprogrammed to ensure correct operation. The parameters can be seen in Table A.1.

Validation of PID Output Voltage: During manual operation of the PID controller, the control signal of 0 – 5 V can be manipulated to control the furnace power supply. In order to confirm that the PID controller is outputting the correct control signal, the output voltage was measured using a BRYMEN TBM805 digital multimeter. The output was confirmed to be functioning suitably with an output voltage range of -0.05 – 4.65 V.

4.3.2 Furnace Heat Retention

Lowered Gas Flow Rate: The furnace had in previous years operated at the required temperature (1130 °C) and therefore it was thought that too large a gas flow rate was currently being used, resulting in large heat losses at higher temperatures. The process gas flow rates were considerably reduced, from

4.0 – 2.0 l/min for N_2 and from 2.0 – 0.5 l/min for H_2. Previously the furnace reached 800 °C in 3 hours and a temperature of 1000 °C in 32 hours. The furnace now reached 800 °C in 2.5 hours and could reach a temperature of 1130 °C in 22 hours.

Although the furnace could now reach the sought after set temperature, the reduction in gas flow had too small an impact on the heating capacity of the furnace to be the root cause of its problematic functionality. Additionally, the low gas flow rates had resulted in the furnace's inability to produce unoxidised samples.

4.3.3 Thyristor Output

Mr P Pieterse, of the electrical department at SU, was consulted on the operation and testing of the Eurotherm thyristor unit. The Eurotherm thyristor specifications are 380 V rms phase-to-phase and 25 A/phase. The thyristor unit, while part of the pusher furnace system, is supplied with three-phase power from the ESKOM grid with a root mean squared (rms) phase-to-phase voltage of 400 V at 50 Hz (230 V rms phase-to-neutral).

Potentiometer Replacement: In situ Measurements showed that an initial, correct, voltage output of 400 V was measured between the output phases of the thyristor unit. Upon heating, this voltage dropped to ~100 V within 2 hours, corresponding to a temperature of ~700 °C. Investigation of the thyristor unit revealed that the potentiometers responsible for the input/output scaling on the thyristor controller were faulty. The potentiometers were replaced but did not solve the drop in output voltage.

Output Waveform Analysis: Mr P Pieterse, assisted by Mr AP Scholtz, conducted a laboratory experiment to determine if the output of the thyristor unit has the correct waveform, as seen in Figure A.4 for maximum power output. In order to test the thyristor unit waveform, each thyristor output was connected to an electrical heating element, with a 3 kW rating. A Gwinstek GPS-3303 power supply unit was used to supply the 5 V control signal to the thyristor unit. A Tektronix TDS 2001C oscilloscope was used to measure the phase-to-neutral output of the thyristor.

It was possible to see from the oscilloscope display that two of the three phases displayed faulty triggering waveforms, where under maximum desired output conditions phase shifted (conducting along the wrong portion of the sinusoid) or low power trigger angles were observed. The erroneous triggering resulted in a maximum voltage output (line-to-line) of ~100 V where under correct triggering, for full power operation, the voltage output should be 400 V. The reduced voltage output is therefore directly responsible for the reduced heating capability of the furnace. The cause of the faulty output was never determined,

but it is suspected to be a result of component failure due to ageing. It was concluded that the thyristor unit should be decommissioned due to the time and cost required in determining the faulty electronic components and repair or replacement of the ageing equipment.

Thyristor Replacement: A new thyristor unit, a Tele Haase TST3, was procured as a replacement. Calculations for the required power and current capabilities of the thyristor are included in Appendix A.3.2. The TST3 unit was chosen with careful consideration of cost, current rating, power rating, control input and inductive load capabilities. The TST3 unit has a 16 kW capacity which can be controlled by a 0 – 10 V or a 0 – 20 mA control signal. Voltage control was chosen due to the limitation of the PID controller, which can only output a 0 – 5 V signal. An op-amp circuit, which is included in the circuit diagram of Figure A.2, was built to amplify the PID controller's voltage control signal for the new thyristor unit. Calculations for the specifications of the op-amp circuit are given in Appendix A.2.2.

4.3.4 Process Gas System Inaccuracy

Flow meter inaccuracy test: In order to test for the process gas system inaccuracy, the N_2 flow was set to 20 scale markings on the rotameter and a regulator pressure of 50 kPa. Measurement of the cylinder pressure over time allowed the use of the ideal gas law, Equation 4.5, to determine the actual (average) volume flow rate of N_2 supplied; 4.75 l/min at 20 scale markings and 50 kPa.

$$PV = mRT \tag{4.5}$$

The supplier calibration curve for the N_2 Aalborg rotameter indicated that a volume flow rate of 3.33 l/min could be expected at 20 scale markings and 50 kPa. Figure B.3 shows the measured cylinder pressure drop (solid line) and the theoretical pressure drop, over time, for a volume flow rate of 3,33 l/min as indicated by the supplier calibration curve. A straight line with Equation 4.6 was fitted to the data, where $P_{cylinder}$ is the starting cylinder pressure in kPa and 't' is the time in minutes. The curve fit indicated that the cylinder pressure drops ~8.9 kPa/min when using 20 scale markings of flow at 50 kPa.

$$P = P_{cylinder} - 8.9t \quad [kPa] \tag{4.6}$$

The error (1.42 l/min) between the calibration data and the calculated volume flow rate was determined. It was unclear whether the discrepancy in volume flow rate was caused by inaccurate regulator pressure or wrongful calibration data. It was decided that new calibrations for the N_2 and H_2 flow meters should

be performed with closely controlled line pressure. The calibration process is detailed in Section 4.4.3.

Process gas system additions and modification: A capillary type mass flow meter, Alicat M-5SLPM-D/M, was procured and employed to measure data for the new calibration curves. Additionally, 100 kPa Rhomberg pressure gauges were installed in-line directly after the gas cylinder regulators and directly before the Variable Area Flow (VAF) meters.

4.3.5 Sooting of Samples

The burn-off of lubricants require the presence of oxygen species in the furnace atmosphere, as mentioned in Section 2.2. Oxygen is supplied in the gaseous form by O_2, CO, CO_2 and H_2O in the sintering atmosphere [1]. A common practice to introduce oxygen into the delubing section of the furnace is to bubble the process gas through distilled water [71, 72]. A bubble column reactor, a schematic of which is shown in Figure 4.1, adds H_2O vapour to the carrier gas as it bubbles a carrier gas through a water reservoir.

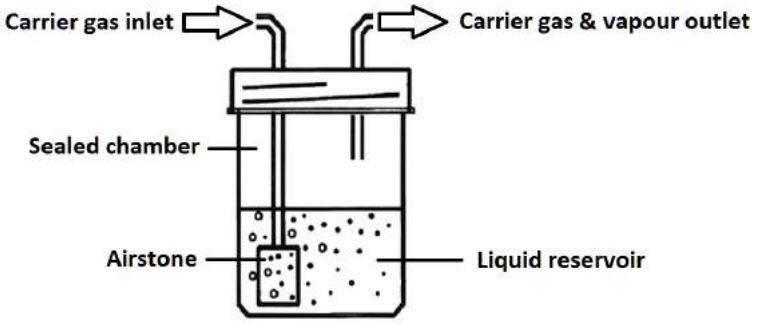

Figure 4.1: Bubble column reactor schematic

In order to build and install a bubble column reactor in the process gas system, several design specifications were required to be obtained through calculations. The calculations to determine the gas flow rate of the process gas (H_2-N_2 mixture) throughout the various section of the furnace are given in Appendix B.3.3. The gas flow rate of process gas through the preheat or delubing section is subsequently determined through these calculations. This flow rate is used as an input to calculate the mass transfer of water vapour to the process gas when passing through the bubbler. These calculations are presented in Appendix B.1.2. A summary of the calculation of the mass transfer for water vapour to the preheat zone process gas, as per Appendix B.1.2, is presented here. A preheat zone dewpoint of 8 °C is required, as indicated by [40]. This gives a required saturation pressure of 1.073 kPa at the preheat zone. The partial

vapour pressure[6] of $H_2O_{(g)}$ must be equal to this saturation pressure[7] in order to fix the dewpoint at 8 °C. The required absolute humidity is calculated, which indicates a required vapour mass flow rate of 42.56 mg/min.

The total moisture content of the bubbler outlet is the sum of all the moisture content transferred, through diffusion, to the dry process gas bubbles whilst moving through the water column. The velocity of a carrier gas bubble in liquid water is required in order to determine the time available for diffusion to take place. The process gas bubbles are assumed to be perfect spheres with a 5 mm diameter, as supported by visual observation. The bubble diameter is assumed to remain constant throughout the water column, unaffected by the pressure change experienced. The terminal velocity, for a 5 mm diameter bubble, is calculated to be ~104.4 mm/s. It is assumed that the bubble reaches terminal velocity in a negligible time, a conservative assumption as any lower velocity will result in an increased contact time between the bubble and the water column which will result in additional diffusion. The process gas bubbles are assumed to rise vertically, without perturbation, and do not interact with the bubbler walls or adjacent bubbles in any way. The bubbles, therefore, travel through the entire water column at terminal velocity. The bubbler is assumed to have a water column height of 200 mm, therefore the terminal velocity being 104.4 mm/s a bubble will be exposed to the liquid medium for 1.92 seconds.

A mass diffusion coefficient is calculated for the mass transfer between a process gas bubble of (80:20) N_2:H_2 and the liquid H_2O. It is found that the mass diffusion coefficient is 17.2 mm^2/sec and is assumed constant throughout the water column. The penetration depth allows the depth of diffusion to be determined at any given time. The penetration depth is a straight line with a gradient equal to the concentration gradient at the bubble-liquid interface. It starts at the bubble-liquid boundary and ends where it intercepts the initial concentration of moisture in the bubble. This distance, along the initial concentration line, is the penetration depth which has been calculated to have a value of 0.445 mm. The concept of penetration depth is valid as long as no mixing occurs within the bubble.

Analysis of the penetration depth considered two scenarios. The first scenario, where the penetration depth results in a volume of bubble exposed to liquid vapour and a portion of volume which remains dry. The second scenario, where the full depth of the bubble is penetrated by the water vapour and some vapour content profile exists over the bubble radius. It was calculated that the

[6]The partial pressure is the pressure which will be exerted if a single constituent gas were to exist alone, occupying the same volume as the mixture, at the same temperature [43].

[7]Dalton's law states that the total pressure of a gas mixture is equal to the sum of the partial pressures of the individual gases [43].

penetration depth (for the current bubbler configuration) results in the second scenario, where vapour penetration occurs up to the centre of the bubble. The moisture content of the entire bubble as it reaches the end of the water column was calculated to be 0.0011 mg.

If all the flow to the preheat zone were to pass through the bubbler, ~850 bubbles would be generated per second and result in ~54 mg/min water vapour entering the preheat zone. It was calculated previously that only 42.56 mg/min of vapour is required at the preheat zone for a dewpoint of 8 °C. Thus, depending on the additional (over and above the supply of a desired dew point) water vapour required for delubrication, only a portion of the total flow to the preheat zone must pass through the bubbler in order for sufficient saturation of the process gas. A bubbler carrier gas flow of 2.6212 l/min results in the correct vapour mass flow rate and therefore 0.7124 l/min of process gas destined for the preheat zone must bypass the bubbler to maintain a dewpoint of 8 °C. A summary of the design specifications, as per these calculations for the bubbler, is presented in Table 4.1.

Table 4.1: Bubbler specifications

Bubbler temperature:	20 °C
Water column height:	200 mm
Carrier gas temperature:	20 °C
Carrier gas gauge pressure:	50 kPa
Carrier gas flow rate:	2.6212 l/min
Bypass gas flow rate:	0.7124 l/min
Maximum moisture content:	54 mg/min

The excess capacity available for the delubrication process, 11.4 mg/min, can be determined from the difference between the maximum moisture content achievable with the bubble column reactor, 54 mg/min, and the required moisture content for the correct dewpoint, 42.6 mg/min. It is important to note here that these calculations only take into account the moisture addition necessary to maintain the dewpoint of the inlet process gas flow and does not take into account the quantity of oxidation species required for the delubrication process.

4.3.6 General Upgrades

After careful consideration, it was decided that a rebuild of the furnace equipment would be beneficial to the completion of this project, providing for a functioning, safe, and organized workspace.

Furnace redesign: Originally the furnace control system (housed inside a

steel filing cabinet), the transformer, LPG cylinder and muffle were all separate units. A solution was designed and implemented in which all of these components could be integrated into a stand-alone unit. Images for comparison between the old furnace build and the rebuilt furnace are presented in Figure 4.2.

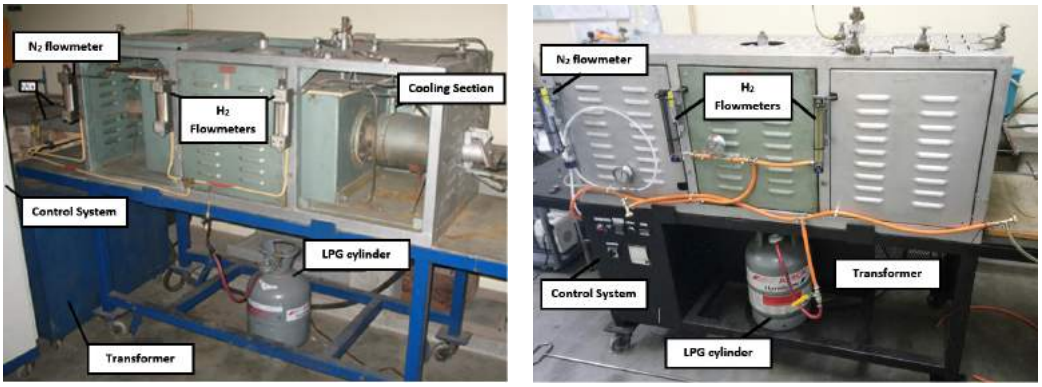

(a) Old furnace build (b) New furnace build

Figure 4.2: Furnace refurbishment comparison

Electrical earthing: During troubleshooting of the electronics and control system, it was found that there was no earthing wire connected to the furnace. An earthing wire was installed during the rewiring of the furnace.

Extractor fan: An extractor fan was installed in the room above the pusher furnace in order to extract process gasses and products of combustion that may be dangerous or harmful to persons from the furnace room.

Improved burners: The burner flames were rigid in their positioning and would often ignite the process gas behind the furnace tube gates, causing a blow-out. The blow-outs had caused viewing glasses on the furnace gates to break, as seen in Figure 4.3a. The issue was remedied by replacing the problematic burners with custom-made burners that burn-off H_2 above the tube gates. The new burners were made using short aluminium piping wherein a thread was tapped, allowing for small gas nozzles to be attached to the ends of the aluminium pipes. The aluminium pipes were brazed onto hose tails which connect to clear flexible PVC hosing that allows positional adjustment of the burner flames. Concerns about the safety of the clear PVC piping set-up emerged after which an investigation, presented in Appendix B.1.3, was conducted. The investigation proved that the clear PVC piping was safe to use in the LPG system. The old and new burner flames can be seen in Figure 4.3.

(a) Furnace gate blow–out (b) Old burner flame (c) New burner flame

Figure 4.3: Burner flames comparison

Track design: the original steel rod used to push the sample boats through the furnace required that the entrance gate is opened for every push of the sample boats, thus causing atmospheric air to enter the furnace and process gas to escape the furnace. Additionally, the rod could not be left inside the furnace tube as it forced the entrance gate to remain open during the time it was inserted into the furnace. Furthermore, the rod proved to be hazardous as it becomes heated inside the furnace and is then removed from the furnace where it can contact flammable materials or cause injury to persons inside the lab. The furnace track design was modified in order to allow pushing of sample boats using a thermocouple, without the need to open the tube gates, which also serves to provide a more accurate estimate of sample temperature.

Tube gate redesign: The tube gates required redesign in order to interface better with the furnace tube, allowing minimal gas flow from escaping around the periphery of the furnace tube entrance and exit. The new tube gate design incorporates tempered glass viewing windows. The design incorporates a silicone rubber gasket which allows relative movement between the viewing glass and the tube gate it is attached to, thereby reducing the possibility of cracking under thermal stress.

LPG cylinder location: The risk of damage to the LPG cylinder and its piping is reduced by securing it in the frame of the pusher furnace assembly.

Drain sealed: An open drain near an LPG gas system is a safety hazard because LPG is heavier than air, an LPG leak will enter the drainage system and could be ignited elsewhere causing major damage to buildings and/or people. A drain cap was manufactured and installed in the furnace room, replacing the grid that was installed there previously.

4.4 Validation of Sintering Furnace Operation

4.4.1 Thyristor Comparison

A comparison was done between the old and new thyristor's heating capabilities are given in Figure A.6. Note that this comparison was done without the use of the cooling section (i.e. the water jacket was not operational in both instances). As can be seen from Figure A.6 the new thyristor unit resulted in much faster heating of the furnace. The furnace could now reach a set temperature of 1130 °C in ~30 min. The old thyristor unit was only able to reach 1130 °C in ~22 hours and could not maintain this temperature once the H_2 gas flow and press–and–sinter samples were introduced to the furnace system.

4.4.2 Steady State Temperature Profiling

The pusher furnace at SU is typically used for short periods of time during research experiments, as opposed to industry applications where furnaces would run continuously. Industry furnaces can take days to reach a steady state and are only switched off for critical maintenance. At SU, because of the infrequent use of the pusher furnace, the time required to reach a steady state condition is of interest.

Axial Steady State Temperature Profile

In order to determine when the furnace reaches a steady state, the furnace high heat zone was first brought up to a set temperature of 1130 °C, from room temperature. Thereafter a second thermocouple was inserted into the preheat zone. The temperature in the preheat zone was monitored and it was found that the temperature stabilised, to < 1 °C change over 10 min, 5 hrs after the furnace heating was switched on. In order to confirm whether this state was sufficiently stable, the furnace was left at the 1130 °C setpoint for a total of 24 hours whereafter the temperature profile was again measured. The setpoint temperature remained at 1130 °C (see Section 4.1.2) whereas the temperature distribution over the entire length of the profiles showed a negligible, 3.45 %, change over the entire temperature profile. The error calculation is presented in Equation 4.7.

$$\text{err} = 100 \cdot \sum_{i=1}^{n=32} \left(\frac{T_{i,24hrs} - T_{i,5hrs}}{T_{i,5hrs}}\right)/n = 3.45\% \tag{4.7}$$

It was assumed that when temperatures along the furnace tube changed by less than 1 °C, the resolution of the furnace controller, over 10 min, a steady state had been reached. A temperature profile of the furnace tube in the

axial direction was created through taking temperature measurements on the inside of the furnace tube using the O/TEMP thermocouple at 50 mm intervals along the length of the furnace tube. The thermocouple was resting on the base of the furnace tube and the track was left inside the furnace for the measurements. The resulting temperature profile is presented in Figure 4.4. The centre of the high heat zone is located at 850 mm from the tube inlet, where the maximum temperature is found. Additionally, it was noted that the minimum time required for thermocouple readings to stabilise was ~3 min (hold times of up to 10 min were considered).

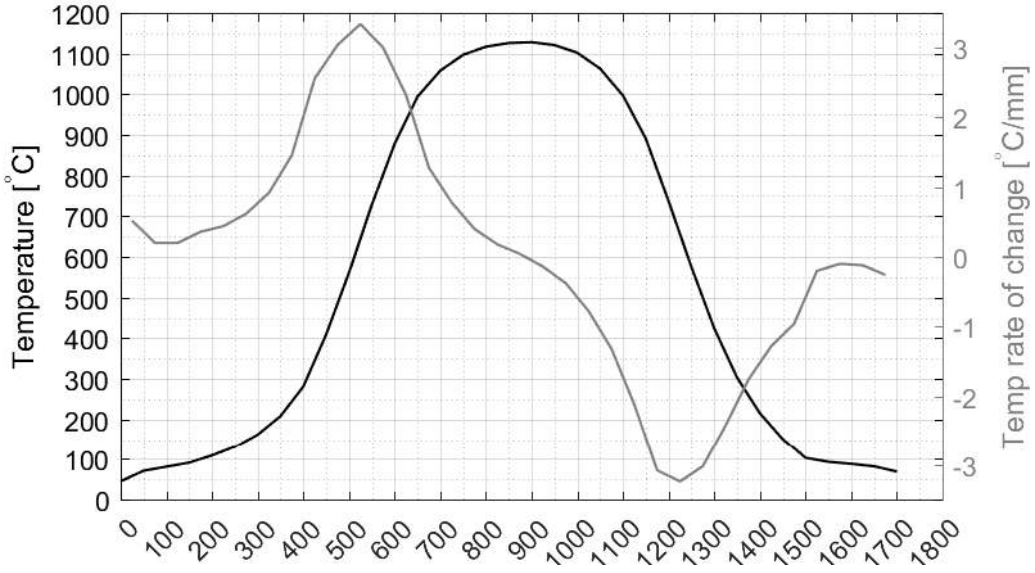

Figure 4.4: Axial temperature profile of the pusher furnace tube

Numerical differentiation was performed on the temperature profile of Figure 4.4. The results, the rate of temperature change over the axial direction of the furnace tube, is plotted on the secondary y-axis of Figure 4.4. In order to visualise the data better, an example can be made from the data presented in Figure 4.4, consider a sample boat inside the furnace tube. The sample boat is 100 m in length and is currently in position between 475 and 575 mm, where the rate of temperature change is a maximum. In order to determine the difference in temperature between the front and back of the sample boat, the area under this part of the plot must be calculated. This results in a temperature difference of 317 °C between the front and the back of the sample boat. A similar calculation can be performed across a sample of 25 mm diameter. The resulting, maximum, temperature difference across a 25 mm sample is 82.5 °C. This maximum temperature gradient occurs in the delubrication and cooling zones at a distance of ~525 mm and ~1225 mm at ~650°C).

Cross-sectional Steady State Temperature Profile

In order to determine the cross-sectional temperature profile in the pusher furnace tube a jig was designed and manufactured to accurately locate the thermocouple for temperature measurements over a cross-sectional area of the pusher furnace tube. The thermocouple becomes yielding due to the high temperatures inside the furnace tube and as a result, requires support in order to perform temperature measurements at specific locations. A total of 25 temperature measurements were performed. The measurement locations numbered 1 – 25, are given in Figure 4.5.

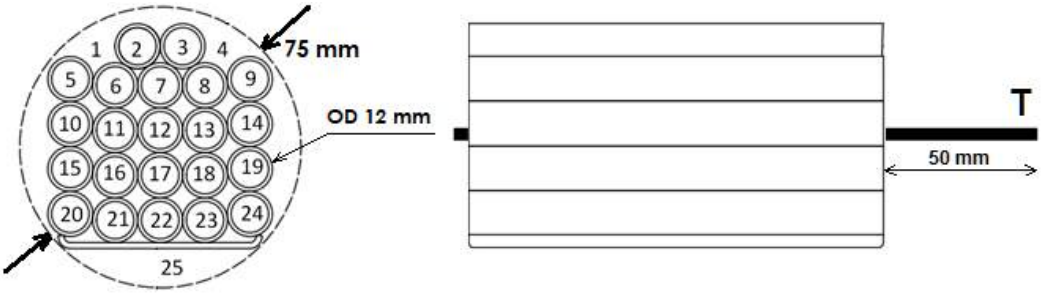

Figure 4.5: Pusher furnace cross-sectional temperature profile measurement locations

As can be seen from the figure, four rows of five 12 mm outer diameter pipes are located side-by-side across the width of the boat. The outside two pipes are located 2.4 mm higher than the inside three pipes, due to the curvature of the furnace tube. A fifth layer is created using two tubes, each shifted a single tube radius from the assembly's horizontal centre line.

With a thermocouple diameter of 6 mm and assuming temperature measurements are taken at a central point on the tip of the thermocouple, the height of the first row of temperature measurements can be calculated. The height of the first row of temperature measurements is taken from the lowest point on the inside of the 75 mm furnace tube. Therefore it can be shown that the outside two measurements of the first layer are located at a height of 15 mm above the lowest point in the furnace tube, while the central three measurements in this layer are located at 12 mm above the lowest point.

The further three layers are located at increments of 12 mm above the first layer and the last layer is located 10.4 mm above the last complete layer. The temperature measurements were taken approximately 50 mm outside of the jig, in order to reduce any impact the jig may have on the measurements and/or the temperature profile.

The results were plotted in Figure 4.6. It can be seen from this figure that there is a temperature gradient present in the cross-section of the furnace, as indicated by the arbitrary colour scale used. The data indicates that 1) the set temperature is not constant throughout a cross-sectional plane of the furnace tube, 2) there is a temperature gradient vertically as well as horizontally, 3) the set temperature is at least 12 °C lower than the maximum temperature within that cross-sectional plane, 4) the central temperature is ~5 °C lower than the temperatures measured closer to the edges of the furnace tube.

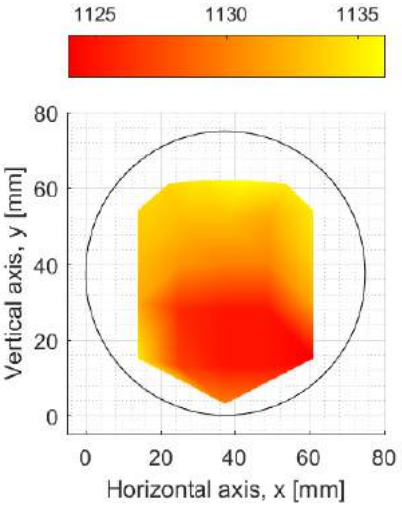

Figure 4.6: Jig-measured cross-sectional temperature gradient in the high heat zone

Preliminary sinter-infiltration experiments indicated the presence of a larger temperature gradient, as compared to the measurements performed with the jig, in the pusher furnace tube when using a track. This was supported by thermal imaging and thermocouple measurements. Consequently, two scenarios were investigated. The results of these investigations follows here.

The first scenario gave the pusher furnace a setpoint at 1130 °C. Three samples, two Cu sinter-infiltrated ferroalloy and one sintered NC100.24 compact were used during this experiment. The samples were positioned on top of HeBoCoat® 10WF graphite plates. The graphite plate was positioned on top of a mild steel furnace boat. The boat rests on top of the furnace track, also made from mild steel.

This configuration can be seen in Figure 4.7, where the image used was captured using a Canon EOS 750D camera with the settings 1/25 sec. f/14 172 mm and ISO = 200. Two thermocouples were used in the experiment. One was inserted at the lowest point inside the furnace tube (not seen in Figure 4.7) and used as the setpoint temperature, while the second thermocouple was moved between several positions of interest.

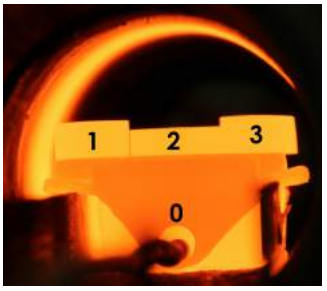

Figure 4.7: Temperature measurement locations (captured using a Canon EOS 750D)

With the setpoint thermocouple measuring 1130 °C in the high heat zone of the furnace tube, a second thermocouple was inserted to measure the local temperatures at the centre of the furnace boat, inside the guide tube. This is where it would normally be

located during a sample run of the furnace. Figure 4.7 depicts four locations where temperature measurements were made. With the setpoint thermocouple at 1130 °C, the measured temperature stabilised at 1082 °C for location 0. Locations 1, 2 and 3 measured 1079, 1074, 1081 °C respectively, which are all lower than the melting temperature of copper (1084 °C, Table C.1 [30–34]). These temperatures are within 4.25 – 4.96 % of the required sinter-infiltration temperature. The maximum difference from the set temperature is 55 ±1 °C, taking into account the 5 ±1 °C offset between thermocouples.

Thermal images of the furnace tube cross-section were taken using a Fluke Thermography Ti400 Thermal Imager. Post processing was performed using Fluke SmartView 3.5.31.0. The emissivity, '$\mathcal{E}$', was adjusted such that at the location of the measurement thermocouple, the temperature of the thermal image and the thermocouple are in agreement. The emissivity values, presented in Table 4.2, are in line with the expected emissivity of steels at high temperature.

Table 4.2: Scenario 1: Temperatures and emissivity with the setpoint thermocouple held at 1130 °C

	Sample 1 ferroalloy $\mathcal{E}$ (Temp.)	**Sample 2 ferroalloy $\mathcal{E}$ (Temp.)**	**Sample 3 NC100.24 $\mathcal{E}$ (Temp.)**
Test 1	91 (1084.9 °C)	91 (1081.0 °C)	90 (1083.6 °C)
Test 2	91 (1086.1 °C)	91 (1079.2 °C)	91 (1086.5 °C)
Test 3	91 (1084.4 °C)	91 (1079.7 °C)	91 (1085.3 °C)
Average	91 (1085.1 °C)	91 (1080.0 °C)	91 (1085.1 °C)

The second scenario involved adjusting the setpoint such that the sample thermocouple (Location 0) remained at 1130 °C. An identical configuration of samples, track, thermocouples and furnace boat were used as in scenario 1. The only parameter that was in this scenario was the furnace set temperature. The set temperature was set to 1174 °C and allowed to stabilise. This set temperature resulted in the sample thermocouple, inserted at position 0, to measure 1130 °C. Locations 1, 2 and 3 measured 1125, 1121, 1125 °C respectively. These temperatures are within 0.44 – 0.8 % of the required sinter-infiltration temperature.

Once again the thermal imaging data was aligned with the thermocouple measurements, resulting in Table 4.3.

Table 4.3: Scenario 1: Temperatures and emissivity with 'Location 0' held at 1130 °C

	Sample 1 ferroalloy $\mathcal{E}$ (Temp.)	**Sample 2 ferroalloy $\mathcal{E}$ (Temp.)**	**Sample 3 NC100.24 $\mathcal{E}$ (Temp.)**
Test 1	91 (1127.3 °C)	89 (1118.1 °C)	90 (1123.8 °C)
Test 2	92 (1128.9 °C)	90 (1125.9 °C)	92 (1124.9 °C)
Test 3	93 (1123.4 °C)	91 (1125.8 °C)	92 (1127.8 °C)
Average	92 (1126.5 °C)	90 (1123.3 °C)	91 (1125.5 °C)

Due to the temperature sensitivity of PM processes, the temperature differences seen in the pusher furnace over the length of a furnace boat (317 °C) or 25 mm sample (82.5 °C) is too large to allow processing of multiple samples simultaneously. Care must be taken to ensure correct sinter-infiltration temperatures are produced at the sample locations by adjusting the furnace set temperature in order to expose the research samples to the correct high heat temperature. Furthermore, it can be noted that introduction of the furnace track has a profound effect on the cross-sectional temperature profile within the furnace tube.

4.4.3 Volume Flow Meter Calibration

Gas flow rates for N_2 and H_2 were measured at various line pressures (30, 40, 50 and 60 kPa) and VAF meter scale markings. It was found that a line pressure, taken at the pressure gauge nearest to the cylinder, of 50 kPa resulted in a good range of flow with sufficient control over the volume flow rate. The pressure drop seen between the pressure gauge nearest to the cylinder and the pressure gauge nearest to the VAF was 1.5 – 8 kPa for the H_2 line over the range of 0 – 6 SLPM and 1.5 – 5.5 kPa for the N_2 line over the range of 0 – 6 SLPM. The regulator ensures that the cylinder side pressure gauge remains constant, but an upstream pressure drop is seen with increasing volume flow rate, thus to avoid constant adjustment of the cylinder regulator calibration was performed at 50 kPa line pressure, measured at the cylinder side pressure gauge. Therefore, the new calibrations take into account the pressure drop between the gas cylinders and the VAF meters.

Instrumentation error was calculated using the Root Sum Square (RSS) method which allows for the propagation of error through different measurements [73]. The calculations for the RSS method can be found in Appendix B.3.1. These errors were deemed to be too large and not representative of the actual system. Thus, other methods were explored in order to quantify the measurement accuracy.

Multiple linear regression was employed with the curve fitting method of

least squares. The least squares method's goal is to minimize the sum of squares between the data and the approximating function. At first, a sample size of 7 was used, but it was found that such a small sample space resulted in a very large confidence band. A straight line approximation was acceptable for the N_2 flow, but not for the H_2 flow. In the pursuit of accuracy, non-linear regression was used for both calibrations. A few different functions were considered; power, exponential and polynomial functions. A third order polynomial resulted in the best fit for both the N_2 and H_2 data. The calculations for the least squares non-linear regression method can be seen in Appendix B.3.2. The resulting confidence curves are plotted in Figure 4.8, where the solid lines indicate the mean value, the dashed lines indicate the confidence limits, the dots indicate data points and the dotted lines indicate old calibration curves. All the curves presented here are given in NLPM[8], thus providing a standardised calibration curve.

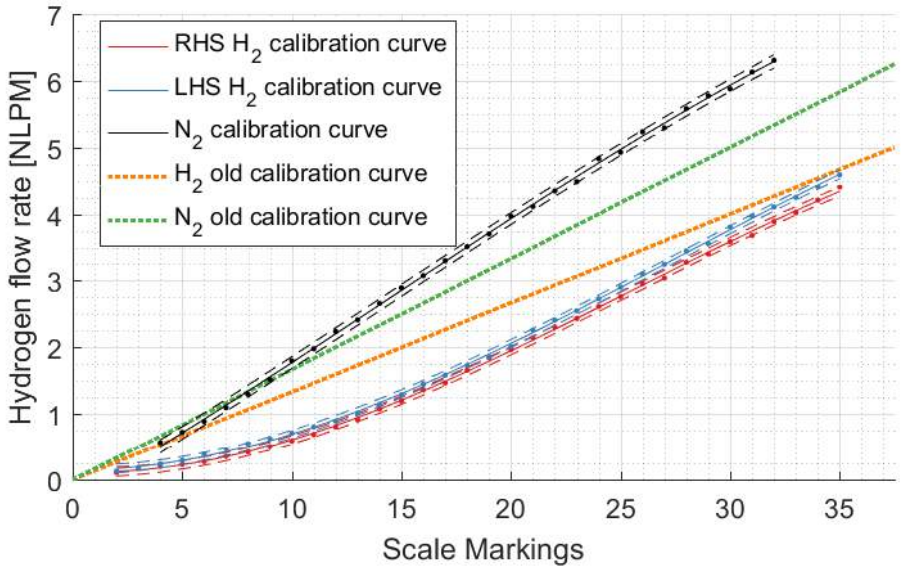

Figure 4.8: VAF volume flow rate calibration curves (95 % confidence, $r^2 \approx 1$)

Due to the large openings available for process gas to escape the furnace tube, at the entrance and exit gates, and outside air to infiltrate the furnace tube the furnace is operated with a total gas flow rate of 6 l/min. During the calibration testing, it was found that 6 l/min, of mixed 80:20 (N_2:H_2), is the maximum flow rate that can be safely supplied to the furnace. Higher flow rates resulted in process gas blowouts at the furnace tube entrance and exit gates due to the quantity of H_2 being burnt off by the pilot flames. The inside diameter of the furnace tube is 0.075 m and it has a length of 1.8 m. Therefore the furnace tube

[8]Normal litres per minute (NLPM) is defined as the flow rate of a gas stream measured at a specific temperature and pressure which has been converted to the flow rate of the gas stream if the temperature and pressure were to be changed to standard conditions of 1 atm pressure and a temperature of 0 °C

has a volume of 7.95 litres. For the pusher furnace with a flow rate of 6 l/min the furnace tube atmosphere turnover rate is calculated, in Appendix B.3.4, to be 45.27 times per hour. This turnover rate is ~4.5 times higher than the required minimum turnover rate of 10 times per hour, as discussed in Section 2.3.1. The use of a maximum flow rate will be beneficial to the removal of lubricants during delubrication, as explained in Section 2.3.

In order to ensure that a sufficient forward flow of process gas is achieved in the delube section, a specific configuration of fully open and fully closed valves is required; see Figure B.1 for the positions of valves. A total gas volume flow rate of 6 l/min was used. The precise configuration is given in Appendix B.3.3. This state is considered to be steady for the remainder of the calculations. It has been assumed that the difference in resistance to flow between the paths of a T-junction are negligible and therefore flow separates equally between the two paths. This is assumed because the lengths of pipe are short, there are few minor losses and it has been assumed that the gas system exhausts inside the furnace tube to the same, atmospheric, pressure. If the losses are different in reality, control of the valves can rectify the discrepancy. It has been assumed that all gases ($H_2O_{(g)}$, N_2, H_2) are pure and obey the ideal gas law at the temperatures and pressures considered. It is assumed that both the process gas and the distilled water in the bubbler are at a room temperature of 20 °C which remains constant. This is assumed as the gas supply pipes are outside the furnace, held at room temperature. Furthermore, it has been assumed that process gasses are supplied to the gas system with low dewpoints.

Consider a N_2 flow rate of 5.33 l/min which enters the gas system through the N_2 rotameter which controls its volume flow rate. The N_2 flow reaches the first T-junction where the flow equally separates (because the losses are assumed to be equal in both paths) to the cooling zone and the preheat zone. Thus, 2.67 l/min N_2 enters the cooling zone and 2.67 l/min continues on to the preheat zone.

Before reaching the preheat zone H_2 and $H_2O_{(g)}$ must be introduced. Thus, the N_2 flow reaches a T-junction where 0.67 l/min H_2 is added to the flow of 2.67 l/min N_2. 3.33 l/min of process gas now proceeds to the bubbler, where $H_2O_{(g)}$ will be added before the process gas enters the preheat zone. The N_2/H_2 mixture at the preheat zone can now be calculated: $0.67/3.33 \simeq 80/20$ by volume.

Chapter 5

Delubrication Study

In order to establish sintering best practices for the pusher furnace at SU, this study investigated the thermal decomposition of the lubricants ethylene bisstearamide (EBS) and zinc stearate (given in Appendix D.2) at various temperatures in air (oxidising), nitrogen (inert) and 80:20 N_2:H_2 (reducing) atmospheres. Additionally the oxidation behaviour of the ferroalloy and Cu were investigated. A thermoanalytic device was utilised in order to obtain an understanding of the thermal behaviour of the lubricant used and the oxidation behaviour of the ferroalloy and Cu. Of particular interest are the melting temperature, the characteristic temperature, where the rate of lubricant decomposition is a maximum, and the influence of temperature and time on the pyrolysis of the lubricants. Thereafter, an investigation of delubrication behaviour is conducted where, with knowledge gained from the thermoanalytics investigations, an estimated optimal temperature for delubrication is tested.

Differential Scanning Calorimetry (DSC) is an analysis technique employed to investigate the heat capacity[1] of a material as the temperature it is exposed to is changed. An interested reader can consult Appendix D.1 for further information regarding the interpretation of DSC results. The technique uses two furnaces, both are kept at the same temperature. One of the furnaces contains a sample of interest and the second contains a reference sample. For the purpose of determining the heat capacity, a reference sample with a well-known heat capacity is required. However, a well-known reference is not required to gain knowledge of other thermal properties of a material, such as phase transformations and chemical reactions.

[1]Heat capacity is the heat required to raise the temperature of a unit mass of the material by 1 °C.

5.1 Thermal Behaviour of the ferroalloy, Cu and EBS

In this investigation, the decomposition behaviour of the lubricant used in the ferroalloy (Acrawax®), Cu (unknown) and Licowax[2] and the chemical reactions occurring during delubrication are of interest.

5.1.1 Experiment Procedure

Research Question: At what temperature does lubricant melting, decomposition and evaporation occur, and what influence does an oxidising atmosphere have on this behaviour? In order to achieve this goal, the specimens will be heated at a constant heating rate to a temperature of 700 °C whilst measuring the differential heat flow required to do so.

Two sets of three specimens, with an average mass of ~50 mg, were taken from a proprietary ferroalloy sample and a Cu infiltrate disc sample. The sample details for the ferroalloy and Cu are given in Section 3. Additionally, two sets of three Licowax specimens, with an average mass of ~5 mg were considered. The specimens were placed inside of a DSC furnace, in alumina pans. The experiment was conducted using a Perkin Elmer DSC 8000 thermoanalytic device. The DSC has an accuracy of ±0.05 °C and a precision of ±0.008 °C.

An empty alumina pan was first weighed whereafter a specimen was positioned in the alumina pan and weighed. A calibration run using an empty alumina pan was conducted before each test. Mass measurements were performed using a KERN ABT 120-5DM precision scale with a reproducibility of 0.02 mg and linearity of ±0.05 mg. The calculated difference in mass between the empty pan and specimen filled pan results in the specimen mass.

The specimen was then positioned inside the DSC furnace with a compressed air or N_2[3] flow rate of 40 ml/min. A temperature scan was performed, from 50 to 700 °C at 7 and 50 °C/min, respectively. Each specimen was subsequently weighed after processing in order to determine the mass of the specimen remaining after the DSC delubrication. Oxidation of the ferroalloy and Cu specimens was expected to occur, during the tests conducted in air, and must be taken into account during interpretation of the results.

The faster heating rate allows peaks in the data to be more easily seen, but at the cost of reduced temperature accuracy due to heating lag. The lower heating rate allows for more accurate specimen temperatures but at the cost of increased oxidation and smaller thermal event peaks.

[2]Licowax is a tradename, similar to Acrawax®, for an EBS lubricant.

[3]Compressed air and pure N_2 was used because the use of a N_2:H_2 atmosphere in the DSC was not viable at the time of this investigation.

The expected oxidation reactions of Cu and Fe are given in Reactions 8 and 9 where the variables a, b, c and d indicate integer mole quantities.

$$aCu(s) + bO_2(g) \longrightarrow cCuO(s) + dCu_2O(s) \quad \{8\}$$

$$aFe(s) + bO_2(g) \longrightarrow cFeO(s) + dFe_2O_3(s) \quad \{9\}$$

For an exothermic reaction, heat is released by the system, thus the net change in enthalpy is $\Delta H_{sys} < 0$. This release of energy increases the entropy of the surroundings and therefore $\Delta S_{surr} > 0$. For an endothermic reaction, heat is absorbed by the reaction, thus $\Delta H_{sys} > 0$. This energy is lost by the surroundings and therefore $\Delta S_{surr} < 0$ [50].

In order to calculate ΔH_{sys} and ΔS_{surr} the enthalpy[4] and standard molar entropy (S°) of the constituents must be known. These quantities are available at various temperatures in the NIST-JANAF thermodynamic tables [74]. The equations of interest for determining whether the reactions are exo- or endothermic are given in Equations 5.1 – 5.4 [50].

$$\Delta S^\circ_{sys} = \sum n_{products} S^\circ_{products} \sum n_{reactants} S^\circ_{reactants} \quad (5.1)$$

$$\Delta H^\circ_{f,sys} = \sum n_{products} H^\circ_{f,products} \sum n_{reactants} H^\circ_{f,reactants} \quad (5.2)$$

$$\Delta S^\circ_{surr} = -\frac{\Delta H_{sys}}{T} \quad (5.3)$$

$$\Delta S^\circ_{univ} = \Delta S^\circ_{sys} - \Delta S^\circ_{surr} \quad (5.4)$$

From Equations 5.1 – 5.4 it was determined that for oxidation of Fe and Cu (at all delubing temperatures):

$$\Delta S_{sys} < 0 \quad \& \quad \Delta H_{sys} << 0$$

$$\Delta S_{surr} > 0 \quad \& \quad \Delta S_{univ} > 0$$

Therefore, oxidation of both Fe and Cu are both exothermic over the temperature range of interest.

5.1.2 Results

Mean differential heat flow (averaged across the three samples in a single set) for the DSC delubrication of the ferroalloy and Cu specimens can be seen

[4]Enthalpy is the total heat content of a system.

in Figure 5.1, and similarly for the Licowax® specimens in Figure 5.2. The resulting change in total mass, over the entire experiment, for the ferroalloy and Cu specimens can be seen in Figure 5.3. Mass change data for Licowax can be seen in Figure 5.4. Both the ferroalloy and the Cu samples processed in air were visibly oxidised, evident by the matt grey color of their surfaces. Interpretation and discussion of the results are given thereafter.

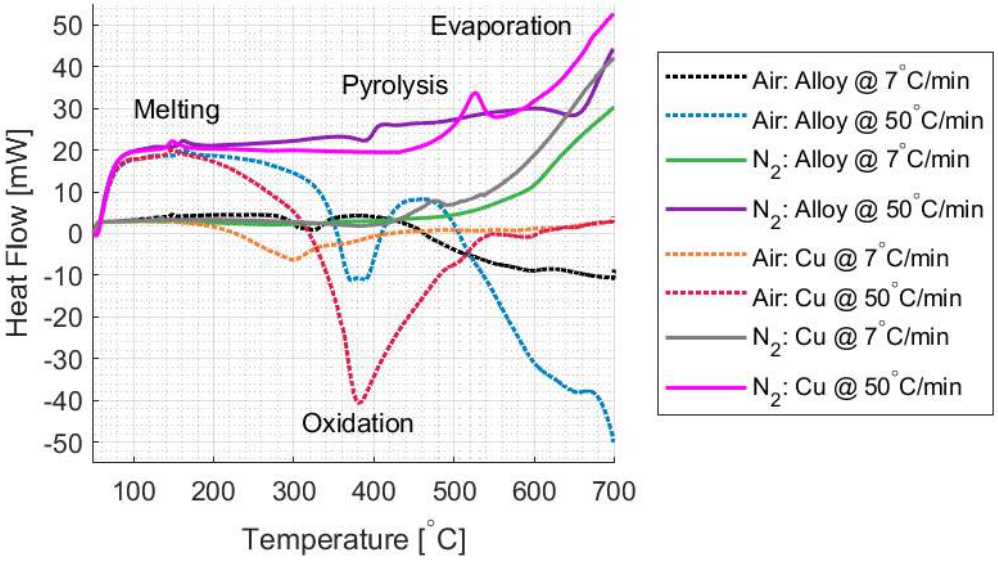

Figure 5.1: Thermoanalytic results for the ferroalloy and Cu specimens processed in air and N_2 atmospheres at both 7 & 50 °C/min between 50 – 700 °C

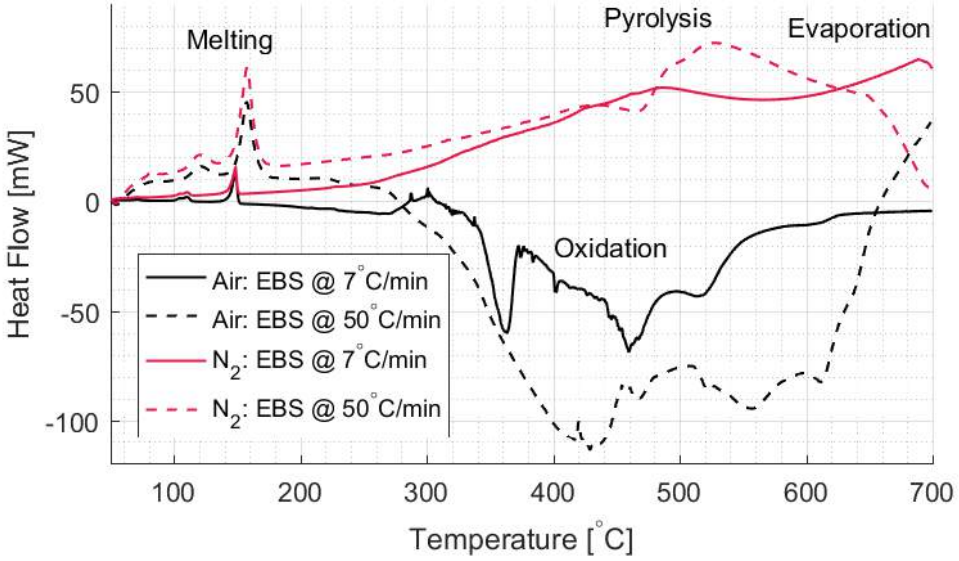

Figure 5.2: Thermoanalytic results for Licowax® specimens processed in air and N_2 atmospheres at both 7 & 50 °C/min between 50 – 700 °C

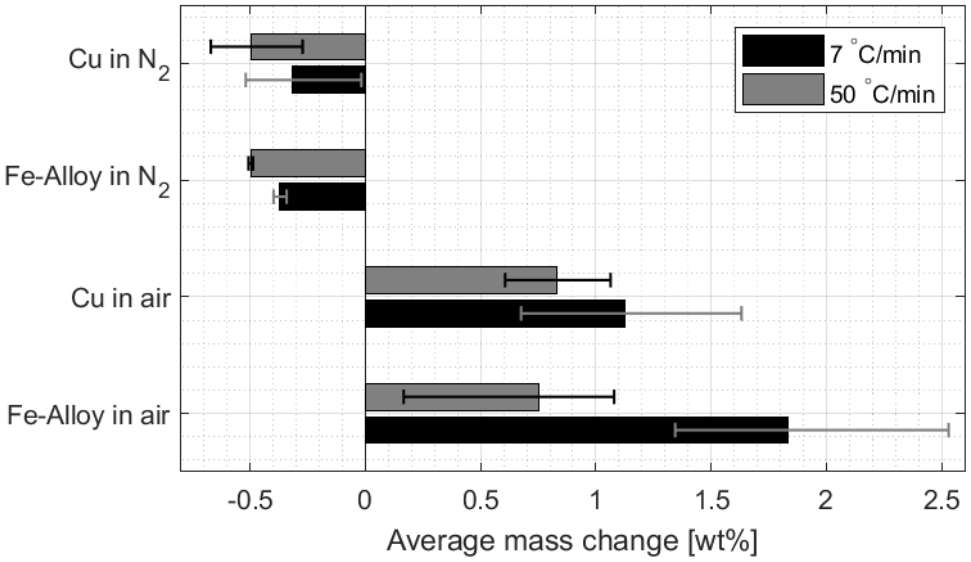

Figure 5.3: Change in total mass of the ferroalloy & Cu specimens over the duration of the experiment, where the specimens were processed in air & N_2 at a heating rate of 7 and 50 °C/min between 50 – 700 °C

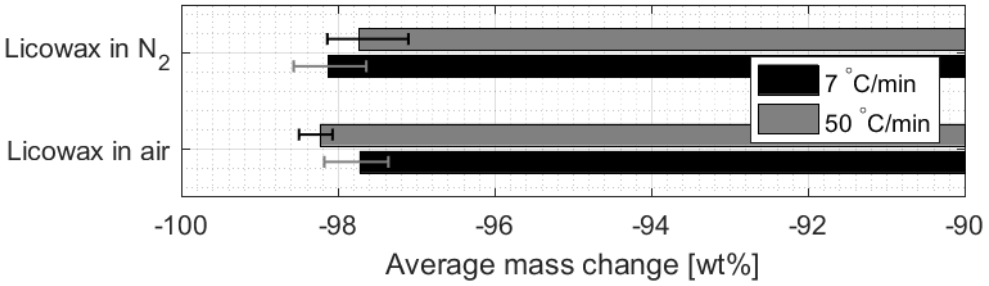

Figure 5.4: Change in total mass of Licowax® specimens over the duration of the experiment, where the specimens were processed in air & N_2 at a heating rate of 7 and 50 °C/min between 50 – 700 °C

5.1.3 Discussion

Observing the results from the thermoanalytic tests, given in Figures 5.1 – 5.4, and considering the sequence of delubrication events detailed in Section 2.3.1 the following interpretations can be made.

The first part of all the differential heat flow curves (up to ~180°C) in all figures is endothermic (positive). This is as expected because the specimens have a thermal mass which absorbs some heat energy. Additionally, for the ferroalloy and Cu specimens processed in air, the exothermic oxidation rate is not yet significant. Therefore, these specimens require a net positive differential heat flow to increase their temperatures.

Endothermic peaks are evident in all datasets at 130 – 150 °C for the 7°C/min heating rate. This indicates that additional energy was needed to increase the temperature, such as is necessary in the event of a phase transformation. These peaks correspond to a melting point of 140 – 145 °C for Acrawax® [25]. These results are in good agreement with Licowax which has a reported melting temperature of 139 – 144°C and a measured melting temperature of ~145 °C in this investigation.

In the 50 °C/min data, for ferroalloy and Cu in air, local minima are seen at ~375 °C. In the more temperature accurate data of the 7 °C/min data these local minima occur at 300 – 325 °C for the ferroalloy and Cu in air data sets. These local minima correspond to the decomposition and subsequent exothermic oxidation of the lubricant and specimens. From literature, presented in Section 2.3.1, evaporation of the pyrolysis products is expected between 300 – 650 °C which is in agreement with the aforementioned result [5]. Clear peaks in this region are only found in the Cu data, at 470 °C and 530 °C for 7 and 50 °C/min data, respectively. Evaporation is an endothermic process, similar to pyrolysis, which will counter the energy release from decomposition in the specimens processed in N_2, possibly explaining the lack of peaks in this temperature range.

It can be seen that the Cu specimens processed in air have a positive sloping heat flow curve after the negative pyrolysis peak. This is due to the formation of Cu_2O in the Cu specimens, as the temperature increases, it can be noted that $\Delta H_{sys,Cu2O}$ decreases in magnitude, i.e. less energy is released. This results in the slope of the heat flow curves for the Cu samples to be positive once the lubricant has decomposed and burnt-off. Similarly, for the ferroalloy the specimens' slope becomes negative after the lubricant decomposition and burn-off, due to $\Delta H_{sys,Fe}$, which remains approximately constant, thus the thermal behaviour remains dominated by oxidation (as opposed to being dominated by evaporation). Furthermore, the higher temperature provides more particle collisions with the required activation energy, thus resulting in an increased oxidation rate as the temperature is increased, compounding the rate of energy released during Fe oxidation.

The mass of the ferroalloy and Cu specimens, processed in air, increased (even though there was solid lubricant burn-off/decomposition). The increased mass can be explained by oxidation. As for the specimens processed in N_2, a mass loss of ~0.5 wt% was seen. This is higher than the estimated lubricant content of 0.2 wt% for the ferroalloy.

The characteristic temperature, where the rate of pyrolysis is a maximum, for EBS in N_2 is expected, according to literature, at $T_c = 437$ °C [46]. The characteristic temperature (T_c) of the present study, for EBS heated in N_2, is located at ≈ 470 °C. This deviation is probably due to the temperature lag

resulting from the use of alumina specimen pans, which are known to have a relatively low thermal conductivity.

The heat flow data for Licowax in the region of 300 – 500 °C is unreliable due to boiling of the lubricant inside the furnace at these temperatures, causing the lubricant to impede gas flow through the specimen pan and coming into contact with the furnace interior, resulting in considerable noise in the data. However, it can be mentioned that there is an endothermic trend for the Licowax specimens processed in N_2, while there is an exothermic trend for the Licowax specimens processed in air.

The Licowax specimens systematically lost ~98 wt% in both N_2 and air atmospheres and for both heating rates used.

5.2 Discrete Furnace Delubrication with Constant Atmosphere

This section presents the experimental procedure followed, and the results of the furnace delubrication investigation. The interest of this investigation is what the effects of various hold times, at a delubrication temperature of 700 °C, are on the degree of delubrication of samples within the furnace atmosphere (N_2:H_2, 80:20).

5.2.1 Experimental Procedure

Research question: Does the hold time at a delubrication temperature of 700 °C influence the degree of delubrication? Hypothesis: Yes, increased hold time at delubrication temperature improves the degree of delubrication.

General purpose iron powder (NC100.24 supplied by Höganäs) was mixed with 0.2 wt% and 2.0 wt% zinc stearate as lubricant, for 20 min at 200 rpm, in a custom built turbula-style swing mixer with a SEW Eurodrive R17 DR63L4 motor and a Movitrac B controller. Cylindrical samples with a diameter of 25.4 mm and mass 25 g were compacted, using tooling according to the ASTM B925 standard, using this powder blend to a pressure of 400 MPa. A total of 24 samples were pressed to a green density of 6.7 g/cc. Compaction was performed using an AMSLER SZBD 56 hydraulic press, HBM C4 500 kN load cell, HBM Spider 8 data logger and Catman Easy data acquisition software. The green samples were subsequently weighed and dimensional measurements were taken before finally capturing images of the samples for observational purposes. Mass measurements were performed using a KERN ABT 120-5DM precision scale with a reproducibility of 0.02 mg and linearity of ±0.05 mg.

The continuous pusher furnace was purged with N_2 at 5.33 l/min for 30 min

and heated to 1130 °C. The furnace gate burner flames were ignited and H_2 flow of 0.67 l/min was added to the furnace atmosphere. The green samples were placed on a hexagonal boron nitrate (HeBo) coated graphite plates and pushed into the furnace where they were heated in the preheat zone to 700 °C, at 10 °C/min, under a mixed N_2:H_2 (80:20) atmosphere. When the samples reached 700 °C they remained at this temperature for the various hold times of 5, 10, 20 and 30 min, before moving them to the cooling zone where they were furnace cooled. The samples were removed from the furnace and images were once again captured for observational comparison purposes. In order to determine the change in mass of the samples, they were weighed again (with residue intact) and their dimensions were taken.

5.2.2 Results

Figure 5.5 presents samples images of each of the hold times tested for both the 2 wt% and the 0.2 wt% sample sets.

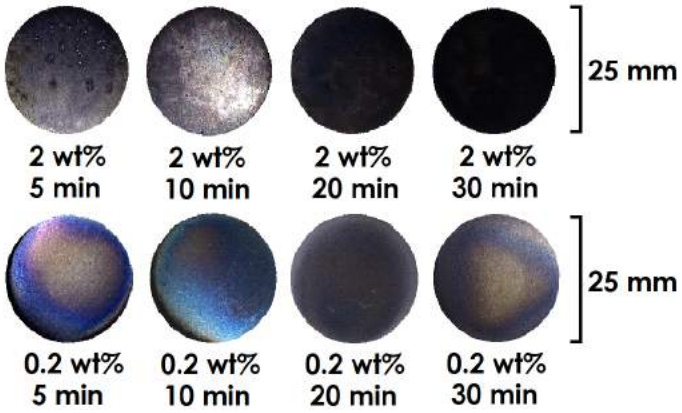

Figure 5.5: Sample images of sintered ferrous PM samples, processed at a delubrication temperature of 700 °C with a heating rate of 10 °C/min, with 2 wt% zinc stearate as lubricant in an 80:20 N_2:H_2 atmosphere for varying hold times

Figure 5.6 shows the mass loss after delubrication in the pusher furnace for different hold times.

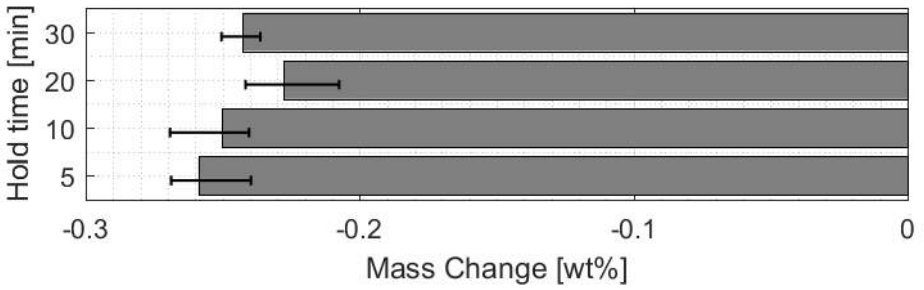

(a) Sintered ferrous PM samples with 0.2 wt% zinc stearate as lubricant

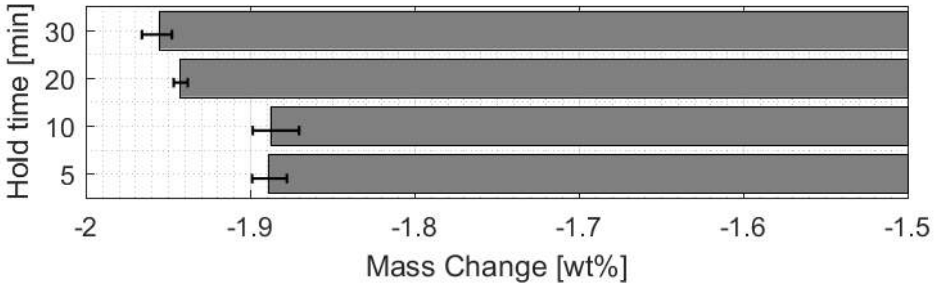

(b) Sintered ferrous PM samples with 2 wt% zinc stearate as lubricant

Figure 5.6: Total percentage mass change of sintered ferrous PM samples, processed at a delubrication temperature of 700 °C with a heating rate of 10 °C/min, with 2 wt% zinc stearate as lubricant in an 80:20 N_2:H_2 atmosphere for varying hold times

5.2.3 Discussion

It can be seen that for the 0.2 wt% zinc stearate iron powder mixtures, samples systematically lose more mass than that of the zinc stearate alone. Consideration of the accuracy of the mass measurement scale used for this investigation can explain the discrepancy in the data. It can be seen that for the 2 wt% zinc stearate iron powder mixtures, that the samples lost less mass than expected for full delubrication. A black residue was observed on the surface of the 2 wt% zinc stearate samples, and to a lesser extent on the 0.2 wt% samples. For the 2 wt% samples the amount of black residue visibly increased with an increase in hold time. This residue increase was accompanied by a larger loss of mass. Additionally, for the most of the 0.2 wt% samples a blue surface tint is seen. This colouration is caused by the formation of a thin oxide layer on the surface of the samples. An indigo/blue colour is seen due to elimination of the longer wavelengths of light by the oxide layer through destructive interference caused by the thickness[5].

[5]Destructive interference is caused by shifting a wavelength of light by 0.5λ. Thus, to shift reflected light the thickness of the oxide layer must be 0.25λ. Therefore, red light with a wavelength of 750 nm is eliminated by an oxide layer with a thickness of ~188 nm.

Chapter 6

Sinter-infiltration Study

This study investigates whether the pusher furnace can produce consistent reliable sinter-infiltration conditions. Of particular interest is the quality of samples that the furnace can produce, ideally, high-quality samples are; fully sinter-infiltrated, soot (from incomplete delubrication) and oxidation free. Due to the profile of the steady state temperature curve, the pusher furnace cannot be operated as a continuous furnace for samples requiring an isothermal hold at a specific temperature. Therefore, in order to facilitate samples that require isothermal holds the furnace operator must move samples, incrementally, at a constant (average) heating rate until the isothermal hold temperature is reached whereafter the sample is left stationary for the duration of the isothermal hold. As the sample is moved through the furnace there are two options for atmosphere control;

Semi-continuous operation: During semi-continuous operation, the three furnace atmosphere zones are generated using the two[1] of the three available process gas inlets of the furnace tube. These atmosphere zones remain unaltered for the duration of the sintering cycle.

Discrete operation: During discrete operation, the entire furnace atmosphere is tailored according to the temperature at which the sample is currently located. The atmosphere is created using only one inlet, the inlet located between the high heat zone and the cooling section. The composition of the process gas through this single inlet is tailored for the temperature at which the sample is located. The sinter-infiltration study was performed in two separate investigations, investigating whether it is possible to successfully produce sinter-infiltrated samples in the pusher furnace using two atmosphere control options. The first investigation, the topic of Section 6.1, investigates sintering results using discrete furnace operation. The second investigation, the topic of Section 6.2, investigates sintering results using discrete furnace

[1]The inlet at the furnace tube exit is not used because the inlet at the muffle exit is located too close to the tube exit, exhausting nearly directly to the furnace room atmosphere. Additionally, the gas flow from the inlet between the high heat zone and the cooling zone is sufficient to supply an adequate gas flow rate to the cooling zone.

operation.

6.1 Discrete Furnace with Constant Atmosphere Composition

Research Question: Can the pusher furnace, with the addition of a moisture bubbler, produce consistent reliable sinter-infiltration conditions?

6.1.1 Experiment Procedure

The planned experiment involves eight (8) sets of three (3) research size samples of ferrous PM and copper infiltrate. The total amount of samples required for this experiment is therefore 24 ferroualloy PM samples and 24 copper infiltrate discs.

The sample sets will move through the furnace at a constant heating rate, placed on top of hexagonal boron nitride (HeBo) coated graphite plate. Once a set of samples reaches a pre-determined point of interest (a set temperature) the sample set will be pushed to the cooling zone where it will be allowed to cool, whereafter the sample set will be removed from the furnace. The temperatures of interest are; 1070, 1090, 1110, 1130 °C. At the sintering temperature of 1130 °C several hold times will be investigated; 0, 5, 10, 20, 30 min. The position of these temperatures inside the pusher furnace can be seen in Figure 6.1 where they are indicated by dotted vertical lines.

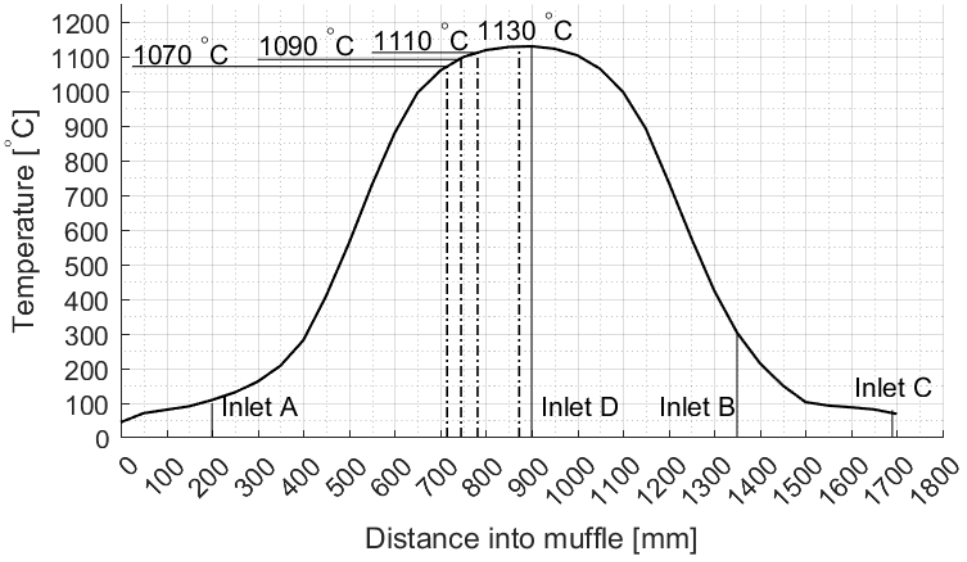

Figure 6.1: Pusher furnace axial temperature profile and experiment temperature locations

The atmosphere settings for all of the sample runs is constant. A process gas composition of N_2:H_2/80:20 (vol%) at the preheat/delubrication zone is desired. According to calculations performed, in Appendix B.3.3, on the process gas system (when operated with two process gas inlets; A and B) 5.33 l/min N_2 and 0.67 l/min H_2 is required for a total process gas flow rate of 6 l/min.

As the total gas flow splits between the preheat and the cooling zones, the expected flow rates (according to calculations performed in Appendix B.3.3) are 2.67 l/min N_2 and 0.67 l/min H_2 at the preheat zone with the remainder of the flow entering the cooling zone. The locations of the process gas inlets, at locations A, B, C and D can be seen relative to the length of the furnace tube in Figure 6.1. Note that inlet 'D' is technically not an inlet to the furnace tube, but rather to the muffle. However, the presence of cracks in the furnace tube allows movement of gasses between the muffle and the furnace tube.

For this experiment only inlets 'A' and 'B' were used, a valve was installed to prevent process gas flow to the muffle which would otherwise exhaust at the so-called inlet 'D' through cracks in the furnace tube. The moisture bubbler was connected to inlet 'A' and gas mixing occurred before the process gasses reached the moisture bubbler. The moisture bubbler received the preheat zone process gas mixture which according to calculations, seen in Appendix B.1.2, adds 42.56 mg/min of $H_2O_{(g)}$ to the preheat zone process gas resulting in a dewpoint of ~8 °C.

After the processing of samples were complete and the samples have been removed from the furnace cooling zone, pictures of the samples were taken and mass measurements were performed on each sample. The sample residue or uninfiltrated copper was subsequently cleaned, by removing the excess copper and residue. After cleaning the samples were weighed again in order to determine the mass of residue/uninfiltrated copper. Dimensional measurements, thickness and diameter, were taken of the cleaned samples. From these mass and dimensional measurements, the sintered density was calculated.

6.1.2 Results

Sample images of the sinter-infiltration result for the experiment can be seen in Figure 6.2. A large degree of sooting and oxidation is visible in the figure (evident through the grey surface color of the samples. Copper balling/pooling can be seen, where the copper balls/pools are covered in black residue.

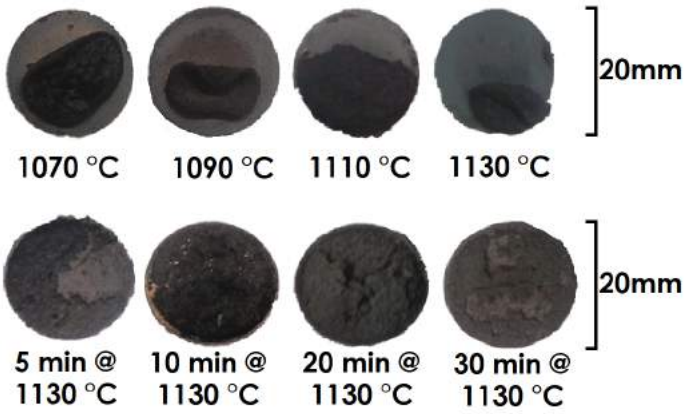

Figure 6.2: Sample images of sinter-infilration result using a continuous atmosphere

The experiment results are plotted in Figure 6.3, where the sample IDs are plotted on the x-axis, the sample sintered density is plotted on the left-hand side y-axis, and the residue mass removed from the sample is plotted on the right-hand side y-axis. The sintered density data point markers are crosses while the residue mass data point markers are circles.

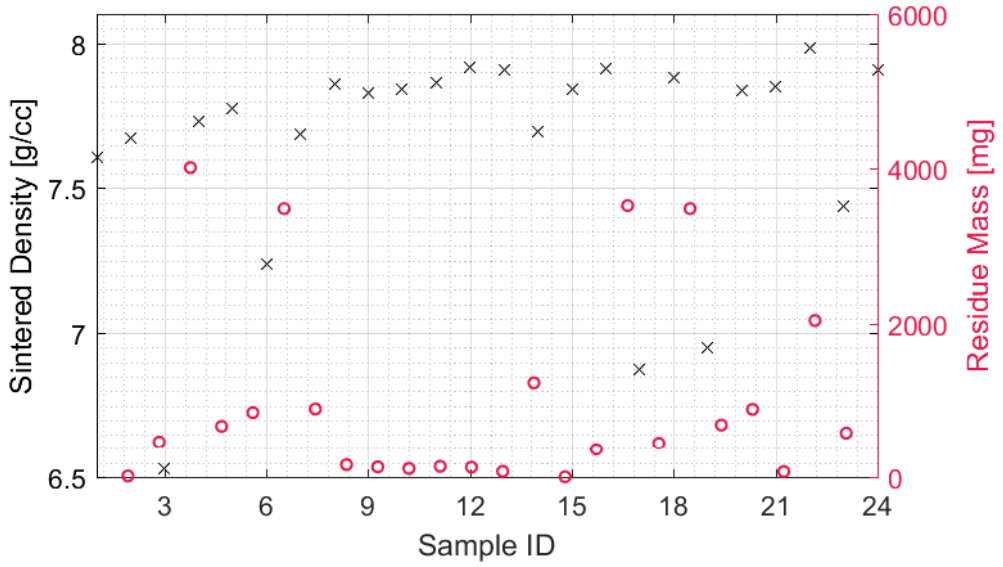

Figure 6.3: Sintered densities & residue mass data for
Sample ID: 1–3 (1070 °C), 4–6 (1090 °C), 7–9 (1110 °C), 10–12 (1130 °C), 13–15 (1130 °C: 5 min hold), 16–18 (1130 °C: 10 min hold), 19–21 (1130 °C: 20 min hold), 22–24 (1130 °C: 30 min hold)

A general trend can be seen (when ignoring the presence of outliers), where the sintered density decreases, as the sintering temperature (and time) is decreased. This is as expected, as sintering involves densification. It can be noted that

there is no clear trend in the amount of residue present in any sample set, in fact, the amount of residue mass present even differs considerably between samples from the same sample set. The reason for outliers in both the density and residue data is that sooting for those samples were particularly heavy, resulting in large amounts of uninfiltrated copper.

6.1.3 Conclusions

The pusher furnace cannot when operated in a semi-continuous way, produce successfully sinter-infiltrated ferrous-copper composites. The addition of the moisture bubbler did not improve the sinter-infiltration results in any measurable way for a continuously operated sintering atmosphere. Overall very poor sinter-infiltration results were obtained, with nearly all samples being heavily sooted. The large amount of sooting resulted primarily in copper pooling or balling leading to incomplete infiltration.

6.2 Discrete Furnace with Transient Atmosphere Composition

The author has reasoned that although the pusher furnace used in this project is considered a continuous type sintering furnace it cannot be operated as such in order to achieve the goals of this project. The furnace axial temperature profile, presented in Section 4.4.2, forces the furnace operator to move samples at different speeds in different areas of the furnace in order to maintain a constant heating rate. Furthermore, the pusher furnace does not have an automated feed mechanism. As such, the furnace is operated by moving (or pushing) samples by discrete lengths through the furnace, also contributing to discontinuous furnace operation.

It was found during the course of this project that the preheat and cooling zone process gas inlets are located too close to the ends of the furnace tube and are insufficient for creating and maintaining a suitable continuous sintering atmosphere in these regions. A solution to the latter problem was developed where the moisture bubbler is connected to the process gas inlet between the high heat zone and the cooling zone. This inlet alone is used[2] to supply process gas to the furnace.

Resultantly the three distinct furnace zones must be created using only one inlet. The process gas composition through this inlet must, be transient — changing as is required by the temperature to which the current sample set is exposed. This also means that only a single sample, or sample set, can

[2]Small amounts of process gas flow may be required through these inlets to ensure sufficient positive pressure at the furnace tube entrance or exit. This must be controlled following observations by the furnace operator.

be sintered at a time. Due to these adaptations of the furnace operation, it can no longer be defined as a continuous sintering furnace. Rather the furnace operation is now more accurately referred to as discrete furnace operation with transient atmosphere composition.

In summary, the pusher furnace cannot (for the outcomes of this project) be operated in a continuous manner. Instead, it is operated using the discrete movement of samples, to ensure a constant heating rate, and transient atmosphere control, to ensure the correct atmosphere composition and flow throughout the furnace. The validity of this conceptual operation process was tested under the following research question.

Research Question: Can the pusher furnace, configured for discrete furnace operation, with transient atmosphere composition, and the addition of a moisture bubbler, produce consistent reliable sinter-infiltration conditions?

6.2.1 Experiment Procedure

The planned experiment involves four (4) sets of three (3) research size samples of the ferroalloy compacts and Cu infiltrate slugs. The total amount of samples required for this experiment is therefore 12 ferroalloy PM samples and 12 copper slugs.

The bubble column reactor was moved from the preheat zone process gas inlet, where it was used during the previous investigations, to the high heat zone process gas inlet (inlet 'B' in Figure B.1). Mass measurements of all of the samples were performed using a KERN ABT 120-5DM precision scale with a reproducibility of 0.02 mg, linearity of ±0.05 mg. Dimension measurements were made of all the samples using vernier callipers, whereafter the samples were placed on HeBo coated graphite plates. Subsequently, images of the samples were captured using a Canon EOS 750D camera.

The sintering furnace was purged for 30 min with N_2 at 6 l/min. The cooling zone water jacket was employed with tap water at ambient temperature and a volume flow rate of 75 ml/min. The furnace was then heated to a set temperature of 1174 °C, as is required in order to sinter at 1130 °C (see Section 4.4.2). The burner flames at each end of the furnace were ignited and the atmosphere composition adjusted to 80:20 vol% N_2:H_2 with a total volume flow rate of 6 l/min. The entirety of the process gas was bubbled through the bubble column reactor, because results from Section 6.1 indicated incomplete delubrication had occurred with 80 vol% of the inlet process gas bubbled through the reactor.

Samples were pushed in intervals of 5 minutes with an average heating rate of 10 °C/min. When the samples reached a temperature of 700 °C, where

delubrication was found to be optimally complete (see Sections 5 and D.2), the moisture bubbler was bypassed completely. The sample sets were heated further to 1070, 1090, 1110 and 1130 °C respectively with an atmosphere composition of 80:20 vol% N_2:H_2 at 6 l/min. The samples were then pushed to the cooling zone where they were allowed to furnace cool in a 95:5 vol% N_2:H_2 atmosphere. The samples were removed from the furnace, once below a temperature of at least 300 °C, and images were once again captured.

The samples were sectioned through their centres, in the vertical plane, using diamond cutting blades on a Buehler IsoMet precision saw. The samples were then mounted in PolyFast conductive hot mounting compound, using a Buehler SimpliMet 1000, in order for analysis on a scanning electron microscope (SEM). The samples were ground and polished, using a Buehler Alpha grinder-polisher, following standard metallurgical grinding and polishing procedures of progressively finer SiC paper, diamond suspension liquid, and ultrasonic and isopropanol cleaning. The samples were then cut to a thickness of 5 mm for accurate results in the SEM unit[3].

Several SEM techniques were used to collect data from the samples and additionally optical- and stereo microscopy was conducted. Optical- and stereo microscopy was conducted using an Olympus GX51 and an Olympus SZX7 respectively. Each microscope is equipped with a SC30 digital camera and Stream Essentials 1.9.4 software package. SEM analysis was conducted, with the assistance of analyst Elrika Harmzen-Pretorius, on a Zeiss MERLIN SEM unit located at Stellenbosch University's Geology faculty. The results of these tests are presented in the following section with a discussion thereafter.

6.2.2 Results

Figure 6.4 presents the sinter-infiltration progression, of the experiment, as the temperature is increased. The formation of a region of black residue can be seen in the figure, where the surrounding part surfaces are clean of sooting (from incomplete delubrication) and oxidation. The samples are seen from above and as the sintering temperature is increased the Cu infiltrant enters the porous ferroalloy sample, revealing its matt grey surface.

[3]The calibration materials for the SEM unit are 5 mm high and therefore the most accurate results are obtained at this sample height.

Figure 6.4: Post sinter-infilration sample set using transient atmosphere composition

Figure 6.5 presents a back-scatter detector image followed by several elemental composition images obtained from wavelength-dispersive x-ray spectroscopy (WDS) of a sample processed at 1110 °C. The WDS scan was performed, from east to west in the Figure, top to bottom on the vertical plane of the sample, through a central area of the sample. The incomplete infiltrate Cu slug can be seen on the eastern side of the figure and to its west is the infiltrated ferroalloy compact. The SEM unit did not scan in a perfectly straight line and as such the scans are bordered with a black background.

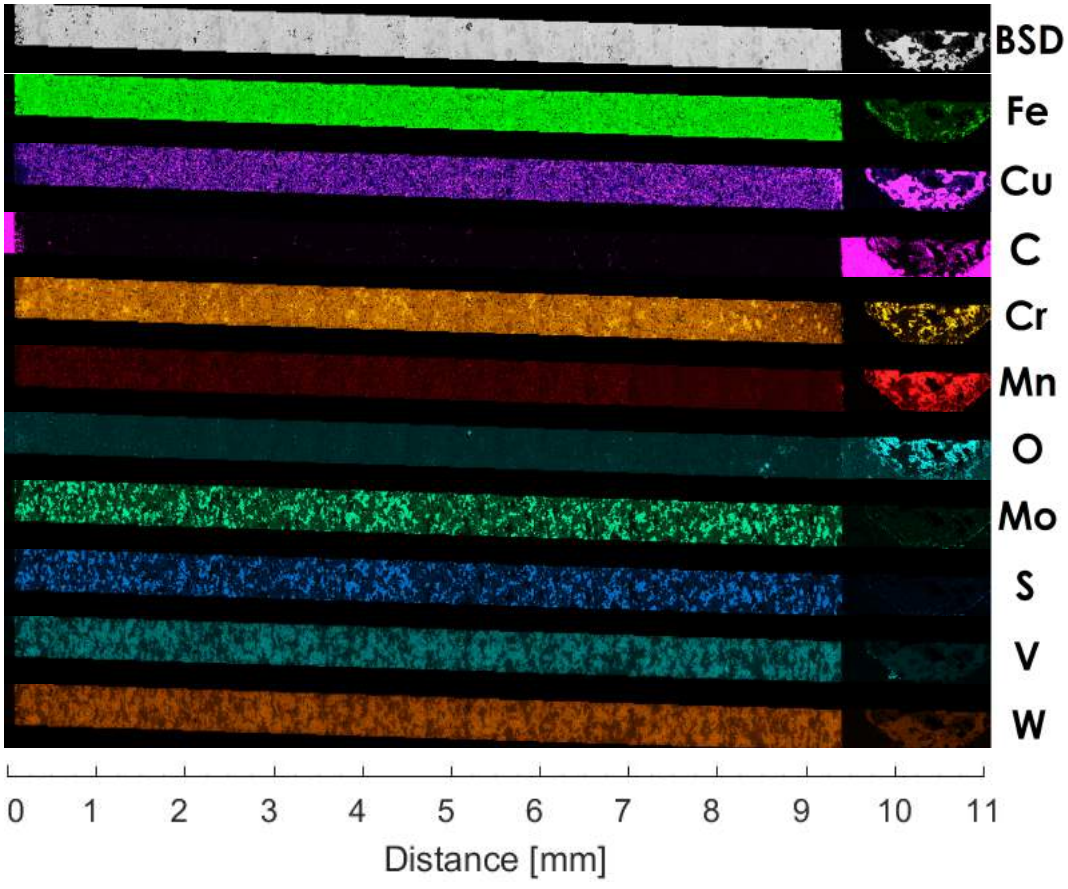

Figure 6.5: WDS elemental compositional images for a sample processed at 1110 °C

Figure 6.6 presents data obtained from WDS scans, similar to Figure 6.5, of samples processed at each of the temperatures tested, as indicated in the legend. The Cu content images were converted to grayscale and an average pixel grayscale value was calculated over every 160-pixel columns. These values were then normalised against the maximum greyscale value and used to represent normalised Cu concentration in the plot. It is assumed that the maxiumum greyscale value corresponds to fully dense Cu. The pixels per unit length, as determined from the scale bars on the images, was used to plot the distance from the bottom of the sample, along its length, on the x-axis. The interface between the Cu and ferroalloy compacts were used to locate each of the plots on the x-axis, in order to more effectively compare the infiltration interface area between the different samples with different overall dimensions. Note that the uninfiltrated Cu regions do not all correspond due to the area in which the scan was completed, the uninfiltrated Cu may be separated from the interface.

Figure 6.7 presents EDS data plots[4] for variable sized area scans performed along the depth of the samples. The data was use to plot Mn content, on the y-axis with a log scale of the wt% detected, along the distance of the samples.

Figure 6.8a presents a optical microscope image of the interface area between the Cu (North) and the ferroalloy (South) at a temperature of 1090 °C, while Figure 6.8b presents a close-up cross-sectional view of the copper balling at 1130 °C.

Figure 6.9a presents a EDS area scan of the green Cu slug. Figure 6.9b presents a BSD image of the inclusion area presented in Figure 6.9a.

Figure 6.10 presents the quantity of minimum, mean, and maximum pore dimensions grouped in intervals of 10 μm over the entire range of pore size found.

[4]The already available EDS area scans were used in this instance due to the additional time required to extract the Mn composition data from the WDS scans, which were not of interest when the Cu data was first extracted.

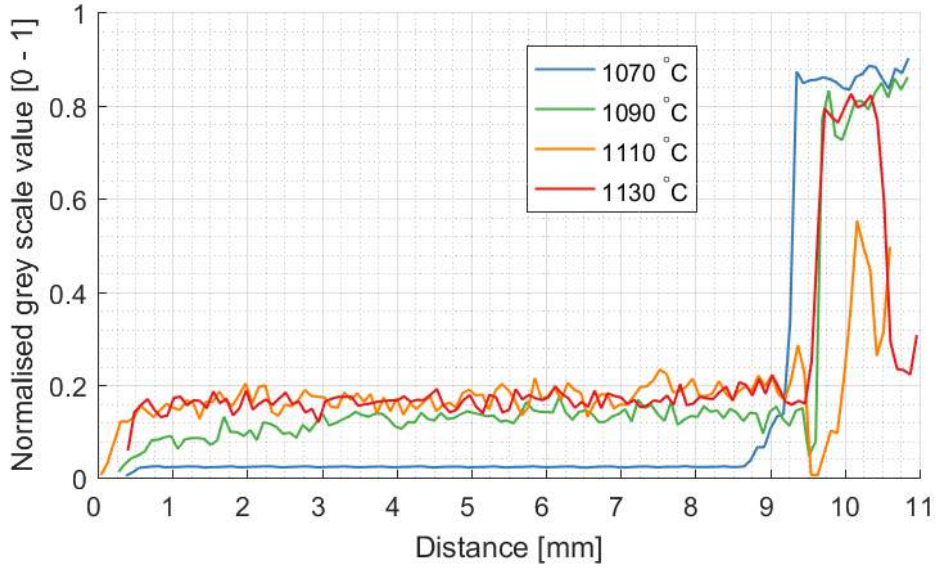

Figure 6.6: Normalised Cu content

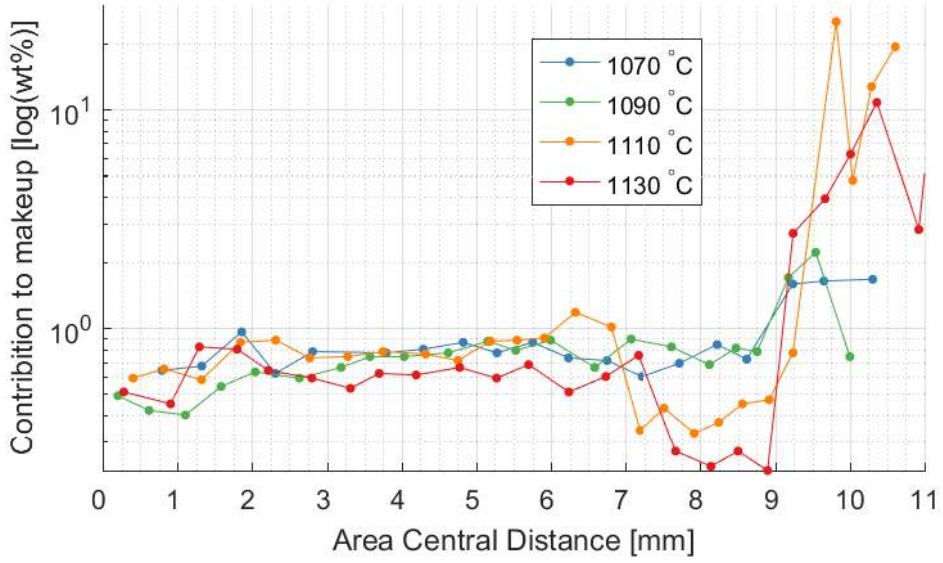

Figure 6.7: Normalised Mn content

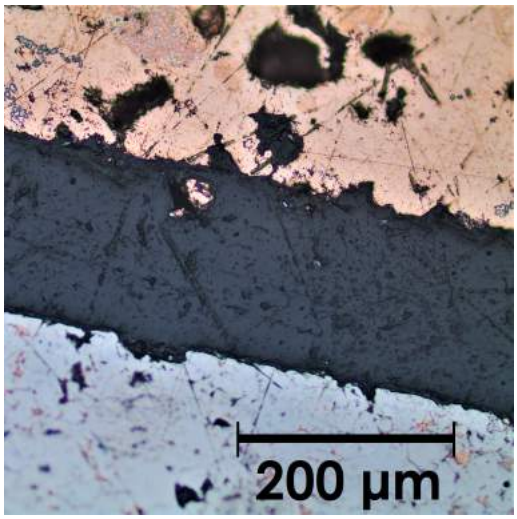

(a) Cu-Mn Phase formation on the Cu slug interface at 1090 °C, optical microscope image taken at 200x magnification

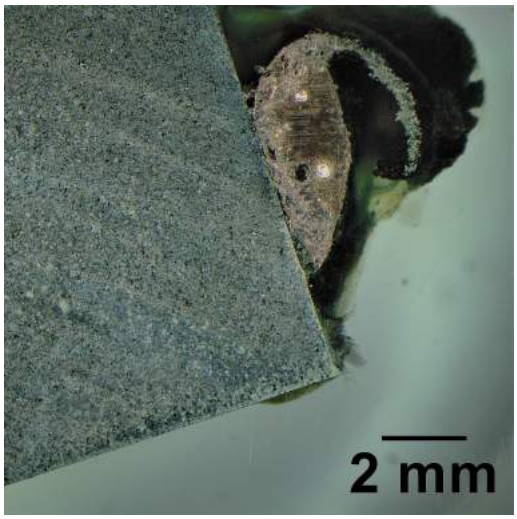

(b) Post sinter-infiltration, at 1130 °C, stereo microscope image taken at 8x magnification

Figure 6.8: Microscopy images of Cu interface

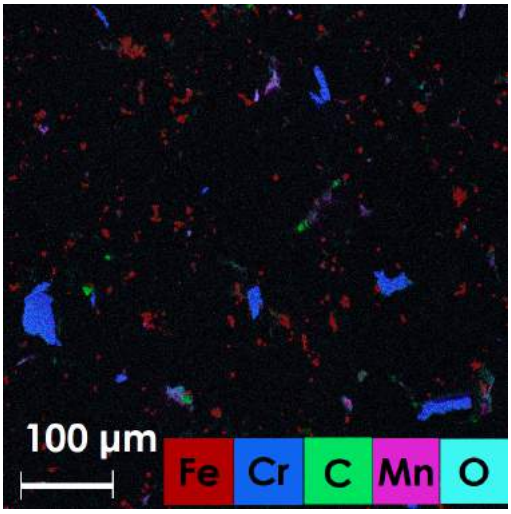

(a) Green Cu part inclusions

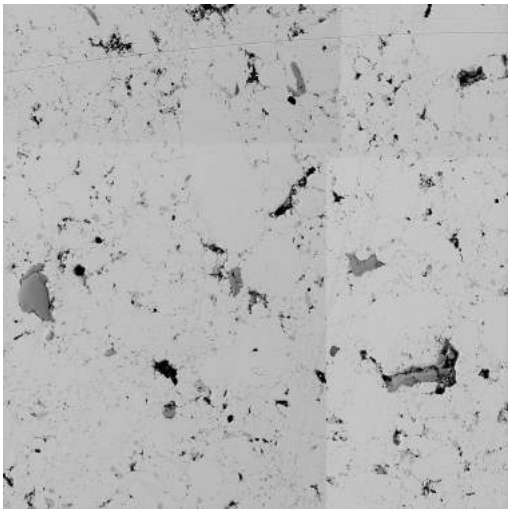

(b) Cu green part BSD image of inclusion area

Figure 6.9: Green Cu slug inclusions

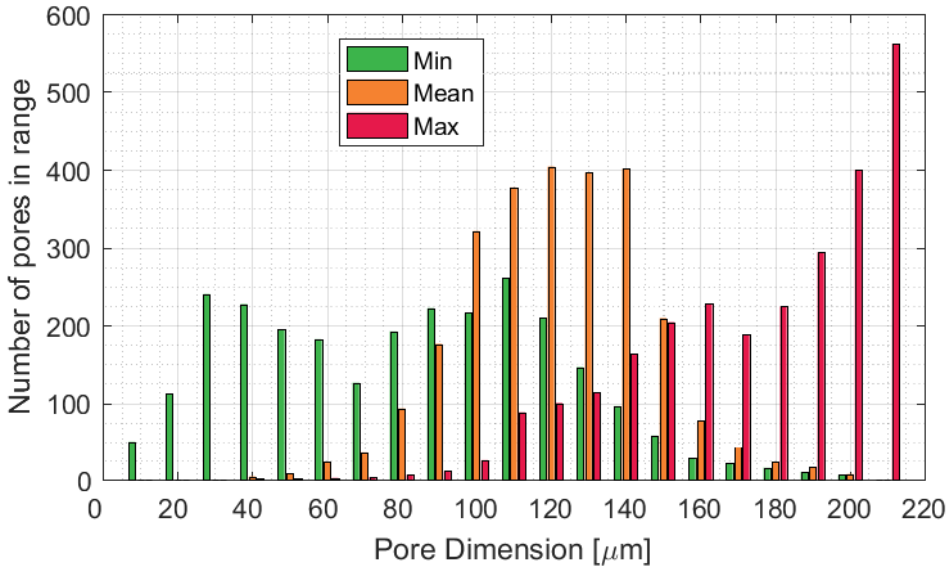

Figure 6.10: Pore size distribution at 1070 °C

6.2.3 Discussion

From Figure 6.4 it can be seen that the samples were clean after sinter-infiltration. When comparing the sample images of the current experiment with that of Section 6.1, a large decrease in oxidation and surface sooting can be seen. This indicates that the combination of the full use of the bubbler and the transient atmosphere resulted in cleaner samples with more complete delubrication.

Analysis of the WDS scans presented in Figure 6.5 reveal that W and V make up the same areas. O and Mn can also be seen to correspond on the uninfiltrated Cu residue. This result can be explained through Mn's high affinity towards oxygen [75].

Infiltration appears to be relatively homogeneous at 1110 °C, as seen in Figure 6.5. Comparing the progress of infiltration between the different temperature samples reveals that infiltration occurs suddenly and rapidly between 1070 and 1090 °C. It can be noted that some infiltration had taken place at 1070 °C, which is lower than the melting point of pure Cu. Consulting the Cu-Mn phase diagram of Figure C.3 it can be seen that Mn is capable of lowering the melting temperature of Cu. Therefore, as solid diffusion of Mn into the Cu slug occurred at the elevated temperature, the melting point of Cu was lowered enough for some infiltration to occur at or before 1070 °C.

Interestingly the high concentration Mn areas, of ~9 μm in diameter, do not correspond to most of S containing areas, as is expected for a material lubricated with solid lubricant MnS. S is used to inhibit C diffusion from the

graphite powder, thus retaining the benefits of graphite lubrication whilst simultaneously preventing the graphite from adversely affecting material properties [5:1720]. Furthermore, it can be seen that molybdenum (Mo) and sulphur areas correspond, thus indicating the presence of the lubricant molybdenum disulfide (MoS_2).

A closer look at the Mn concentration, from west to east in Figure 6.5, reveals that some solid lubricant sweeping had taken place. A clear change in Mn concentration is found near a distance of 7 mm, more noticeably visible in Figure 6.7 where the Mn concentration suddenly decreases from ~1.5 to ~1.1 wt%. In Figure 6.7 Mn concentration can be seen to rapidly decrease between 1090 and 1110 °C and further decreasing, in this area with increasing temperature. This rapid decrease in Mn concentration occurs at a similar time as the rapid infiltration had occurred. However, instead of finding a larger concentration of Mn between 0 – 7 mm as a result of infiltration, Mn had moved to the uninfiltrated Cu on top of the sample, travelling in the opposite direction as infiltration. Here it was exposed to the oxygen species in the atmosphere an subsequently oxidised.

As previously mentioned Mn diffuses into Cu during heating to the sintering temperature, where it creates a solid solution with Cu. The Cu-Mn alloy has a lower melting point of than pure Cu and therefore starts to melt earlier. The liquid Cu-Mn alloy subsequently enters the capillaries, engulfing Mn particles and dissolving/eroding sintering necks. The necks are preferentially dissolved due to the same driving forces for neck formation, high curvature [76], as explained in Section 2.1.7. The Mn particles, with a density of 7,43 g/cc [30], becomes positively buoyant in the liquid Cu with a density of 7.96 g/cc. These particles, once sufficiently eroded through diffusion into the liquid Cu, pass through the capillaries under the influence of buoyancy and travel towards the top of the sample. The result is that the Mn concentration moves upwards, against gravity and gravity assisted infiltration. This solution of Mn into Cu is believed to persist until the sintering temperature is reached, whereupon the remaining porosity is filled so rapidly that the Mn particles cannot be dissolved into the molten Cu fast enough in order to escape through the capillaries. The result then is that a clear change in Mn concentration is found at the depth, ~2.3 mm, to which Mn particles had sufficiently eroded to escape through the capillaries.

Figure 6.8a indicates the formation of a Cu-Mn layer between the Cu slug (north) and the ferroalloy sample (south). Mn is capable of lowering the melting point of Cu up to a concentration of 34.6 wt% Mn, whereafter any increase in Mn concentration tends to increase the melting point of the solution. Very high concentration areas of Mn can be seen in the vicinity of the uninfiltrated Cu. It is, therefore, possible that the high concentrations of Mn near the Cu slug interface caused the Cu-Mn solution's melting

temperature to increase above that of the sinter-infiltration temperature, causing recrystallization of FCC Cu-γMn or BCC Cu-δMn on the Cu slug interface [64]. This higher melting point phase acted to close the capillaries by forming a physical barrier and so preventing further infiltration. Furthermore, the contact angle between the molten Cu and the Cu-Mn solid is believed to be >90 °C, resulting in the copper balling seen in the sinter-infiltrated samples in Figure 6.4.

Consulting Figure 6.9 it can be seen that relatively large, ~80 μm, particles of Cr are present in the green Cu slug. It is possible that these inclusions also inhibit sinter-infiltration. The melting point of all the inclusions seen in Figure 6.9a is above that of Cu. Therefore, as the Cu becomes liquid and infiltrates the ferroalloy sample, the inclusions will remain behind if they are not capable of passing through the capillaries. The inclusions moving with Cu through the capillaries may encounter Mn particles moving in the opposite direction, thus causing interference and possibly pore closure, preventing infiltration. From Figure 6.10 it can be deduced that a considerable percentage, ~50 %, of the minimum pore sizes at 1070 °C are smaller than 80 μm, thus preventing the Cu inclusions from travelling through the pores.

It can be seen that the inclusions are irregularly shaped. This affects the observed contact angle, which can result in contact angles that are larger than 90 ° and thus negatively affect infiltration. Additionally, also leading to the phenomenon of copper balling.

Chapter 7

Conclusions

This project investigated the critical sintering process parameters for high-quality Cu sinter-infiltration of conventional ferrous PM alloys. The successful completion of this research aim required that a pusher furnace at SU be refurbished. The refurbishment entailed, mainly, replacement of the furnace power supply, modification and calibration of the process gas system, and adaptations to the standard operating procedure of the furnace. These actions resulted in fully functional equipment suitable for the executing research experiments.

The delubrication behaviour of EBS was studied through thermoanalytic methods as well as furnace experiments. It was found that EBS has a melting temperature of ~145 °C which is in close agreement with the reported melting temperature. A characteristic temperature in N_2 of 470 °C was witnessed, which does not correlate well with literature, where a characteristic temperature of 438 °C is reported [46]. It was seen that EBS loses ~98 wt% during heating from 50 – 700 °C at 7 and 50 °C/min in an N_2 or atmospheric air atmospheres.

However, furnace delubrication with 2 wt% zinc stearate samples, in an 80:20 N_2:H_2 atmosphere, indicated that longer hold times (20 to 30 min) at a delubrication temperature of 700 °C resulted in a larger mass loss. The optimal delubrication temperature of 700 °C was determined through isothermal decomposition of zinc stearate specimens in a thermoanalytic device. This investigation is presented in Appendix D.2.

The effect of sintering process parameters on conventional PM was studied through comparing different furnace operation and atmosphere control concepts, namely 1) discrete furnace operation with a continuous atmosphere and 2) discrete furnace operation with a transient atmosphere. Briefly, the latter differs from the former in that the furnace conditions are tailored to suit the requirements of a single sample set moving through the different furnace zones. The continuous atmosphere was found to be unsuitable due to incomplete delubrication, oxidation, and unreliable sintering results. In

contrast, the transient atmosphere operation resulted in reliably clean sinter-infiltration results, with the only impediment that of the black residue which required further investigation.

The cause and effect of the black residue formation was investigated using several techniques. It was found that Mn lowers the melting temperature of Cu sufficiently to cause a small amount of infiltration to occur at 1070 °C. Sudden and rapid infiltration was found to occur at a temperature between 1070 and 1090 °C. Mn was removed from the infiltration area to a depth of approximately 2.3 mm. The Mn was, however, not swept down in the direction of infiltration, but rather upwards where Mn reacted with oxygen species on the surface of the molten Cu infiltrate. The cause of the movement of Mn can possibly result from two phenomenon or a combination thereof: 1) the diffusion of Mn into Cu, 2) the buoyancy of Mn in molten Cu.

Furthermore, infiltration was inhibited causing copper balling to occur. Infiltration was inhibited by the following phenomenon: 1) particle inclusions in the Cu infiltrate that cannot pass through capillaries due to their size and shape, 2) the formation of a Cu-Mn layer between the Cu slug and the porous matrix, 3) pore clogging as a result of the movement of Mn particles due to buoyancy.

Chapter 8

Recommendations

Herewith follow recommendations from the author upon completion of the research project:

1. Sintering with the Cu slug underneath the ferroalloy compact may result in the liquid Cu being pulled up into the porous part, whilst possibly preventing the Mn concentration from becoming too high.
2. Investigation of the effects on the formation of black residue and copper pooling using alternative solid lubricants to MnS.
3. Investigation of the delubrication process in a thermoanalytic device using a N_2:H_2 atmosphere with the addition also of water vapour.
4. The pusher furnace heating elements should be inspected.
5. The central furnace tube should be replaced, due to the cracks which pose considerable oxidation risk to the heating elements.
6. Elemental composition analyses on the black residue layer formation at the copper-alloy interface.

Chapter 9

References

[1] R.M. German. *Powder Metallurgy and Particulate Materials Processing*. Metal Powder Industries Federation, 2005. ISBN 0976205718.

[2] A.C. Reardon. *Metallurgy for the Non-Metallurgist, Second Edition*. EngineeringPro collection. ASM International., 2011. ISBN 9781615038459.

[3] M.P. Groover. *Fundamentals of Modern Manufacturing: Materials, Processes, and Systems*. John Wiley & Sons, 5 edition, 2012. ISBN 9781118476550.

[4] Höganäs. *Handbook 3: Design and Mechanical Properties*. Höganäs Handbook for Sintered Components. Höganäs AB, 2015.

[5] ASM International Handbook Committee. *Powder Metal Technologies and Applications*, volume 7 of *ASM Handbook*. ASM International, 1998. ISBN 9780871703873.

[6] G. Dowson and D. Whittaker. *Introduction to Powder Metallurgy: The Process and its Products*. EPMA education & training. European Powder Metallurgy Association (EPMA), 2008.

[7] J. Das, A. Chakraborty, T.P. Bagchi, and B. Sarma. Improvement of machinability of tungsten by copper infiltration technique. *International Journal of Refaractory Metals & Hard Materials*, 26(6):530 – 539, Jan 2008. ISSN 0263-4368.

[8] SCM Metal Products. Infiltration powders and application guide, 2017. [Online]. Available: `http://www.scmmetals.com/infiltration-sinterbrazing` [2017, February 09].

[9] Metal Powder Industries Federation. Powder metallurgy – intrinsically sustainable, n.d. [Online]. Available: `https://www.mpif.org/IntroPM/PDFs/PM-Intrinsically-Sustainable.pdf` [2018, Feb 27].

[10] Department of Environment and Tourism. National framework for sustainable development in south africa, June 2008. [Online]. Available: https://www.environment.gov.za/documents/strategicdocuments/nfsd [2018, Feb 08].

[11] Department of Environmental Affairs. National strategy for sustainable development and action plan, 2011. [Online]. Available: https://www.environment.gov.za/node/21/edit?q=content/documents/strategic_docs/national_strategy_sustainable_development [2018, Feb 08].

[12] United Nations. Report of the united nations conference on sustainable development. 6 2012.

[13] European Commission. Europe 2020 a european strategy for smart, sustainable and inclusive growth. 2010.

[14] Metal Powder Industries Federation. Powder metallurgy: A green technology, 2018. [Online]. Available at: https://www.mpif.org/IntrotoPM/AGreenTechnology.aspx [2018, August 20].

[15] F. Bernier, P. Beaulieu, J-P. Balon, and G.L. Espérance. Effect of cu infiltration on static and dynamic properties of pm steels. *Powder Metallurgy*, 54(3):314 – 319, 2011. doi: 10.1179/003258909X12502872942615.

[16] M. Madej and J. Lezaski. Copper infiltrated high speed steel based composites. *Archives of Metallurgy and Materials*, 50:871 – 877, 01 2005.

[17] S. Klein, S. Weber, and W. Theisen. Effect of heat treatment on phase structure and thermal conductivity of a copper-infiltrated steel. *Journal of Materials Science*, 50(10):3586 – 3596, 5 2015. doi: 10.1007/s10853-015-8919-y.

[18] H. Sanderow and P. Rivest. Mechanical properties of copper infiltrated low alloy steels using wrought wire infiltrant. 01 2007.

[19] Air Products and Chemicals, Inc. Introduction to furnace brazing, 2001.

[20] Powder Metallurgy Review., 2018. [Online]. Available: http://www.pm-review.com/introduction-to-powder-metallurgy/powder-production-technologies [2018, February 08].

[21] Copper Development Association Inc. Production and properties of copper and copper alloy powders, 2017. [Online]. Available: https://www.copper.org/resources/properties/129_6/production.html#a2 [2018, March 29].

[22] Höganäs. *Handbook 1: Material and Powder Properties*. Höganäs Handbook for Sintered Components. Höganäs AB, 2013.

[23] Lonza. Product datasheet: Acrawax c, 2011. [Online]. Available: `http://bio.lonza.com/uploads/tx_mwaxmarketingmaterial/Lonza_ProductDataSheets_Acrawax_C_PDS.pdf` [2017, September 14].

[24] Compound Summary for CID 11178, 03 2018. [Online]. Available: `https://pubchem.ncbi.nlm.nih.gov/compound/zinc_stearate#section=Top` [2018, March 30].

[25] Compound Summary for CID 8044, 03 2018. [Online]. Available: `https://pubchem.ncbi.nlm.nih.gov/compound/Plastflow/#section=Top` [2018, March 30].

[26] Compound Summary for CID 12406, 03 2018. [Online]. Available: `https://pubchem.ncbi.nlm.nih.gov/compound/pentacosane#section=MeSH-Entry-Terms` [2018, March 30].

[27] Lithium Stearate MSDS, 09 2011. [Online]. Available: `http://datasheets.scbt.com/sc-279277.pdf` [2018, March 30].

[28] Höganäs. *Handbook 2: Production of Sintered Components*. Höganäs Handbook for Sintered Components. Höganäs AB, 2013.

[29] M. M. Baum, R. M. Becker, A. M. Lappas, J. A. Moss, D. Apelian, D. Saha, and V. A. Kapinus. Lubricant pyrolysis during sintering of powder metallurgy compacts. *Metallurgical and Materials Transactions B*, 35(2):381 – 392, Apr 2004. ISSN 1543-1916. doi: 10.1007/s11663-004-0038-0.

[30] Densities of Solids, 2016. [Online]. Available: `http://www.engineeringtoolbox.com/density-solids-d_1265.html` [2016, June 29].

[31] Metals - Melting Temperatures, 2016. [Online]. Available: `http://www.engineeringtoolbox.com/melting-temperature-metals-d_860.html` [2016, June 29].

[32] Thermal Conductivity of Metals, 2016. [Online]. Available: `http://www.engineeringtoolbox.com/thermal-conductivity-metals-d_858.html` [2016, June 29].

[33] Vickers Hardness of the Elements, 2016. [Online]. Available: `http://periodictable.com/Properties/A/VickersHardness.al.html` [2016, June 27].

[34] StrengthMechanics of Materials, 2016. [Online]. Available: http://www.engineersedge.com/material_science/yield_strength.htm [2016, June 29].

[35] Z.Z. Fang. *Sintering of Advanced Materials*. Woodhead Publishing Series in Metals and Surface Engineering. Elsevier Science, 2010. ISBN 9781845699949.

[36] D. Whittaker. Introduction to powder metallurgy, 2016. [Online]. Available: http://www.ipmd.net/Introduction_to_powder_metallurgy/Sintering [2016, June 27].

[37] J.R. Groza and J.F. Shackelford. *Materials Processing Handbook*. CRC Press, 2007. ISBN 9781420004823.

[38] R.M. German. Sintering trajectories: Description on how density, surface area, and grain size change. *JOM*, 68(3):878 – 884, 03 2016. ISSN 1543-1851. doi: 10.1007\/s11837-015-1795-8.

[39] R.M. German. *Sintering Theory and Practice*. John Wiley & Sons, 1996. ISBN 0-471-05786-X.

[40] S.L. Feldbauer and A. Malas. Gassing up to get the right atmosphere. *Metal Powder Report*, 62(5):14 – 19, 2007. doi: 10.1016/S0026-0657(07)70104-2.

[41] T. Philips, J.J. Dwyer, and Z. Zurecki. Techniques and tips to optimize, control and control and stabilize the atmosphere inside a continuous sintering furnace. 2011. [Online]. Available: http://www.airproducts.com/{~}/media/downloads/white-papers/A/en-atmos-cont-sintering-furnace-330-11-006-US.pdf [2017, Oct 29].

[42] G.S. Upadhyaya. *Powder Metallurgy Technology*. Sintering atmosphere. Cambridge Int. Science Publishing, 1997. Section 6.8.

[43] Y.A. Cengel and M.A. Boles. *Thermodynamics: An Engineering Approach*. Cengel series in engineering thermal-fluid sciences. McGraw-Hill, 1221 Avenue of the Americas, New York, NY 10020, 7 edition, 2011. ISBN 9780071311113.

[44] G.P. Vyatkin, G.G. Mikhailov, Y.S. Kuznetsov, O.I. Kachurina, and S.V. Digonskii. Reduction of iron oxides in a humid atmosphere. *Steel in Translation*, 42(2):103 – 106, 02 2012. ISSN 1935-0988. doi: 10.3103/S0967091212020301.

[45] L.F. Pease and W.G. West. *Fundamentals of Powder Metallurgy*. Metal Powder Industries Federation, 2002. ISBN 9781878954862.

[46] D. Saha and D. Apelian. Control strategy for de-lubrication of p/m compacts. *International Journal of Powder Metallurgy*, 38(3):71 – 79, 2002.

[47] ASM International Handbook Committee and J.R. Davis. *Machining*, volume 16 of *ASM Handbook*. ASM International, 1999. ISBN 9780871700223.

[48] J.P. Davim. *Machining of Metal Matrix Composites*. Springer series in advanced manufacturing. Springer London, 2011. ISBN 9780857299383.

[49] Copper Development Association Inc. Copper in iron and steel p/m parts, 2016. [Online]. Available: `http://www.copper.org/resources/properties/129_6/copper_iron.html` [2016, June 27].

[50] M. Silberberg. *Principles of General Chemistry*. Intermolecular forces: Liquids, Solids and Phase Changes. McGraw Hill, 2 edition, 2007.

[51] Contact Angles, 2016. [Online]. Available: `http://chemwiki.ucdavis.edu/Core/Physical_Chemistry/Physical_Properties_of_Matter/Bulk_Properties/Cohesive_And_Adhesive_Forces/Contact_Angles` [2016, June 29].

[52] N. Eustathopoulos. Wetting by liquid metals – application in materials processing: The contribution of the grenoble group. *Metals*, 5(1):350 – 369, 3 2015. ISSN 2075-4701. doi: 10.3390/met5010350.

[53] D. Yunus A. Cengel and J.M. Cimbala. *Fluid Mechanics: Fundamentals and Applications*. McGraw-Hill Education, 2010. ISBN 9780071284219.

[54] F.M. White. *Fluid Mechanics*. McGraw-Hill series in mechanical engineering. McGraw Hill, 2011. ISBN 9780073529349.

[55] Capillary Pressure, 2016. [Online]. Available at: `http://web.mst.edu/{~}numbere/cp/chapter%203.htm` [2016, June 28].

[56] B. Larson, United States. Federal Aviation Administration. Office of Aviation Research, William J. Hughes Technical Center (U.S.), and Center for Aviation Systems Reliability (U.S.). *Study of the Factors Affecting the Sensitivity of Liquid Penetrant Inspections: Review of Literature Published from 1970 to 1998*. AD-a399 887. Office of Aviation Research, U.S. Federal Aviation Administration, 2002.

[57] M. Motoyoshi and M. Osawa. Valve seat material for internal combustion engines and the similar material, 9 1970.

[58] A. Fujiki, Y. Yasuda, I. Tanimoto, H. Endo, Y. Ikenoue, and K. Suzuki. Heat resistant and wear resistant iron-base sintered alloy, 7 1987.

[59] M. Osawa, Y. Hagiwara, K. Kusaka, T. Kawakita, K. Motoyoshi, and N. Kuroishi. Valve seat materials for internal combustion engines, 6 1973.

[60] S. Urano, K. Yamamoto, Y. Takagi, and T. Sugawara. Sintered alloy for valve seat, 7 1982.

[61] W. Callister and D. Rethwisch. *Material Science and Engineering*. John Wiley & Sons, Inc., 8 edition, 2011.

[62] Metastable Iron-Carbon (Fe-C) Phase Diagram., 2011. [Online]. Available at: `http://www.calphad.com/iron-carbon.html` [2018, Feb 26].

[63] H. Okamoto. The c-fe (carbon-iron) system. *Journal of Phase Equilibria*, 13(5):543–565, 1992. doi: 10.1007/BF02665767.

[64] H. Baker. *Alloy Phase Diagrams*, volume 3 of *ASM Handbook: Alloy Phase Diagrams*. ASM International, 1992. ISBN 9780871703811.

[65] K. Shubhank and Y. Kang. Critical evaluation and thermodynamic optimization of fecu, cuc, fec binary systems and fecuc ternary system. *Calphad*, 45:127 – 137, 2014. ISSN 0364-5916. doi: 10.1016/j.calphad.2013.12.002.

[66] K. Parameswaran, K. Metz, and A. Morris. Phase equilibria for iron-rich Fe-Cu-C alloys: 1500 to 950 °C. *Metallurgical Transactions A*, 10(12):1929 – 1939, 12 1979. ISSN 1543-1940. doi: 10.1007/BF02811739.

[67] S. Weis, T. Uhlig, G. Wagner, T. Lampke, W. Bauer, and A. Moldenhauer. High-temperature corrosion and radiation characteristics of thermal sprayed molybdenum disilicide-based coatings. *IOP Conference Series: Materials Science and Engineering*, 118(1):012007, 03 2016. doi: 10.1088/1757-899X/118/1/012007.

[68] AZoM.com. Molybdenum disilicide, 05 2001. [Online]. Available at: `https://www.azom.com/article.aspx?ArticleID=512` [2018, April 12].

[69] Practical Control Solutions. Characteristics of silicon carbide heaters, 2014. [Online] Available: `http://www.practicalcontrol.com.au/molybdenum_disilicide_MoSi2_control.html` [2017, March 21].

[70] D. Gandy. *Carbon Steel Handbook: 1014670*. Electric Power Research Institute, March 2007.

[71] S. Degaleesan, M. Dudukovic, and Y. Pan. Experimental study of gas-induced liquid-flow structures in bubble columns. *AIChE Journal*, 47(9):1913 – 1931, 2001.

[72] M. Zizka, R. Sulc, and P. Ditl. Heat transfer between gas and liquid in a bubble column. *Chemical Engineering Transactions*, 57, 2017. doi: 10.3303/CET1757211.

[73] R.S. Figliola and D.E. Beasley. *Theory and Design for Mechanical Measurements*. John Wiley and Sons, 5 edition, 2011. ISBN 9780470547410.

[74] M.W.J. Chase. *NIST-JANAF Thermochemical Tables*. Journal of Physical and Chemical Reference Data Monographs. American Inst. of Physics, 1998. ISBN 9781563968310.

[75] E. Hryha and E. Dudrova. *The Sintering Behaviour of Fe-Mn-C Powder System, Correlation between Thermodynamics and Sintering Process, Manganese Distribution and Microstructure Composition, Effect of Alloying Mode*. IntechOpen, Rijeka, 2011. doi: 10.5772/13735.

[76] Nicholas B. Erhardt, Pavan Suri, and Randall German. A study of the microstructural evolution of tungsten heavy alloys during liquid phase sintering. 5, 01 2003.

[77] I. Poole. Non-inverting amplifier circuit using an op-amp, 2017. [Online] Available: `http://www.radio-electronics.com/info/circuits/opamp_non_inverting/op_amp_non-inverting.php` [2017, April 13].

[78] A.R. Hambley. *Electrical Engineering: Principles and Applications*. Upper Saddle River, NJ Pearson Education, Inc, 5 edition, 2011. ISBN 9780132155168.

[79] M. Holmgren. X steam, thermodynamic properties of water and steam, 2007. Based on the "International Association for Properties of Water and Steam Industrial Formulation 1997 (IAPWS IF-97)". A full implementation of the IF-97 standard that provides very accurate steam and water properties in ranges from 0-1000 bar and 0-2000 °C.

[80] R. M. Davies, G. Taylor, and F. R. S. The mechanics of large bubbles rising through extended liquids and through liquids in tubes. *Proceedings of the Royal Society of London A: Mathematical, Physical and Engineering Sciences*, 200(1062):375 – 390, 1950.

[81] R. Clift, J.R. Grace, and M.E. Weber. *Bubbles, Drops and Particles*. Academic Press, 1978. ISBN 9780121769505.

[82] A.F. Mills and V Ganesan. *Heat Transfer*. Pearson Education, 2 edition, 2015. ISBN 9788131727133.

[83] Y.A. Cengel and A.J. Ghajar. *Heat and Mass Transfer: Fundamentals & Applications*. McGraw-Hill Education, 5 edition, 2014. ISBN 9789814595278.

[84] E.R. Gilliland. Diffusion coefficients in gaseous systems. *Industrial & Engineering Chemistry*, 26(6):681 – 685, 1934. doi: 10.1021/ie50294a020.

[85] Polyvinyl Chloride (PVC), 2017. [Online]. Available: http://www.lenntech.com/polyvinyl-chloride-pvc.htm [2017, May 24].

[86] PVC and CPVC Pipes - Schedule 40 & 80, 2017. [Online]. Available: http://www.engineeringtoolbox.com/pvc-cpvc-pipes-dimensions-d_795.html [2017, May 24].

[87] Harvel. Product specification clear pvc pipe scheule 40 and schedule 80, 2017. [Online]. Available: https://www.usplastic.com/catalog/files/34100specsheet10-2004.pdf [2017, May 24].

[88] A.M. Helmenstine. Aliphatic hydrocarbon definition, 2017. [Online]. Available: https://www.thoughtco.com/definition-of-aliphatic-hydrocarbon-604763 [2017, May 24].

[89] E. Hahn. What is lpg? liquefied petroleum gas - propane, 2017. [Online]. Available at: http://www.elgas.com.au/blog/492-what-is-lpg-lpg-gas-lp-gas [2017, May 24].

[90] Marley Pipe Systems. Megaflex hose technical manual, 2017. [Online]. Available: http://www.marleypipesystems.co.za/mining-and-industrial-pipeline-solutions/pipeline-construction-and-design-downloads/pipe-technology-and-products-manuals [2017, May 24].

[91] Professional Plastics. Pvc pipe specifications, 2017. [Online]. Available: https://www.professionalplastics.com/professionalplastics/PVCPipeSpecifications.pdf [2017, May 24].

[92] UL International TTC GmbH. Flammability ul 94 v, 2017. [Online]. Available at: https://www.ulttc.com/en/solutions/test-methods/combustion-fire/flammability/flammability-ul-94-v.html [2017, October 28].

[93] J. Schmuller. *Statistical Analysis with Excel for Dummies*. John Wiley & Sons, 3 edition, 2013. ISBN 9781118464311.

[94] T. Matsumoto, H. Fujii, T Ueda, M Kamai, and K Nogi. Measurement of surface tension of molten copper using the free-fall oscillating drop method. *Measurement Science and Technology*, 16(2):432, 2005. doi: 10.1088/0957-0233/16/2/014.

[95] S.W. Strauss. The temperature dependence of the viscosity of liquid metals. *Nuclear Science and Engineering*, 12(3):436 – 439, 1962. doi: 10.13182/NSE62-A28099.

[96] D. Cripps. Formulae, 2016. [Online]. Available: http://www.netcomposites.com/guide-tools/guide/formulae [2016, July 21].

Appendix A

Electrical Refurbishment

A.0.1 Heating Element Resistances

Figure A.1 presents the estimated resistances of the three furnace heating elements with temperature.

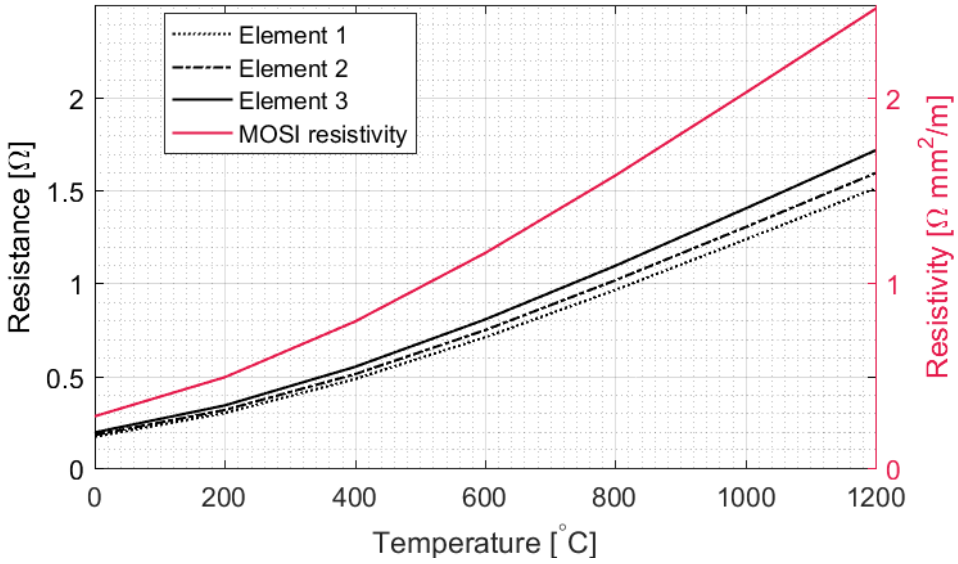

Figure A.1: Element resistances with temperature

A.1 Electrical Circuit

A.1.1 Circuit Diagram

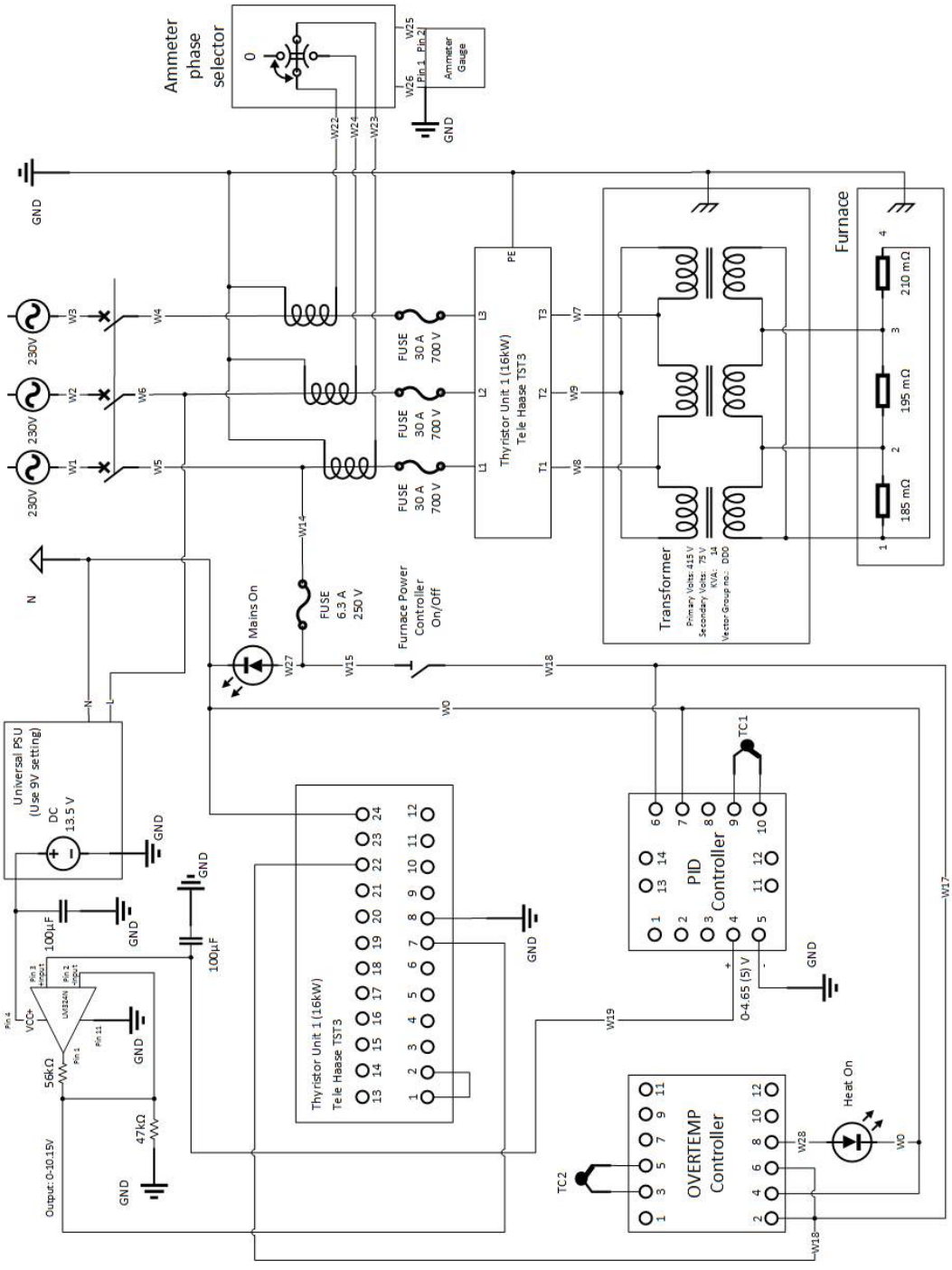

Figure A.2: Pusher furnace circuit diagram

A.2 Temperature Controller

A.2.1 Programming Settings

Table A.1 presents the settings used for the PID controller, REX-D100, during this project.

Table A.1: Temperature controller, RKC REX-D100, parameter group settings

Parameter Group	Description	Setting
PG1	Correction bias for measurement value (PV)	Pb = 0 °C
PG2	Set value (SV) change rate limit	SVrL = 0 °C/min
PG3	Alarm 1 action Differential gap Alarm delay Alarm break LBA dead band	AS1 = 0 (off) AH1 = 2 °C ALT1 = 0 sec LbA = 0 (off) Lbd = 0 (off)
PG4	Alarm 2 action Differential gap Alarm delay	AS2 = 0 (off) AH2 = 2 °C ALT2 = 0 sec
PG5	Proportional band Integral time Derivative time Anti-reset wind-up ON/OFF differential gap Manual reset Fuzzy logic	P = 100 °C I = 30 sec d = 60 sec Ar = 100 % of P oH = 2 °C Mr = 0 % FUZZ = 0 (off)
PG6	Output high limit Output low limit Direct or reverse control action	oLH = 105 % oLL = 0 %
PG7	Analog output Analog high limit Analog low limit (0 = scaling low to high limit)	Ao = 0 (PV) AHS = 0 ALS = 0
PG8	Not displayed when there is no communication function	SC1

A.2.2 Control Signal Op-amp Circuit Design

The REX-D100 PID controller can only output a 0 – 5 V DC control signal. The signal must, therefore, be amplified with a gain of 2 to get full output. The gain calculation is given in Equation A.1 [77]. Measurement of the actual

PID control signal showed that the maximum voltage was in reality 4.65 V, not 5 V. Thus, a larger than 2 gain was required for the control signal.

$$\frac{V_{out}}{V_{in}} = G = 1 + \frac{R_2}{R_1} \tag{A.1}$$

A non-inverting op-amp circuit, seen in Figure A.2, was designed in LTspice XVII and built by Mr AP Scholtz. A universal, adjustable, charging unit was purchased to be used as the power supply to the op-amp. It was found that its output voltage on the 9 V setting is 13.5 V, which is sufficient for the op-amp to deliver a maximum output voltage of 10 V. A Texas Instruments LM324N op-amp was used in the circuit. It was found that a resistor combination of 47 kΩ and 56 kΩ gave the best output results in reality. The gain of this resistor combination was calculated in Equation A.2.

$$G = 1 + \frac{56}{47} = 2.19 \tag{A.2}$$

The PID controller voltage output (V_in) was plotted along with the op-amp output voltage (V_out) versus the manual setting scale, -5 – 105. The plot can be seen in Figure A.3. From this, it can be seen that there is a very good linear relationship between the manual scaling and PID controller output voltage, as well as a constant gain over the op-amp circuit.

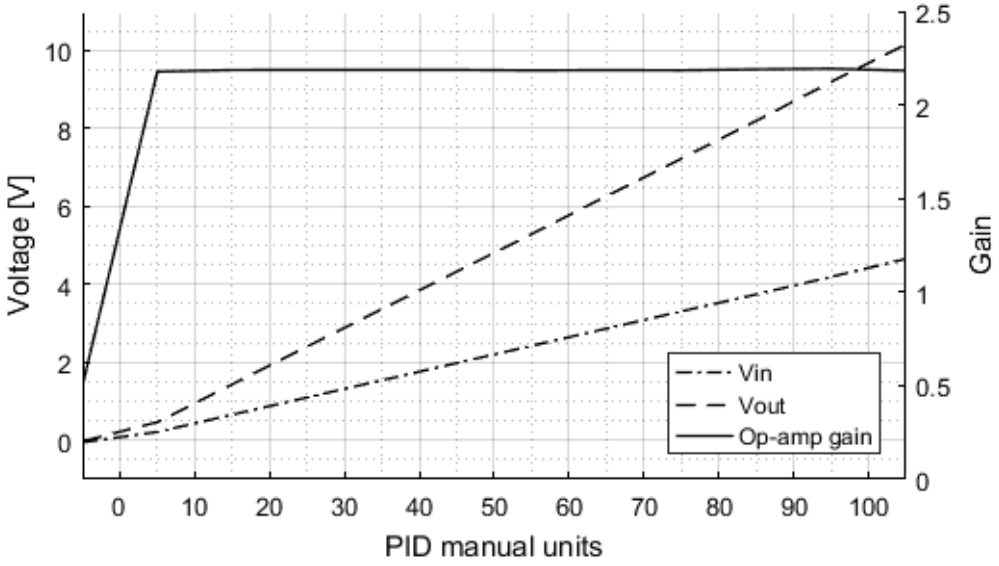

Figure A.3: Op-amp control voltages and gain

A.3 Thyristor Information

A.3.1 Thyristor Waveform

Figure A.4 presents the combined voltage waveform resulting in maximum three-phase power output for the thyristor.

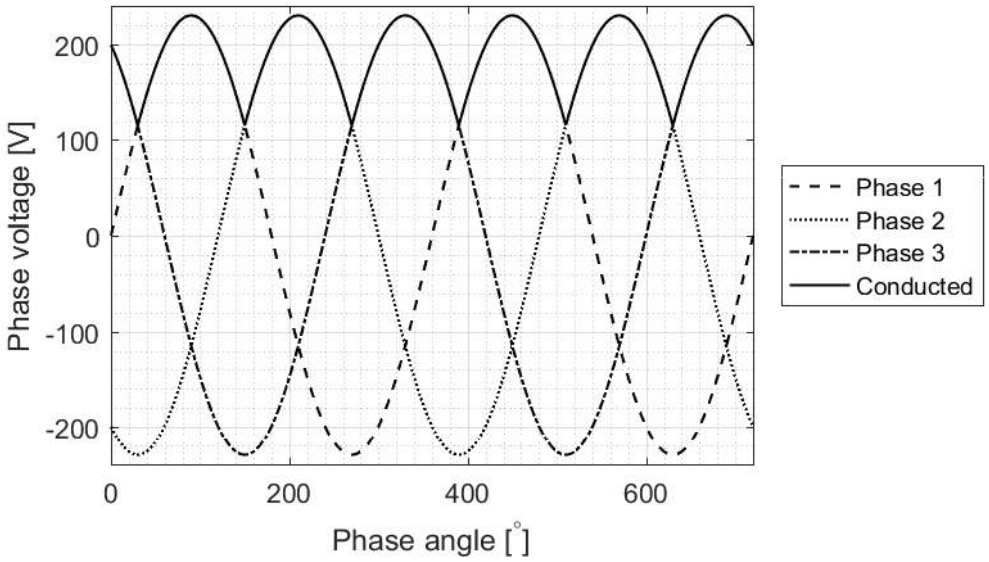

Figure A.4: Maximum power conduction characteristic curve for a three-phase thyristor unit

A.3.2 Thyristor Specifications

Considering the thyristor, transformer and element electrical circuits. It can be noted that the elements, as well as the transformer (primary and secondary), are in delta configurations. The heating element resistances, given in the circuit diagram of Figure A.2, are comparable with each other. It can, therefore, be assumed that the elements have equal impedances, resulting in a balanced delta circuit. For the purposes of simplifying calculations, an equivalent wye connected circuit can be calculated, which allows single-phase analysis of the circuit. The equivalent delta and wye circuits (including only the secondary side of the transformer) are given in Figure A.5 adapted from [78].

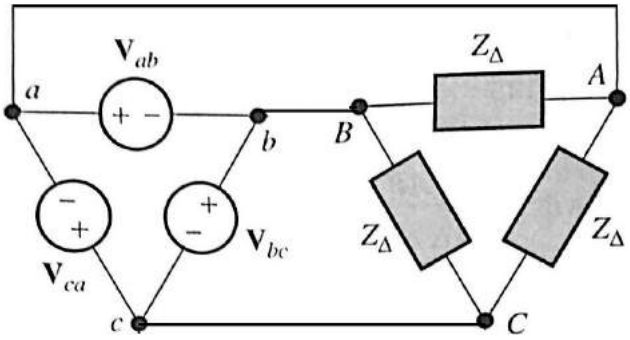

(a) Delta circuit

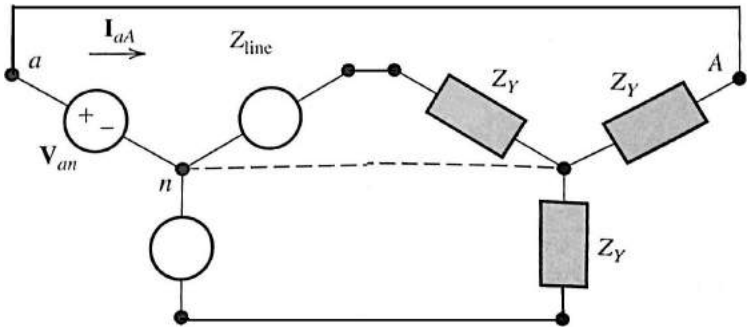

(b) Wye-connected equivalent circuit

Figure A.5: Delta and wye equivalent circuits adapted from [78]

The impedance of the delta load can be calculated as follows:

Element resistance:	R	$= 200\,\text{m}\Omega$	(At room temperature)
Source frequency:	ω	$= 50\,\text{Hz}$	
Inductance:	L	$= 0\,\text{H}$	(Unknown, assume zero)
Impedance:	ZΔ	$= \text{R} + i \cdot \omega \cdot \text{L}$	$= 0.2\,\Omega$

The secondary line-to-line voltage of the delta circuit can be calculated as follows:

Transformer turns ratio:	r	$= 5.5333$	
Primary line-to-line voltage:	$\text{V}_{\text{primary}}$	$= 230\,\text{V}$	
Secondary line-to-line voltage:	V_{ab}	$= \frac{\text{V}_{\text{primary}}}{\text{r}}$	$= 41.5663\,\text{V}$

The wye equivalent circuit is calculated as follows:

Line-to-neutral voltage:	V_{an}	$= \frac{V_{ab}}{\sqrt{3}\angle 30°}$	$20.7831 - 11.9991i\,V$
Wye equivalent load:	Z_y	$= \frac{Z_\Delta}{3}$	$0.0667\,\Omega$
Line impedance:	Z_{line}	$= 0$	(Unknown, assume zero)
Single-phase equivalent current:	I_{aA}	$= \frac{V_{an}}{Z_{line}+Z_y}$	$= 311.747 - 179.9872i\,A$
Line-to-neutral voltage:	V_{an}	$= I_{aA} \cdot Z_y$	$= 20.7831 - 11.9991i\,V$
Line-to-line voltage:	V_{ab}	$= V_{an} \cdot \sqrt{3}\angle 30°$	$= 41.5663\,V$
Line-to-line current:	I_{AB}	$= \frac{V_{ab}}{Z_\Delta}$	$= 207.8313\,A$
Line-to-line RMS current:	I_{ABrms}	$= \frac{I_{AB}}{\sqrt{2}}$	$= 146.9589\,A$
Single-phase power:	P_{AB}	$= I_{AB_{rms}}^2 \cdot R$	$= 4319.386\,W$
Total power:	P_{total}	$= 3 \cdot P_{AB}$	$= 12958.1579\,W$

Repeating the calculations for the elevated temperature (1200 °C) resistance of 2 Ω for each heating element, the following values are obtained:

Single-phase equivalent current:	I_{aA}	$= \frac{V_{an}}{Z_{line}+Z_y}$	$= 31.1747 - 17.9987i\,A$
Line-to-line current:	I_{AB}	$= \frac{V_{ab}}{Z_\Delta}$	$= 20.7831\,A$
Line-to-line RMS current:	I_{ABrms}	$= \frac{I_{AB}}{\sqrt{2}}$	$= 14.69596\,A$
Total power:	P_{total}	$= 3 \cdot P_{AB}$	$= 1295.8158\ W$

The choice of suitable thyristor units were narrowed down by considering current ratings, maximum current and cost. A Tele Haase TST3 16 kW unit with a maximum phase current of 25 A was selected. Confirmation of its suitability and expected operation in the pusher furnace system follow:

Maximum current:	I_{max}	$= 25\ A$	
Secondary maximum current:	I_s	$= r \cdot I_{max}$	$= 138.3333\,A$
Total power @ 24 °C:	P_{24C}	$= 3 \cdot I_s^2 \cdot 0.2\Omega$	$= 11.4817\,kW$

Thus, the limiting factor at room temperature is the supply current.

Total power @ 1200 °C:	P_{1200C}	$= 3 \cdot I_s^2 \cdot 2\Omega$	$= 114.8167\,kW$

This is much greater than 16 kW, therefore the limiting factor at 1200 °C is the power capacity of the thyristor unit.

Secondary maximum current @ 1200 °C:	I_{s16kW}	$= \sqrt{\frac{16kW}{3 \cdot 2\Omega}}$	$= 51.6398\,A$
Primary maximum current @ 1200 °C:	I_{p16kW}	$= \frac{I_{s16\,kW}}{r}$	$= 9.3325\,A$

A.3.3 Thyristor Comparison

Figure A.6 presents a comparison between the required time for the old and new thyristor units to heat the high heat zone to the set temperature of 1130 °C.

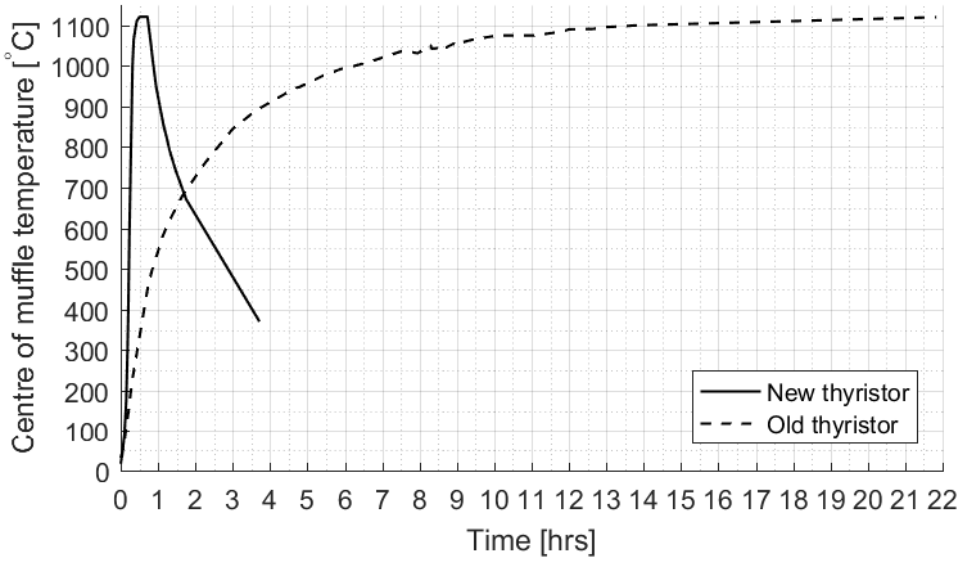

Figure A.6: Thyristor heating comparison

Appendix B

Gas Flow System

B.1 Process Gas System Hardware

B.1.1 Process Gas Flow Diagram

Figure B.1 presents the gas flow diagram for the pusher furnace process gas system used in this project.

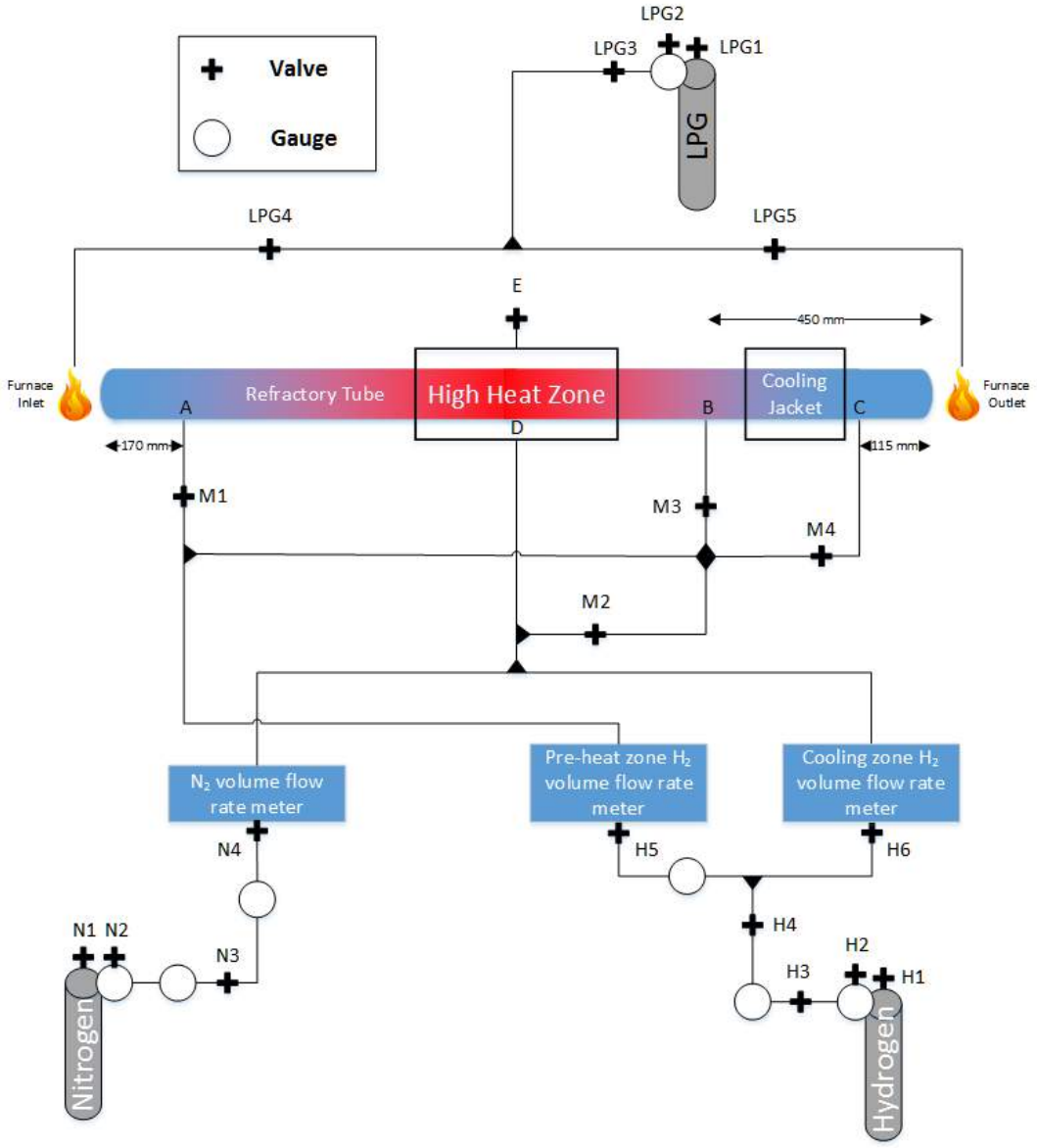

Figure B.1: Process gas flow system schematic

B.1.2 Moisture Bubbler Calculations

This section contains the calculations for a bubble column reactor. Figure 4.1 presents a schematic of the bubbler design. According [40] a typical dewpoint temperature inside the delubing/preheat zone of a furnace is ~8 °C. In order to achieve this dewpoint, the partial pressure of water vapour must be equal to the saturation pressure at a saturation temperature of 8 °C.

Delube dew-point temperature:	T_{dp}	$= 8\,°C$	
Saturation pressure at 8 °C:	$P_{sat,8C}$	$= 1.073\,kPa$	[43]
Partial vapour pressure:	$P_{v,req}$	$= P_{sat,8C}$	$= 1.073\,kPa$
Bubbler temperature:	T_b	$= 20\,°C$	
Water temperature:	T_l	$= T_b$	$= 20\,°C$
Carrier gas volume flow rate:	$\dot{V}_t$	$= 3.33$ l/min	(Appendix B.3.3)
H_2 volume flow rate:	$\dot{V}_{H_2}$	$= 0.6668$ l/min	(Appendix B.3.3)
N_2 volume flow rate:	$\dot{V}_{N_2}$	$= 2.6667$ l/min	(Appendix B.3.3)
Carrier gas pressure (abs):	P_c	$= 151.325\,kPa$	

Properties at 20 °C and 151.325 kPa [50]:

H_2 density:	ρ_{H_2}	$= 0.1225$	$\frac{kg}{m^3}$
N_2 density:	ρ_{H_2}	$= 1.1650$	$\frac{kg}{m^3}$
$H_2O_{(g)}$ density:	ρ_v	$= 0.0173$	$\frac{kg}{m^3}$
$H_2O_{(l)}$ density:	ρ_l	$= 998.16$	$\frac{kg}{m^3}$ [79]
H_2O dynamic viscosity:	μ_{H_2O}	$= 9.9593 \cdot 10^{-4}$	$\frac{kg}{m \cdot s}$

Carrier gas mass flow rate:

H_2 mass flow:	$\dot{m}_{H_2}$	$= 0.0817$	$\frac{g}{min}$
N_2 mass flow:	$\dot{m}_{N_2}$	$= 4.6397$	$\frac{g}{min}$
Carrier gas mass flow:	$\dot{m}_c$	$= \dot{m}_{H_2} + \dot{m}_{N_2}$	$= 4.7214 \quad \frac{g}{min}$

Gas constants [43]:

H_2 gas constant:	R_{H_2}	$= 4.1240 \frac{kJ}{kgK}$	
N_2 gas constant:	R_{N_2}	$= 0.2968 \frac{kJ}{kgK}$	
$H_2O_{(g)}$ gas constant	R_v	$= 0.4615 \quad \frac{kJ}{kgK}$	
Carrier gas constant	R_c	$= \frac{R_{H_2} \cdot \dot{m}_{H_2} + R_{N_2} \cdot \dot{m}_{N_2}}{\dot{m}_{H_2} + \dot{m}_{N_2}}$	$= 0.3302 \quad \frac{kJ}{kgK}$

Required absolute humidity [43]:

$$\omega_{req} = \frac{R_v}{R_c} \frac{P_{v,req}}{P_c} = 0.009 \tag{B.1}$$

Required vapour mass flow rate [43]:

$$\dot{m}_{v,req} = \omega_{req} \dot{m}_c = 42.5631 \quad \frac{mg}{min} \tag{B.2}$$

Required vapour volume flow rate via Dalton's law [43]:

$$\dot{\mathrm{V}}_{v,req} = \dot{\mathrm{V}}_{\mathrm{t}} \frac{\mathrm{P}_{v,req}}{\mathrm{P}_{\mathrm{c}}} = 0.0236 \quad \frac{l}{min} \tag{B.3}$$

In order to calculate the diffusion of H_2O to the carrier gas, the rise time for a bubble must be determined. Using the velocity of a bubble and the water column height, the rise time can be estimated. The terminal velocity is assumed to be reached immediately as the bubble is released, from the airstone, into the continuous liquid. A homogeneous bubble distribution is assumed, where all bubbles are the same size and have no influence on each other. Visual observations indicate that, for the airstone used, 5 mm diameter (perfectly spherical) bubbles can be assumed.

Gravitational acceleration:	g	$= 9.81$	$\frac{m}{s^2}$
Bubble diameter:	d_b	$= 5$	mm
Water column height:	H_{H_2O}	$= 200$	mm

Bubble terminal velocity [80, 81]:

$$u_b = \frac{2}{3} \cdot \sqrt{g \cdot \frac{d_b}{2}} = 104.40 \quad mm/s \tag{B.4}$$

Bubble travel time through water column:

$$t_{H_2O} \geq \frac{H_{H_2O}}{u_b} = 1.9157 \quad sec \tag{B.5}$$

Atomic volumes [82]:

$V_{a,H_2} = 14.3$
$V_{a,N_2} = 15.6$
$V_{a,H_2O} = 18.8$
$V_{a,c} = x_{\mathrm{H_2,ph}} \cdot V_{a,H_2} + x_{\mathrm{N_2,ph}} \cdot V_{a,N_2} = 15.34$

Molar masses [83]:

$M_{\mathrm{H_2}} = 2.0160 \quad \frac{\mathrm{kg}}{kmol}$
$M_{\mathrm{N_2}} = 28.010 \quad \frac{\mathrm{kg}}{kmol}$
$M_{H_2O} = 18.015 \quad \frac{\mathrm{kg}}{kmol}$

Moles [50]:

$\dot{\mathrm{N}}_{\mathrm{H_2}} = \frac{\dot{\mathrm{m}}_{\mathrm{H_2}}}{M_{\mathrm{H_2}}} = 0.0007 \quad \frac{mol}{sec}$
$\dot{\mathrm{N}}_{\mathrm{N_2}} = \frac{\dot{\mathrm{m}}_{\mathrm{N_2}}}{M_{\mathrm{N_2}}} = 0.0028 \quad \frac{mol}{sec}$
$\dot{\mathrm{N}}_c = \dot{\mathrm{N}}_{\mathrm{H_2}} + \dot{\mathrm{N}}_{\mathrm{N_2}} = 0.0034 \quad \frac{mol}{sec}$

Mole fractions [50]:

$$X_{\mathrm{H_2}} = \frac{\dot{\mathrm{N}}_{\mathrm{H_2}}}{\dot{\mathrm{N}}_{\mathrm{t}}} = 0.1965$$
$$X_{\mathrm{N_2}} = \frac{\dot{\mathrm{N}}_{\mathrm{N_2}}}{\dot{\mathrm{N}}_{\mathrm{t}}} = 0.8035$$

Carrier gas molar mass [82]:

$$M_{\mathrm{c}} = X_{\mathrm{H_2}} \cdot M_{\mathrm{H_2}} + X_{\mathrm{N_2}} \cdot M_{\mathrm{N_2}} = 22.9026 \quad \frac{\mathrm{kg}}{kmol} \tag{B.6}$$

Diffusion coefficient [84]:

$$D_{eq} = \frac{0.0043 \cdot T_b^{\frac{3}{2}}}{\mathrm{P_c} \cdot (V_{a,c}^{\frac{1}{3}} + V_{a,H2O}^{\frac{1}{3}})^2} \cdot \sqrt{\frac{1}{M_{\mathrm{c}}} + \frac{1}{M_{H_2O}}} = 17.2 \quad mm^2 \tag{B.7}$$

Diffusion penetration depth [83]: The penetration depth allows the depth of diffusion to be determined at any given time. The penetration depth is a straight line with a gradient equal to the concentration gradient at the bubble-liquid interface. It starts at the bubble-liquid boundary and ends where it intercepts the initial concentration of moisture in the bubble. This distance, along the initial concentration line, is the penetration depth. A schematic representation of the penetration depth can be seen in Figure B.2a where 'C' is the concentration of water vapour in the carrier gas bubble. For the current scenario, penetration depth is calculated in Equation B.8. Note that the penetration depth, in this case, is larger than the bubble radius.

$$\delta_{diff} = \sqrt{\pi \cdot D \cdot t_{H2O}} = 10.17 \quad mm \tag{B.8}$$

Average mass transfer coefficient was assumed constant throughout the bubble, resulting in:

$$k_l = \frac{D}{\delta_{diff}} = 1.69 \quad \frac{mm}{s} \tag{B.9}$$

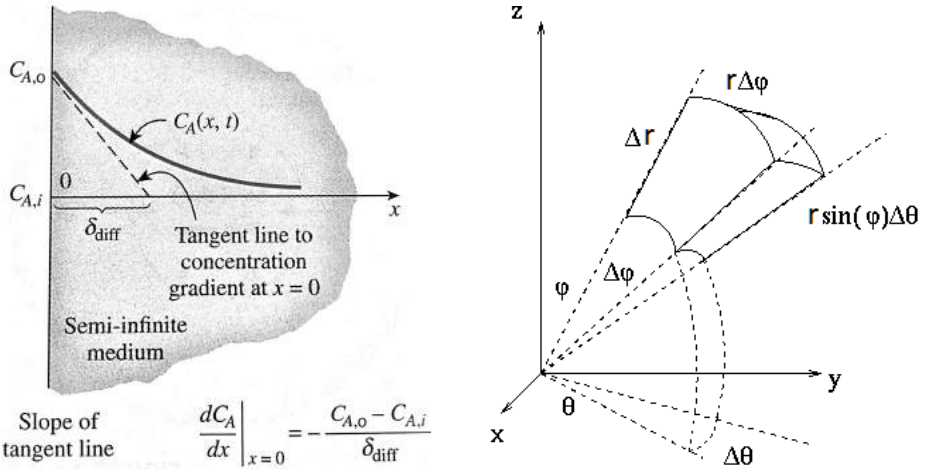

(a) Bubble water vapour penetration depth [83]

(b) Sphere Polar Coordinate Volume Element

Figure B.2: Bubble calculation concept schematics

In order to calculate the total vapour mass present in a bubble, a derivation of this quantity is required. Firstly, the volume of a sphere can be calculated through a polar coordinate derivation presented in Equation B.10 with the volume element defined in Figure B.2b.

$$dV = r^2 \cdot dr \cdot sin\phi \cdot d\phi \cdot d\theta \tag{B.10}$$

The volume of a spherical shell with outer radius of r_o and inner radius of r_i is therefore:

$$\begin{aligned} V &= \int_0^{2\cdot\pi} \int_0^{\pi} \int_{r_i}^{r_o} r^2 \cdot dr \cdot sin\phi \cdot d\phi \cdot d\theta \\ &= \frac{4 \cdot \pi}{3} \cdot (r_o^3 - r_i^3) \quad (for\ a\ spherical\ shell) \\ &= \frac{4 \cdot \pi}{3} \cdot r_o^3 \quad (for\ a\ solid\ sphere) \end{aligned} \tag{B.11}$$

The vapour content profile over the penetration depth is:

$$
\begin{aligned}
&C_v = w \cdot (r - r_i) \quad (for\ partial\ vapour\ penetration)\\
&C_v = w \cdot r + c \qquad (for\ full\ vapour\ penetration)\\
&\quad where\ 'w'\ is\ the\ concentration\ gradient\\
&\quad and\ 'c'\ is\ the\ intercept\ at\ the\ center\ point\ of\ the\ sphere\\
&c = C_o - w \cdot r_o\\
&w = \frac{C_o}{\delta_{diff}}
\end{aligned}
\tag{B.12}
$$

Combining Equations B.10 and B.12 an equation for the differential vapour mass content is obtained, Equation B.13:

$$dm_v = r^2 \cdot dr \cdot sin\phi \cdot d\phi \cdot d\theta \cdot C_v \tag{B.13}$$

Integration of Equation B.13 results in:

$$
\begin{aligned}
m_{v,b} &= \int_0^{2\cdot\pi} \int_0^{\pi} \int_{r_i}^{r_o} r^2 \cdot dr \cdot sin\phi \cdot d\phi \cdot d\theta \cdot C_v\\
&= 4\pi \cdot \left(\frac{C_o}{r_o - r_i}\right) \cdot \left(\frac{r_o^4}{4} + \frac{r_i^4}{12} - \frac{r_i \cdot r_o^3}{3}\right) \qquad (for\ a\ spherical\ shell)\\
&= 4\pi \cdot r_o^3 \cdot \left(\frac{C_o}{4 \cdot \delta_{diff}} + \frac{C_o}{3} \cdot \left(1 - \frac{r_o}{\delta_{diff}}\right)\right) \quad (for\ a\ full\ sphere)\\
&= 0.0011 \quad mg
\end{aligned}
\tag{B.14}
$$

Bubble volume from Equation B.10:

$$V_b = \tfrac{4}{3} \cdot \pi \cdot \left(\tfrac{d_b}{2}\right)^3 = 65.45 \quad \text{mm}^3$$

Number of bubbles for a carrier gas volume flow of 3.3334 l/min:

$$n_b = \frac{V_t}{V_b} = 848.9 \quad 1/sec$$

Vapour mass transfer to carrier gas:

$$m_{v,total} = n_b \cdot m_{v,b} = 54.13 \quad \frac{mg}{min}$$

Looking back at the required vapour mass transfer of 42.56 $\frac{\text{mg}}{\text{min}}$ it is clear that if all the process gas going to the preheat zone is passed through the bubbler, too much vapour will enter the furnace tube. Too much vapour will adversely affect the samples and/or furnace. Reducing the carrier gas volume flow rate to 2.6212 l/min:

$$n_b = \frac{V_t}{V_b} = 667.5 \quad 1/\text{sec}$$
$$m_{v,total} = n_b \cdot m_{v,b} = 42.56 \quad \frac{\text{mg}}{\text{min}}$$

This quantity alone is needed to ensure the correct dewpoint is maintained. Additional moisture must be added to the process gas during delubrication to ensure the correct stoichiometric quantity of H_2O is available for the pyrolysis reactions to take place.

B.1.3 LPG Clear Piping Safety

Introduction

Mr C Zietsman expressed his concern over the safety of the clear PVC piping used to feed the LPG burner flames at the entrance and exit to the furnace tube. Mr Zietsman's concerns were noted and investigated. The findings for this investigation is presented in this section.

Chemical Suitability

PVC is an abbreviation for Polyvinyl chloride with the chemical formula of $(C_2H_3Cl)_n$ [85].

PVC has the following properties, it [86]: 1) is strong and rigid, 2) is resistant to a variety of acids and bases, 3) may be damaged by some solvents and chlorinated hydrocarbons, 4) has a maximum service temperature of 60 °C, 5) is safe for use in water, gas and drainage systems, and 6) is not suitable for hot water systems.

87 mentions that PVC piping is generally resistant to most acids, bases, salts, aliphatic solutions, oxidants and halogens. According to [85] PVC is particularly well suited for aliphatic hydrocarbons.Aliphatic hydrocarbons are hydrocarbon compounds which contain carbon and hydrogen joined together in straight chains [88]. Liquid Petroleum Gas (LPG) contains a mixture of hydrocarbons, mostly consisting of propane (C_3H_8) and butane (C_4H_{10}) [89]. Marley pipe systems provide a full range of technical documentation on their current range of piping. In this comprehensive document, PVC piping is recommended for use with propane gas [90]. Therefore, the chemical suitability of PVC piping is very good for its current application.

Pressure Rating

At 22.78 °C Schedule 40 1/4" PVC piping has a pressure rating of 2688.96 kPa [87]. The LPG regulator creates a pressure drop from the LPG cylinder to the Bunsen burners. The pressure after the regulator is constant at 2.8 kPa, this is much lower than the rated pressure of the clear PVC piping. Even at 60 ,°C, where the rated pressure of the piping drops to 0.22 of its room temperature rating [87], the rated pressure is 591.57 kPa which is still 211 times the required pressure. Therefore, there is a very large safety factor for the pressure condition of the current piping application.

Flammability

PVC piping exhibits excellent physical properties and flammability characteristics [87]. PVC piping has a flash ignition temperature of 387.778 °C and a flammability rating of V-0 according to the UL-94 standard test method [91]. As can be seen from Table B.1 [92], a rating of V-0 indicates that PVC is a flame retardant material.

Table B.1: UL-94 flammability rating [92]

Observation	**V-0**	**V-1**	**V-2**	**Units**
Burning time after flame application	≤10	≤30	≤30	sec
Total burning time (10 flame applications)	≤50	≤250	≤250	sec
Burning and afterglow times of specimens after second flame application	≤30	≤60	≤60	sec
Dripping of burning specimens (ignition of cotton batting)	no	no	yes	N/A
Specimens completely burned	no	no	no	N/A

Conclusions

The suitability of PVC piping for the LPG supply to the burner flames of the pusher furnace was considered. Chemical, pressure and flammability issues were investigated and it was found that there is no cause for concern using the piping in its current application.

B.2 Process Gas System Calibration

B.3 Nitrogen Cylinder Pressure Drop

Figure B.3 presents the measured N_2 cylinder pressure drop and, old calibration data, expected cylinder pressure drop when using 20 scale markings of flow at

50 kPa.

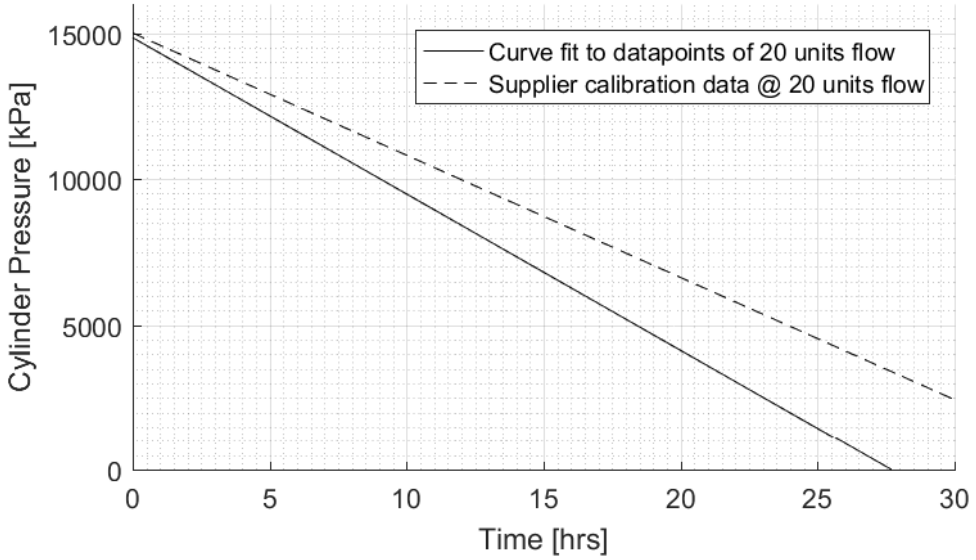

Figure B.3: Process gas, N_2, cylinder pressure drop during use at 20 units of VAF scale markings

B.3.1 Instrumentation Error: Root Sum Squares Method

The propagated error is calculated using Equation B.15, where 'u_{sys}' is the total system error and 'n' is the number of errors in the system. A plot of the data with the instrumentation error, calculated through the use of this method, is given in Figure B.4.

$$u_{sys} = \sqrt{\sum_{i=1}^{n} u_i^2} \tag{B.15}$$

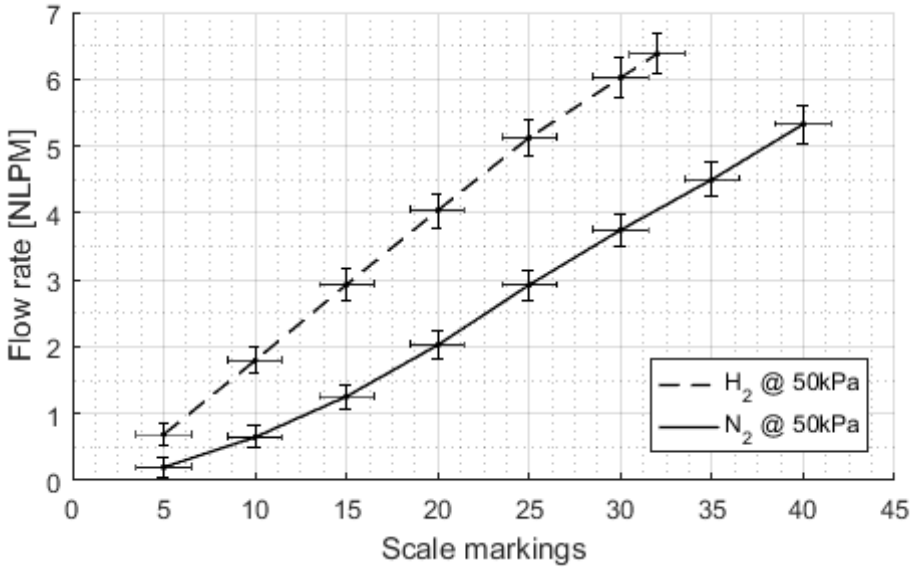

Figure B.4: Process gas flow meter calibration curves with instrumentation error

B.3.2 Non-Linear Regression: Least Squares Method

The least squares curve fit method can be described by the Equations B.16 – B.22. For N amount of data points, each of which are referred to as x_i and y_i, with $i = 1, 2, ..., N$. The flow rate (y) is related to the scale markings (x), at a given pressure, through Equation B.16:

$$y_{ci} = \beta_0 x_i^3 + \beta_1 x_i^2 + \beta_2 x_i + \beta_3 \tag{B.16}$$

where β are the coefficients to be determined in order to fit the curve to the data. The deviation then between the resulting polynomial (y_{ci}) and the dependant variable (y_i) is defined as $y_i - y_{ci}$. The sum of squares is represented as follows, Equation B.17:

$$D = \sum_{i=1}^{N} (y_i - y_{ci})^2 \tag{B.17}$$

Combining Equations B.16 and B.17, Equation B.18 results:

$$D = \sum_{i=1}^{N} (y_i - (\beta_0 x_i^3 + \beta_1 x_i^2 + \beta_2 x_i + \beta_3))^2 \tag{B.18}$$

In order to minimize D, Equation B.18 is differentiated with respect to the coefficients β, resulting in 4 partial derivatives which are set equal to zero in Equation B.19. The simultaneous solution of Equation B.19 yields the unknown regression constants β_0, β_1, β_2, β_3.

$$\frac{\partial D}{\partial \beta} = 0 = \frac{\partial}{\partial \beta}(\sum_{i=1}^{N}(y_i - (\beta_0 x_i^3 + \beta_1 x_i^2 + \beta_2 x_i + \beta_3))^2) \tag{B.19}$$

In order to calculate the confidence interval, the standard deviation of the curve fit must be calculated using Equation B.20, where the degrees of freedom (v) are $v = N - (m + 1)$, with $m = 3$ (for a third order polynomial):

$$\mathrm{S}_{yx} = \sqrt{\frac{D}{v}} \tag{B.20}$$

Assuming variation in both x and y data a confidence band can be found using Equation B.21:

$$\mathrm{y_c(x)} \pm \mathrm{t_{v,P} S_{yx}} \sqrt{\frac{1}{\mathrm{N}} + \frac{(\mathrm{x} - \bar{\mathrm{x}})^2}{\sum_{\mathrm{i=1}}^{\mathrm{N}} (\mathrm{x}_i - \bar{\mathrm{x}})^2}} \tag{B.21}$$

where 't' is called the t-estimator whose value is a function of the probability (P) and degrees of freedom (v). Its value for a range of 'P' and 'v' is given in [73].

In order to tell how strong the relationship between flow rate and scale markings are for the polynomial fit, a correlation coefficient (r) can be found. For a linear polynomial [73] presents Equation B.22. The correlation coefficient provides a measure of association between 'x' and 'y' as predicted by the curve fit equation. Values for 'r' range between ± 1, with the sign indicating whether flow rate (y) increases or decreases with an increase in the scale markings (x). The closer 'r' is to ± 1 the better an association is observed between 'x' and 'y', where a value of zero indicates that 'x' and 'y' are not related [93]. r^2 values are an indication of how well the variance in 'y' is accounted for by the curve fit [73].

$$\mathrm{r} = \sqrt{1 - \frac{\mathrm{D}}{\sum_{\mathrm{i=1}}^{\mathrm{N}} (\mathrm{y_i} - \bar{\mathrm{y}})}} \tag{B.22}$$

Matlab has a built-in function called 'fitnlm', which performs a non-linear

curve fit according to the least squares method. This method of curve fitting requires an initial guess as to the values of β. The function was used with the calibration data collected [1] for each flow meter and the resulting curves are plotted in Figure 4.8.

B.3.3 Process Gas Volume Flow Rate Calculations

This section contains the calculations for the process gas distribution within the gas system piping. See Figure B.1 for valve locations.

Valves E, M4, and H6 are closed fully.
The line pressure after the N_2 and H_2 rotameters is 50 kPa.
The gas temperature is 20 °C.
There are no leaks in the gas system.

Total process gas flow rate:	$\dot{V}_t$	$= 6\,l/min$	
Nitrogen volume fraction:	v_{N_2}	$= 0.88886$	
Hydrogen volume fraction:	v_{H_2}	$= 1 - v_{N_2}$	$= 0.11114$
N_2 inlet volume flow rate:	$\dot{V}_{N_2,i}$	$= v_{N_2} \cdot \dot{V}_t$	$= 5.3332\,l/min$
H_2 inlet volume flow rate:	$\dot{V}_{H_2,i}$	$= v_{H_2} \cdot \dot{V}_t$	$= 0.6668\,l/min$

Looking first at the flow path of N_2, the first T-junction directs gas towards the preheat zone and the cooling zone. It is assumed that the N_2 separates equally between the two paths, as the pipe losses are negligible over the short lengths and both paths exhaust to atmospheric pressure inside the furnace tube.

N_2 flow to preheat zone:	$\dot{V}_{N_2,ph}$	$= \frac{\dot{V}_{N_2,i}}{2}$	$= 2.6667\,l/min$
N_2 flow to cooling zone:	$\dot{V}_{N_2,cool}$	$= \dot{V}_{N_2,ph}$	$= 2.6667\,l/min$
H_2 flow to preheat zone:	$\dot{V}_{H_2,ph}$	$= \dot{V}_{H_2,i}$	$= 0.6668\,l/min$
Total volume flow to preheat zone:	$\dot{V}_{ph}$	$= \dot{V}_{H_2,ph} + \dot{V}_{N_2,ph}$	$= 3.3334\,l/min$
Preheat N_2 volume fraction:	$v_{N_2,ph}$	$= \frac{\dot{V}_{N_2,ph}}{\dot{V}_{ph}}$	$= 0.8$
Preheat H_2 volume fraction:	$v_{H_2,ph}$	$= 1 - v_{N_2,ph}$	$= 0.2$

This means that in order for flow at the preheat zone to be mixed in a ~80/20 volume ratio, a ~89/11 volume ratio is required at the inlets.

B.3.4 Furnace Atmosphere Turnover Rate

Herewith follows calculations to determine the minimum and maximum (according to safety concerns) pusher furnace atmosphere turnover rate.

[1] Data was collected using an Alicat M-5SLPM-D/M capillary type mass flow meter

Minimum atmosphere turnover rate [37]:	x	$= 10\,1/\mathrm{hr}$	
Minimum atmosphere flow rate:	$\dot{V}_{max}$	$= 6\,\mathrm{l/min}$	
Furnace tube inside diameter:	d	$= 75\,\mathrm{mm}$	
Furnace tube length:	L	$= 1.8\,\mathrm{m}$	
Furnace tube cross-sectional area:	A	$= \pi \cdot (\frac{d}{2})^2$	$= 4417.8647\,\mathrm{mm}^2$
Furnace tube volume:	V_{tube}	$= A \cdot L$	$= 7.9522\,\mathrm{l}$
Volume flow rate required per hour::	Q_{req}	$= V \cdot x$	$= 79.5216\,\mathrm{l/hr}$
Volume flow rate required per min:	Q_{min}	$= 1.3254\,\mathrm{l/min}$	
Turnover rate with 6 l/min:	Q_{max}	$= \frac{\dot{V}_{max} \cdot 60\,\mathrm{min}}{V_{tube} \cdot 1\mathrm{hr}}$	$= 45.2707\,1/\mathrm{hr}$

Appendix C

Material Properties

C.1 Constant Properties

Table C.1 [30–34] gives the relevant material properties of the materials considered in this study. The table shows that the infiltrate in the Fe-Cu-C system has a much higher thermal conductivity than the metal-matrix material, as is desired. The infiltrate melting point is considerably lower than that of the solid matrix material.

Table C.1: Relevant Material Properties [30–34]

Material	**Copper (Cu)**	**Iron (Fe)**
Thermal conductivity [W/m K] @ 20 °C	386	73
Melting Point [°C]	1084	1535
Yield Strength [MPa]	117	80-100
Ultimate Strength [MPa]	210	350
Hardness [MPa, HV]	369	608
Solid Density [kg/m^3]	8790	7870

Table C.2: Atomic masses [50]

Element	**Atomic mass**
C	12.01
Zn	65.41
H	1.008
O	16.00
N	14.01

C.2 Temperature Dependent Material Properties

The surface tension (or surface energy) of a fluid was mentioned in Section 2.4.3 where its relevance is explained in connection with the contact angle of a fluid. The surface tension of Cu is presented here as it varies with temperature. Another property that varies considerably with temperature is that of viscosity, which is also presented in this section. A simple equation for the calculation of surface tension of molten Cu is given by Equation C.1 [94]:

$$\sigma_{\mathrm{Cu}}(\mathrm{T}) = 1257 + \sigma'(\mathrm{T} - 1356) \tag{C.1}$$

Where 'σ' was experimentally determined to be -0.2 $\mathrm{mJ.m^{-2}.K^{-1}}$ and 'T', temperature, in Kelvin [94]. Equation C.1 was plotted in the temperature range of interest for this project and can be seen in Figure C.1a.

It is important to differentiate between kinematic and dynamic viscosity. Dynamic viscosity of a fluid is its internal resistance to flow, where the kinematic viscosity of the fluid is the ratio of dynamic viscosity to the fluid density. The dynamic viscosity, 'μ', of Cu is therefore of interest in this study and can be seen in Figure C.1b. From Figure C.1b [95], which shows experimental values of dynamic viscosity, it can be seen that as temperature increases the dynamic viscosity of molten Cu decreases.

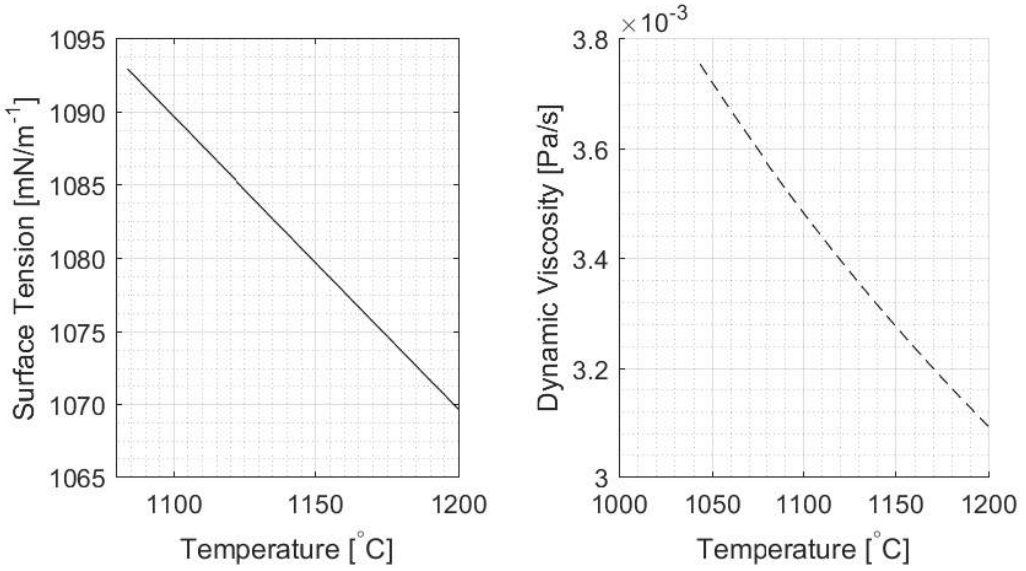

(a) Surface tension of Cu with temperature (adapted from [94])

(b) Dynamic viscosity of Cu with temperature (adapted from [95])

Figure C.1: Liquid Cu properties

C.3 Phase Diagrams

C.3.1 Cu-C Phase Diagram

A maximum amount of up to ~0.0078 wt% carbon is soluble in Cu at 1100 °C. However, this already small amount decreases drastically above 1100 °C, where the solubility limit becomes ~0.00025 wt%. Comparing the solubility of Cu or C in Fe with the solubility of Cu in C it can be concluded that mutual solubility between Cu and C can be disregarded as it is three orders of magnitude smaller.

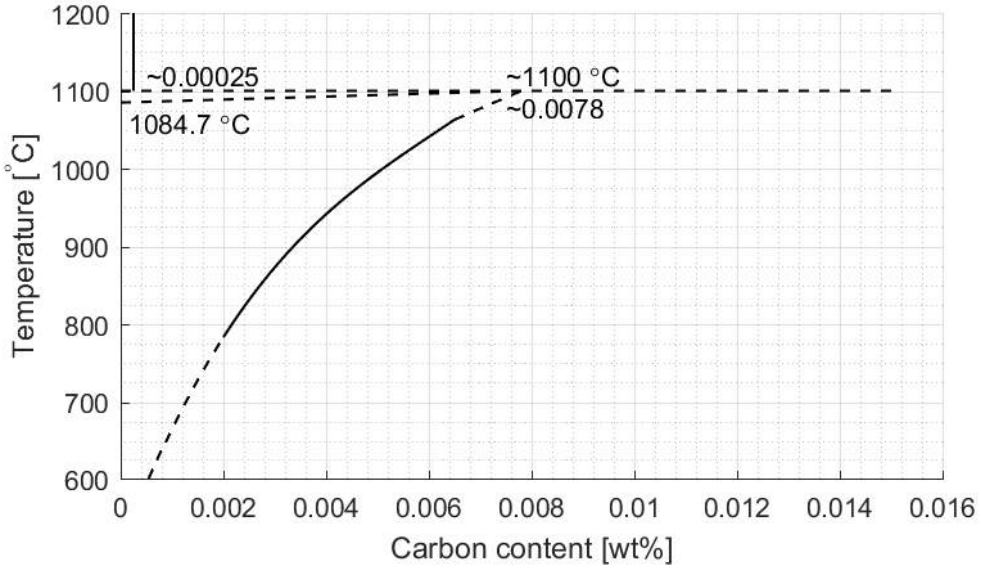

Figure C.2: Cu-C phase diagram adapted from [64]

C.3.2 Cu-Mn Phase Diagram

Figure C.3, adapted from [64], presents the Cu-Mn phase diagram.

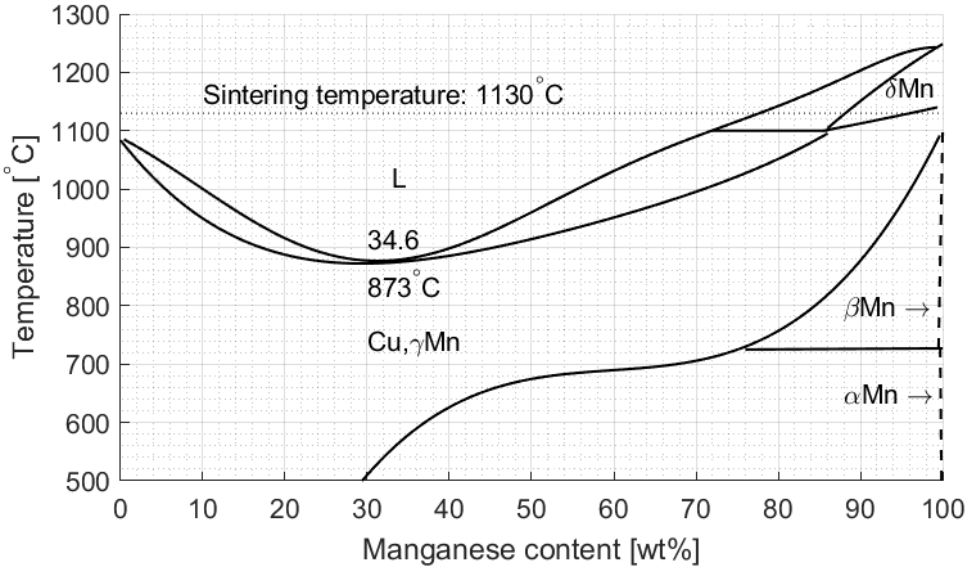

Figure C.3: Cu-Mn phase diagram adapted from [64]

C.4 Infiltrated Part Calculations

In order to calculate the total porosity (at any stage of sintering), Equation C.2 may be used, as indicated by [7]. Where ρ is the current part density and ρ_w is the wrought material density.

$$P_t = 100(1 - \frac{\rho}{\rho_w}) \ [\%] \tag{C.2}$$

The following calculations may be performed after infiltration, Equation C.3 – C.6, as indicated by [7]:

Theoretical Density (TD):

$$TD = \frac{100}{\sum_{i=1}^{n} \frac{w_i}{\rho_i}} \ [\%] \tag{C.3}$$

Where 'w_i' is the weight percent (wt%) of the constituent element 'i', 'ρ_i' is the density of the constituent element and 'n' is the total number of constituent elements.

Mass fraction (w_i) of constituent:

$$w_i = \frac{m_i}{\sum_{j=1}^{n} m_j} \tag{C.4}$$

Where m_i is the mass of the constituent of interest.

Volume percent of constituent:

$$V_i = \frac{100\frac{w_i}{G_i}}{\sum_{j=1}^{n} \frac{w_j}{G_j}} \ [\%] \tag{C.5}$$

Where 'G' is the specific gravity of the constituent.

Volume percent of porosity:

$$V_{p\,\text{after infiltration}} = V_{p\,before\ infiltration} - V_{\text{infiltrate}\,\text{after infiltration}} \ [\%] \tag{C.6}$$

It is often necessary to convert between volume and mass (or weight) fractions because the porosity of the preform is given as a volume fraction and the phase diagrams are given in wt%. The following equations, C.7 and C.8, may be used to converter between volume fraction (v) and mass fraction (w) respectively [96].

$$v_1 = \frac{1}{(1 + \frac{\rho_1}{\rho_2}(\frac{1}{w_1} - 1))} \tag{C.7}$$

$$w_1 = \frac{\rho_1 v_1}{(\rho_2 + (\rho_1 - \rho_2)v_1)} \tag{C.8}$$

Appendix D

Thermoanalytic Behaviour

D.1 DSC Background

DSC data is notoriously difficult to interpret, but some general remarks can be made of certain trends in the data:

- Positive values of heat flow indicate that heating of the sample required more energy than the reference to change its temperature.
- Negative values of heat flow indicate that the sample required less energy than the reference in order to change its temperature.
- The area under a (heat flow vs. time) curve is equal to the energy requirement of the change in temperature.
- Peaks in DSC data can indicate the occurrence of phase transformations or chemical reactions.
- The height of a peak gives an indication of the rate of change of the reaction or transformation.
- The sign of the slope of a DSC curve can be indicative of an exothermic or endothermic reaction[1]. In order to tell with certainty if the reaction is exo- or endothermic, one must take into account the entropy[2] of the reacting system.

D.2 Thermal Behaviour of Zinc Stearate

In this investigation, the optimal hold temperature for zinc stearate delubrication is of interest. Additionally, the time required for complete

[1] An exothermic reaction is a reaction wherein energy is released during the reaction. An endothermic reaction is a reaction wherein energy is absorbed during the reaction.

[2] Entropy is the degree of disorder in a system.

delubrication of zinc stearate at this optimal temperature is of interest. Tests were conducted using a Perkin Elmer DSC 8000 thermoanalytic device. The DSC 8000 has an accuracy of ±0.05 °C and a precision of ±0.008 °C.

D.2.1 Experiment Procedure

Research Question: What is the optimal hold temperature for zinc stearate delubrication and how long a hold time is required for optimal delubrication?

Hypothesis: A temperature larger than 600 °C is required for optimal delubrication of zinc stearate. Longer hold times will result in more complete delubrication. Below a certain temperature, ~500 °C, delubrication will be insufficient regardless of the length of hold time at this temperature.

Analysis of 12 zinc stearate specimens, each with a mass of ~5 mg, was conducted in air and similarly in N_2 with a flow rate of 40 ml/min. Before each specimen run a reference run, identical to the specimen run following it, was conducted using an empty alumina pan. The result of the empty pan run allows the difference between the specimen and reference pans to be observed, which effectively cancel each other out. The reference run data is subtracted from the sample run data in order to observe the true behaviour of the specimen only. Mass measurements were performed using a KERN ABT 120-5DM precision scale with a reproducibility of 0.02 mg, linearity of ±0.05 mg. The empty alumina pan was weighed whereafter a specimen was then positioned in the empty alumina pan and weighed. The calculated difference in mass between the empty pan and specimen filled pan gives the specimen mass. The specimen was then positioned inside the DSC furnace with a compressed air or N_2 [3] flow rate of 40 ml/min. Each specimen was individually heated to one of four hold temperatures; 400, 500, 600 and 700 °C. The hold time at each of these temperatures was 10 min. Equal rise times were used to reach the hold temperatures, i.e. different heating rates were used for each specimen in order to keep the heating time constant for all specimens. The constant heating time ensures that all the specimens have equal time for delubrication to take place, allowing for the effect of temperature and time on delubrication to be observed. The maximum heating rate achievable in the Perkin Elmer DSC8000 is 300 °C/min, thus heating to the various hold temperatures from a starting temperature of 50 °C was executed at;

- 300.00 °C/min for heating to 700 °C (2.17 min)
- 253.85 °C/min for heating to 600 °C (2.17 min)
- 207.69 °C/min for heating to 500 °C (2.17 min)
- 161.54 °C/min for heating to 400 °C (2.17 min)

[3] Compressed air and pure nitrogen was used because the use of a N_2:H_2 atmosphere in the DSC was not viable at the time of this investigation.

Each specimen was subsequently weighed after processing in order to determine the mass of lubricant remaining after the DSC delubrication.

D.2.2 Results

The heat flow data for the duration of the isothermal hold is presented in Figure D.1.

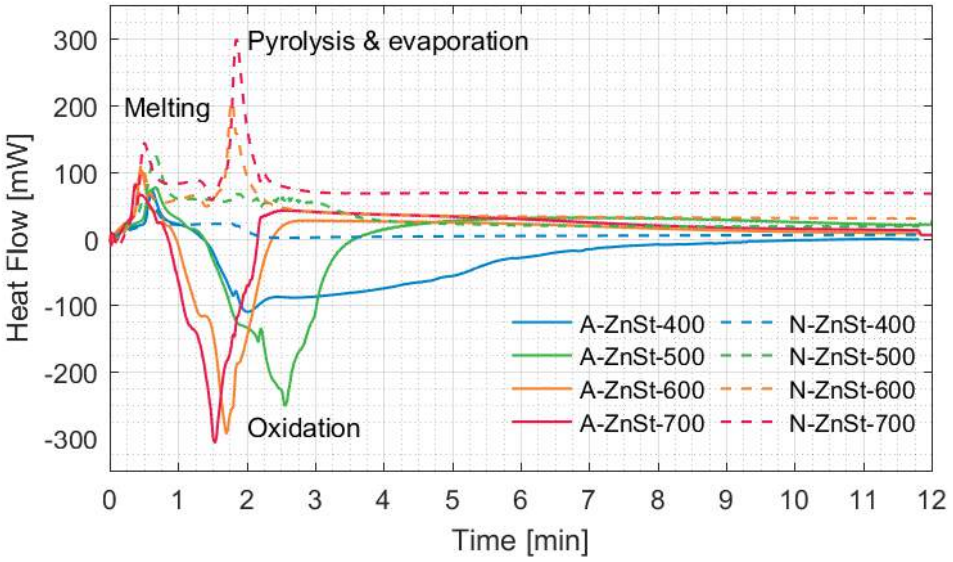

Figure D.1: Thermoanalytic heat flow curves for an isothermal hold of zinc stearate specimens in both air and N_2 atmospheres

Figure D.2 is a horizontal bar graph showing the degree to which delubrication occurred, by presenting the retained weight percentage (wt%) of the initial sample mass, following an isothermal hold. The isothermal hold at 400 °C had caused partial delubrication of the Zinc stearate, resulting in the formation of a large volume of black residue, carbon sooting[4]. The isothermal hold at 500 °C resulted in a dark soot formation on the surfaces of the alumina pan. The isothermal hold at 600 °C had resulted in the formation of some light (white/grey) coloured, powdery residue in the alumina pan. The isothermal hold at 700 °C had resulted in a visibly clear alumina pan, possibly (as indicated by the mass measurements) leaving some residue which cannot be distinguished from the matt white surface of the alumina pan.

[4]Zinc stearate is a pure white, soapy, powder.

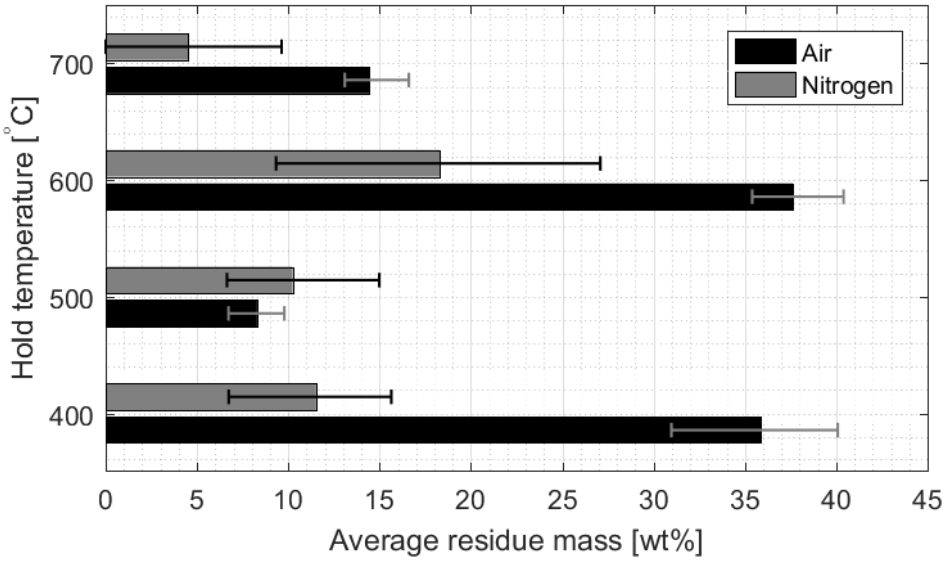

Figure D.2: Zinc Stearate Residue wt%

D.2.3 Discussion

It can be seen that all of the samples reach a thermal steady state during the 10 min isothermal hold. For 400 °C processed in air the time required to reach steady state is ~9.2 min. For 500 °C this time is reduced to ~4.8 min, and for 600 and 700 °C this time is further reduced to ~2.8 min and ~2.4 min respectively. Thus, as the hold temperature is increased the time required to reach a steady state decreases, indicating that delubrication occurs at a faster rate at higher temperatures, with diminishing returns. Once a steady state is reached any subsequent delubrication that might occur is negligible because of the very low thermal activity observed.

The mass data was found to be inconclusive, due to there being no clear trend in the data. A possible reason for the fluctuations in mass results is that the lubricant boils at a temperature between 400 – 500 °C. This boiling caused the lubricant to boil out of the alumina pan and adhere to the pan covers and walls of the DSC furnace, evident by the sooting left on these surfaces, leading to bad mass data for the specimens at these temperatures. From this data and the visual observations, a minimum delubrication temperature of 600 °C is required in the preheat zone, but an increased temperature is beneficial.